AGENTS OF PLANETARY GEOMORPHIC CHANGE: MARTIAN AEOLIAN MORPHODYNAMICS AND THE EMPLACEMENT OF CRATER EJECTA

by
Kirby Daniel Runyon

A dissertation submitted to Johns Hopkins University in conformity with the requirements for the degree of Doctor of Philosophy

Baltimore, Maryland
August, 2017

ABSTRACT

High resolution images of planetary surfaces, such as of Mars from the High Resolution Imaging Science Experiment (HiRISE) camera, reveal a landscape shaped by wind and impact cratering. Wind is the most formative geologic agent on Mars today and impact cratering is the most pervasive geologic process over the lifetime of the Solar System's solid worlds.

In this thesis, I examine the geomorphology and morphodynamics of aeolian geology on Mars and the emplacement of impact crater ejecta on solid worlds with an eye toward the Moon. I provide an introduction to these topics and planets in Chapter 1. In Chapter 2, I present a model for predicting sand flux changes downwind within a dune field by invoking internal boundary layer flow and topographic wind speed changes. These predictions are consistent with measured sand fluxes and changes in dune geomorphology as a function of downwind distance. Chapter 3 builds off this work to explain the existence of Martian sand sheets as deriving from erosion via sand suspension of upwind dunes, in contrast to Earth's dunes and sheets. These results and insights were facilitated by atmospheric circulation models combined with automatic and manual ripple and dune change detection methods. Chapter 4 unveils a new method for studying the dynamics and resulting geomorphology of the emplacement of impact crater ejecta. Along with presenting this new method, I also present geologic results from the initial experiments which reveal ejecta emplacement to be both erosive and depositional, analogous to terrestrial debris flows. The consequences of heterogeneous ejecta emplacement provide an interpretive framework for analyzing spectral datasets, samples, and stratigraphic relations for the Moon and other solid worlds.

Faculty Readers

- **Professor Bruce D. Marsh, PhD**

  Professor & Advisor

  The Johns Hopkins University

  Morton K. Blaustein Department of Earth and Planetary Sciences

  Baltimore, MD, USA

- **Dr. Nathan T. Bridges** *(deceased April 26, 2017)*

  Co-Advisor & Research Assistant Professor

  The Johns Hopkins University

  Morton K. Blaustein Department of Earth and Planetary Sciences

  Baltimore, MD, USA

  Senior Professional Staff

  The Johns Hopkins Applied Physics Laboratory

  Laurel, MD, USA

- **Dr. Olivier S. Barnouin**

  Co-Advisor & Research Assistant Professor

  The Johns Hopkins University

  Hopkins Extreme Materials Institute

  Baltimore, MD, USA

  Senior Professional Staff

  The Johns Hopkins Applied Physics Laboratory

  Laurel, MD, USA

ACKNOWLEDGEMENTS

Earning a PhD in a space-related field has been one of my driving goals since high school. My parents, Dan and Renée Runyon, can attest to this, and so I owe them the highest thanks for their support. Though their professional interests are in the humanities, they always fostered my love for science. My support community of friends from Church of the Resurrection in Lutherville have constantly supported me the last few years even if they didn't know it at the time. Special thanks to Rev. David Drake, Dedi Whitaker, Drew Martin, Joel Miller, Stephen & Megan Rigos, Caleb Wang, Jenny Geilfuss, Katie Black (Dirty 30!), Emily Philpot, Erin Haynes, Maria Czajkowski, Vince Clews, Lauren Raymond, and many others. Their prayers and friendship buoyed me through both troughs of despair and peaks of delight.

Exploring other planets and getting paid for it (wow! I can't believe I get to do that!) is like playing in God's playground, and so I return thanks to him for a mind to think and eyes to see and a heart to love and a mouth to speak about these worlds.

I thank the community at Mobtown Ballroom for offering a sublime venue to swing dance and use that other part of my brain and for making me accidentally smile. Special shout out to Hannah Huguenin.

The past and current students in EPS, especially Dana Brenner, Hannah Susorney, Dr. Scott Guzewich, Dr. Lynnae Quick, Dr. Sophie Lehmann, Fang Huang, Jihua Hao, Alexi Russell, and Nate Towles.

The APL staff in SRE have earned my thanks. Even though I didn't do research with them, they all took a hand in mentoring me. I thank especially Scott Murchie, Casey

Lisse, Dave Blewett, Dave Humm, David Lawrence, Ralph Lorenz, Ben Bussey, Louise Prockter, Angela Stickle, Carolyn Ernst, Jorge Nuñez, Karl Hibbitts, and others.

Penultimately, my graduate committee of Bruce Marsh, Nathan Bridges, and Olivier Barnouin deserve my heart-felt thanks. They have encouraged, sharpened, and mentored me. I also very much appreciate their patience with me.

Finally, I wish to emphasize the role that the late Nathan Bridges played in my career. He unexpectedly passed away several hours after I presented this thesis. His sudden departure shocks and saddens me, yet I feel a resolve to carry on the torch of his scientific interests and career in my own. I will always fondly remember him with gratitude for teaching me his trade.

TABLE OF CONTENTS

LIST OF TABLES

LIST OF FIGURES

Chapter 1: Introduction

1.1 Mars and Aeolian Geology

Of the six terrestrial planets in the inner Solar System (Mercury, Venus, Earth, Moon, Mars, and Ceres), Mars has attracted the most interest in exploration and speculation about extraterrestrial life. This claim is substantiated in the present day, reflected in the number of spacecraft at Mars and the amount of money dedicated to Mars science and exploration in both robotic and human spaceflight programs in the United States and internationally.

Along with the prospects for life, the role of water in Mars' geosphere and putative biosphere garners widespread attention. However, water is not the most active agent shaping the modern or even past Mars: wind-blown sand and dust has been the most active geologic process for the last ~3 billion years (the Amazonian epoch). The term given to wind-blown geology is "aeolian," named after Aeolus, the mythical Greek god of wind. In the sweep of the history of Mars science, understanding aeolian morphodynamics is among the oldest problems, though it was not always recognized as such. Week-long and seasonal albedo changes on Mars were often ascribed to dust storms and Martian vegetation (e.g., Tombaugh, 1950; Sinton, 1959). Of course, no life is known to exist on Mars and the visual changes ascribed to vegetation can be explained by seasonal erosion and deposition of dust and sand.

Extensive regions of sand dunes and sand sheets cover Mars in over 550 discrete fields in the non-polar zones (between 65˚ north and south; Hayward et al., 2006). Presumably, the sand that forms these dunes and sheets travels in the same sort of paths

as they are known to on Earth. Broadly, these sand transport mechanisms are called saltation, reptation, and creep (e.g., Anderson, 1987; Kok et al., 2012).

While I present the following as a brief introduction to these issues, I commend to your aeolian edification the excellent descriptive and quantitative review by Kok et al. (2012). As the strength of the wind approaches the threshold necessary to initiate sand grain movement, sand grains begin to roll, bounce, and tumble along the bed as blown by the wind; this is the mechanism of creep. When the wind strength surpasses some threshold, such grains become lofted on nearly vertical trajectories and then become accelerated downwind, re-impacting the surface at low angles <10˚; this is saltation. The grain may rebound on another saltation trajectory or displace local grains on short, ballistic hops that are only slightly affected by the wind. These short hops embody the process of reptation. Broadly speaking, saltation, reptation, and creep together allow the formation of dunes (explained further in Chapter 3) whereas reptation—while driven by saltation—is credited for the formation of and migration of ripples. Thus dunes and ripples are not large and small versions of each other.

With sand's erosion and deposition being mediated by a planet's atmosphere, aeolian geology brings together the disciplines of geology and climatology. Atmospheric circulation models and wind measurements compliment and inform observations of sand movement and the sometimes enormous accretions of sand dunes. This field's pioneering work is rightly attributed to Ralph Alger Bagnold (1941, 1954) who succinctly described sand grain motion in air, the formation and morphology of ripples, and the formation and morphology of large-scale dunes. While his initial work in aeolian geology has required only minor corrections, most contemporary work simply builds off his foundation, which

also serves as a starting point for studying aeolian geology on other planets, most notably Mars. Appropriately, Bagnold co-authored one of the first works on Martian aeolian dynamics with Carl Sagan (Sagan and Bagnold, 1975).

Motivating the study of Martian grain movement was the discovery a few year's prior of aeolian bedforms in images from the first Mars orbiter, the spacecraft *Mariner 9* (Sagan et al., 1972). Confirmation of *active* bedform movement required waiting 36 years until Bourke et al. (2008) used meter-scale resolution images and multi-year temporal baselines to observe the shrinkage and disappearance of Martian dome dunes. Beginning in 2012, numerous measurements for sand ripple and sand dune migration across Mars showed the planet to be geologically active in very Earth-like ways (e.g., Bridges et al., 2012). Measurements from the ground by the rover *Curiosity* even showed an incipient slip face avalanche in progress on a barchan dune (Bridges et al., 2016).

These active aeolian bedforms obviously indicate a current climate conducive to aeolian activity. Understanding the current aeolian climate allows interpreting paleoclimates recorded in Mars' sedimentary stratigraphy. Aeolian strata exposed in outcrop at the Stimson Formation in Gale Crater indicate past epochs of sand deposition, mobilization, and induration (Banham et al., 2016; Kronyak et al., 2017). The study of sand movement and the resulting geomorphology thus controls modern Mars' evolution as well as informing past climate epochs and the paleogeology. Closing the loop on this thought is the realization that these lithologies may serve as habitats for any Martian microbes, thus underscoring the astrobiological importance of understanding sedimentary geology on Mars.

The knowledge gained from studying Mars primarily from orbit will aid in novel ways to investigate Earth's aeolian systems and their important interactions with the biosphere and anthroposphere. Inaccessible or remote regions of Earth could be more quickly analyzed from Earth-orbital or airborne assets to address ecological, climatological, human usage, or even warfare concerns. With the imminent capability of re-imaging every part of Earth every day at <10 m/px resolution with data from Planet Labs, Inc.'s fleet of CubeSats, the methods of studying Martian aeolian geology will soon see applicability on Earth aeolian geology.

1.2 Ejecta Emplacement on Solid Worlds

Besides the Sun and four known giant planets, every other Solar System object is solid and is therefore subject to the geologic process of impact cratering. Objects are either impactors or targets, though sometimes, for the case of similarly-sized objects, they are both. All solid worlds visited by spacecraft—with the strange exception of Jupiter's satellite planet Io—feature impact craters, and it is thus the most pervasive surface geologic process across the Solar System. Because ejecta from craters extends for many crater radii away from the crater—at least for worlds with sufficient gravity to retain ejecta—the emplacement of ejecta is likewise pervasive as an agent of geomorphic change across the Solar System.

Prior to the mid-20th century, lunar craters were regarded as volcanic in origin, being referred to as "crater-cones" (Elger, 1884). While the overwhelming majority of craters are indeed impact in origin, early workers such as Elger (1884) correctly interpreted variations in albedo as ejecta from craters. My home institution of Johns

Hopkins University has a long history of ejecta studies: as early as 1910, the ejecta surrounding the Moon's Aristarchus Crater were studied by Johns Hopkins' own Professor R.W. Wood at various wavelengths (Wood, 1910). Because ejecta and the craters from which they are ejected are intimately linked, we now turn our attention to an overview of impact cratering.

1.2.1 Terminology

Elasticity and elastic waves refer to a disturbance's propagation through a medium without permanent change, with sound waves through air, water, and solids being the most familiar. Shock waves result when the target experiences more energy than can be accommodated by elastic waves and travel supersonically (relative to the material's sound speed) through the target. As an elastic wave propagates, the compressed region ahead of it grows; in order to accommodate the thickening compressed region the interface between the compressed and uncompressed region must grow and therefore travel faster than the plastic wave. Hence, shock waves are supersonic. Plastic deformation is a permanent volume change in the material as a result of the shock wave's passage. The Hugoniout elastic limit (HEL) is a stress and volume state in which the material stops behaving elastically and starts deforming plastically; shock waves occur above the HEL and elastic waves occur below it.

1.2.2 Overview: The Cratering Process

Contact and Compression: Most planetary impacts Sunward of the asteroid belt occur at hypervelocity and thus shock the targets. As introduced above, shock refers to

imparting enough energy to a target such that the shock wave propagates supersonically, surpassing the Hugoniot elastic limit and causing permanent, plastic deformation at the scale of rocks' mineral crystal lattices. The shock wave radiates into the planet from the impact point; rays drawn perpendicularly to the shock front initially mainly progress deeper, though away from the impact point they curve up toward the free surface. Trailing the shock front, a rarefaction wave also propagates in the same direction although the particle velocities are in the opposite direction as the wave velocity and the rays likewise curve back toward the free surface. These rays, referred to by Melosh (1989) as flow lines, indicate the direction of the particle velocities and, importantly, the sense of the excavation flow field for the ejecta. Shocked target material moves along the flow lines and, if the rarefaction wave overcomes the combined tensile strength of shocked rock and its weight, the material is excavated from the crater. In distal regions from the impact point, the shock and rarefaction waves lack the power to shock and excavate the rock, yet the rock still follows the flow lines but stops short of excavation; hence the uplift of a circum-crater raised rim.

Just as the shock and rarefaction waves propagate into the planet, so shock and rarefaction waves propagate through the (usually) much smaller projectile and often result in its complete destruction. The rarefaction wave passing through the projectile often completely disrupts it. The distance the projectile is able to penetrate before it is destroyed has historically been treated as the depth at which it deposits its energy (Gault et al., 1968).

Modification Stage: The embryonic crater continues to increase in volume through a combination of increasing depth and width. Both excavation and downward

displacement of material contribute to the crater's deepening, with excavation contributing ~2/3 and displacement contributing ~1/3 to the volume. The crater reaches a maximum depth and then begins to collapse (shallow) even as it continues to widen (Barnouin-Jha et al., 2007). The degree of collapse depends upon the planet's gravitational strength and the width of the crater, leading to simple craters, complex craters, peak ring basins, and multi-ring basins, listed in order of size. Simple craters are bowl shaped with depth-to-diameter aspect ratios between 0.1 and 0.2. Complex crater walls lack strength for self-support and so undergo normal faulting, resulting in terraces; a central mountain peak near the crater's center results from crustal rebound. When the crustal rebound becomes extreme and the central peak's weight overcomes the rock strength, it partially collapses to form one or multiple concentric orogenic annuli, thus forming peak-ring or multi-ring basins (French, 1998). Craters larger than simple craters have shallower depth-to-diameter aspect ratios, typically around 0.05.

This initial modification stage typically lasts on order minutes from the time of impact. However, continued modification may continue indefinitely through crustal relaxation and viscous creep. These processes slowly act to "erase" craters by floor uplift and rim collapse.

1.2.3 The Ejecta Curtain

When the rarefaction wave excavates a cavity, most of the material is ejected at an angle of around 45˚ (following ballistic trajectories—for the most part. Factors to cause ejecta particles to deviate from ballistic trajectories include atmospheric drag

(where applicable) and grain-to-grain interactions during flight that convert kinetic energy to heat. Both these factors can cause ejecta to land short of ballistic prediction). Broadly, however, ejecta particles can be considered to travel in ballistic trajectories and land a predictable distance from the crater; from simple ballistics considerations (Melosh, 1989), this range is

$range = U^2 \sin(2\theta/g)$

where θ is the launch angle (again, typically 45˚), g is the planet's gravity, and U is the launch velocity. The individual particles in aggregate resemble an inverted cone sweeping across the planet's surface, depositing itself and mixing with the *in situ* material. This has historically been referred to as an ejecta blanket, but given the heterogeneous mixture with the pre-impact material, the term ejecta deposit or facies is more accurate.

For gravity-dominated craters (when the strength of the rock relative to gravity is not important), observed ejecta deposits appear self-similar; that is, there remains a fixed ratio between ejecta range and crater radius. Self-similarity is violated, however, for smaller craters within the strength regime (where the strength of the rock relative to gravity is important); for the Moon, this corresponds to a radius of about 500 m. This is due to the growing crater encroaching into just-deposited ejecta and "eating" away at the most proximal ejecta deposit (Melosh, 1989).

The volume of ejecta falls off as $1/r$ away from the crater such that 50% of the ejecta falls within the crater rim and one crater radius R away (Melosh, 1989). However, in the gravity regime, for a given fractional crater radius from the rim for larger craters, the ejecta will land with greater speed and can therefore slide further, serving to thin the

ejecta deposit and incorporate pre-existing material into the ejecta deposit. This post-deposit sliding obfuscates thickness profile predictions.

The rest of my cratering considerations in this Thesis will be with regard to the deposit and flow of the ejecta curtain within several crater radii from the rim. The impact of granular ejecta particles are subsonic and thus do not create shock waves in the ground when they re-impact. However, the deposition and sliding of ejecta is still an energetic and violent process and could be regarded as an "avalanche from the sky."

1.3 Comparison Between Aeolian and Ejecta Geology

Though traditionally treated as separate topics, the emplacement and transport of crater ejecta following crater excavation and the formation and movement of aeolian bedforms share fundamentally common physical considerations: those of intergranular interactions between lofted grains and stationary surface grains.

Both processes dominate surface geomorphic processes, though on different time scales. On the present Mars, aeolian modification of the surface is the most active ongoing geologic process (e.g., Cabrol et al., 2014), and this is likely true for equatorial regions of Titan (Burr et al., 2015). Ancient Mars, however, was likely more influenced from "late stage accretion," or rather the proposed Late Heavy Bombardment ~4 Ga consisting of basin-forming impactors.

The resulting geomorphological differences between crater ejecta dynamics and wind-blown sediment are significant, although both are critical in deciphering past and present landscape modification. In the case of crater ejecta, understanding its deposition informs provenance analysis, lunar highlands-lowlands mixing (e.g. Li & Mustard,

2005), crater rim uplift mechanics (Sharpton, 2014), and overall landscape and near subsurface evolution. In contrast, aeolian sediment transport forms meso-to macroscale bedforms such as ripples, dunes, and sand sheets; abrades rock into ventifacts and yardangs; and erodes surfaces, all contributing to crater degradation on Mars, Venus, Titan, and Earth. Also, unlike crater ejecta, aeolian bedform migration informs wind direction and strength, serving to constrain numerical atmospheric circulation models. Lithified aeolian bedforms and paleo-ejecta facies in stratigraphy preserve records of past aeolian climates and impact events, respectively, thus linking modern dynamical observations to the rock record.

For all solid worlds throughout the Solar System and within the sweep of its 4.5 billion year history, impact cratering and the resulting ejecta emplacement have been the most dominant geologic process. For the four planets with both surfaces and atmospheres, wind-blown sediment has largely held sway for billions of years. It seems fitting, then, to focus on two of the Solar System's most dominant surficial geologic processes for this Thesis.

References

Anderson, R.S., 1987. A theoretical model for aeolian impact ripples. Sedimentology, 34, p. 943-956, doi:10.1111/j.1365-3091.1987.tb00814.x.

Banham, S.G., et al., 2016. Reconstruction of an ancient eolian dune field at Gale Crater, Mars: Sedimentary analysis of the Stimson Formation. Lunar and Planetary Science Conference, Abstract #2346.

Bagnold, R.A. 1941, 1954. The physics of blown sand and desert dunes. Metheun, London, 265 pp.

Barnouin-Jha, O.S., Yamamoto, S., Toriumi, T., Sugita, S., Matsui, T., 2007. Non-intrusive measurement of crater growth. Icarus, 188, doi:10.1016/j.icarus.2007.01.009.

Bridges, N.T., et al., 2012. Earth-like sand fluxes on Mars. Nature 485, 339. http://dx.doi.org/10.1038/nature11022.

Bridges, N.T., et al., 2016. Investigation of the Bagnold Dunes by the Curiosity rover: Overview of initial results from the first study of an active dune field on another planet. Lunar and Planetary Science Conference, Abstract #2298.

Burr, D.M., Bridges, N.T., Marshall, J.R., Smith, J.K., White, B.R., Emery, J.P., 2015. Higher-than-predicted saltation threshold wind speeds on Titan. Nature, 517, 60-63, doi:10.1038/nature14088.

Cabrol, N.A., et al., 2014. Sands at Gusev Crater, Mars. Journal of Geophysical Research Planets, 119, doi:10.1002/2013JE004535.

French, B.M., 1998, Traces of catastrophe: A handbook of shock-metamorphic effects in terrestrial meteorite impact structures: LPI Contribution No. 954.

Gault, D.E., Quaide, W.L., Oberbeck, V.R., 1968. Impact cratering mechanics and structures. In: Shock metamorphism of natural materials. B.M. French and N.M. Short, eds. Mono Book Corp.

Hayward, R.K., et al., 2006. Mars global digital dune database: MC2-MC29. U.S. Geological Survey Open-File Report 2007-1158. http://pubs.usgs.gov/of/2007/1158/.

Kenkmann, T., Ivanov, B.A., 2006. Target delamination by spallation and ejecta dragging: An example from the Ries crater's periphery. Earth and Planetary Science Letters, 252, 15-29, doi:10.1016/j.epsl.2006.08.024.

Kok, J. F., Parteli, E.J.R., Michaels, T.I., Bou Karman, D., (2012), The physics of wind-blown sand and dust, Reports Prog. Physics, 75, doi:10.1088/0034-4885/75/10/106901.

Kronyak, R.E., et al., 2017. Capping unites of the Murray Formation, Gale Crater, Mars: Salsberry Peak as a pre-Stimson Formation caprock. Lunar and Planetary Science Conference, Abstract #1523.

Melosh, H.J., 1989. Impact cratering: A geologic process. Oxford University Press (Oxford Monographs on Geology and Geophysics, No. 11), 1989, 253 p.

Sagan, C., Veverka, J., Fox, P., Dubisch, R., 1972. Variable features on Mars: Preliminary Mariner 9 television results. Icarus, 17, 2, p. 346-372, https://doi.org/10.1016/0019-1035(72)90005-X.

Sagan, C., and Bagnold, R.A., 1975. Fluid transport on Earth and aeolian transport on Mars. Icarus, 26, 209-218, https://doi.org/10.1016/0019-1035(75)90080-9.

Sinton, W.M., 1959. Further evidence of vegetation on Mars. Lowell Observatory Bull., 103, 4, 15, p. 252-258.

Tombaugh, C.W., 1950. Geological interpretations of the markings on Mars. Harvard Astron. J., 55, 1186, p. 184.

Wood, R.W., 1910. Moon in yellow and ultra-violet light. Monthly Notices of the Royal Astronomical Society, 70, p. 226,

http://articles.adsabs.harvard.edu//full/1910MNRAS..70..226W/0000226.000.html.

Chapter 2: An integrated model for dune morphology and sand fluxes on Mars

K. D. Runyon, N. T. Bridges, F. Ayoub, C. E. Newman, and J. J. Quade

Key words: Aeolian; Mars; Climate; Stratigraphy; Surface Processes; GCM

Key Points:

- Mars dune fields exhibit a downwind evolution in morphology and sediment flux
- Internal boundary layer theory and slope speedup explain observed sediment flux
- These findings have implications for interpreting Martian stratigraphy

Publication History

This chapter was originally published as a paper in the journal Earth and Planetary Science Letters 457, p. 204-212 (2017), http://dx.doi.org/10.1016/j.epsl.2016.09.054.

Permission was granted by the publisher for this paper's inclusion in this Thesis.

Abstract

The transport and deposition of sand is the most prevalent agent of landscape modification on Mars today, with fluxes comparable to some sand dunes on Earth. Until now, the relationship between sand flux and dune field morphology has been poorly constrained. By tracking dune movement over ~10 km-long dune fields in Herschel Crater and Nili Patera, representative of many dune fields on Mars, we find a downwind flux decrease that correlates with a sequence of changing morphology from barchans to barchanoids and seifs (longitudinal dunes) to isolated dome dunes and ending with sand sheets. We show empirical consistency with atmospheric Internal Boundary Layer (IBL) theory which can describe these broad flux and morphology changes in Martian dune fields. Deviations from IBL flux predictions are from wind streamline compressions up slopes, leading to a speedup effect. By establishing a dune field morphology type example and correlating it with measured and predicted flux changes, we provide an integrated morphology and flux model that can be applied to other areas of Mars and be used to infer paleo-environmental conditions from preserved sandstone.

2.1. Introduction

2.1.1. Martian Aeolian Environments

The Mariner 9 orbiter returned the first data indicating the presence of aeolian bedforms on Mars (*Sagan et al.,* 1972). Sand dunes are now known to cover all major latitude zones (*Hayward et al.,* 2007) and are common in craters, basins, the north polar region, and in the lee of topographic obstacles such as crater rims. With the exception of vegetated (e.g. parabolic) dunes, all of Earth's dune forms are represented on Mars:

barchan, barchanoid, transverse, seif (or longitudinal), star, reversing, and dome. Mars' dunes are mobile and are not relicts of past Martian climates (*Silvestro et al.*, 2010; *Bridges et al.*, 2012). In contrast to Earth, the aeolian processes responsible for dunes and other bedforms on Mars are unhindered by most other geomorphic agents, especially water. Indeed, on Mars the movement of sand and dust is the dominant process of geomorphic change in the current climate. The inferences gained from understanding regional and global sand transport pathways and erosional regimes provide constraints on current and past Martian climate (e.g. *Grotzinger et al.,* 2005) and landscape evolution, in particular interpreting aeolian stratigraphy (*Grotzinger et al.,* 2013; *Milliken et al.,* 2014) and reconstructing paleoclimates, as has been done in terrestrial aeolian systems (*Hunter,* 1977; *Clemmensen and Abrahamsen,* 1983; *Eastwood et al.,* 2012).

Given the need to understand modern dune patterns and sand flux variations, and to interpret paleoenvironments evidenced in sandstone stratigraphy, we establish links between modern sand fluxes, dune morphology sequences, dune height, and flux predictions from Global Circulation Models (GCMs). By combining the results of surface roughness changes and the GCM, we show consistency between measured and predicted fluxes for three sites. Two aeolian regions on Mars within the 300 km-diameter Herschel Crater (centered at 14˚S, 130.1˚E) and one region within the Nili Patera caldera (8.8˚N, 67.3˚E) serve as these case studies (Figure 2.1), in which we used HiRISE (the High Resolution Imaging Science Experiment (*McEwen et al.*, 2007)) images to measure dune height (from stereo digital elevation models), dune slip face advancement (Figure A1), dune morphology (Figure 2.2), ripple migration (Figure 2.3), and dune volumetric crest flux across temporally-spaced images (see Appendix A).

The western and eastern Herschel Crater and the Nili Patera dune fields show similar dune morphological trends downwind in which the dune morphologies transition from classical barchans to sand sheets (Figure 2.2) and have been described by *Cardinale et al.* (2012; 2016). We identify this morphological trend as an illustrative type-example of dune field (Figure 2.2). Importantly, their upwind margins are sharply defined and they all sit on bedrock as opposed to a sandy substrate.

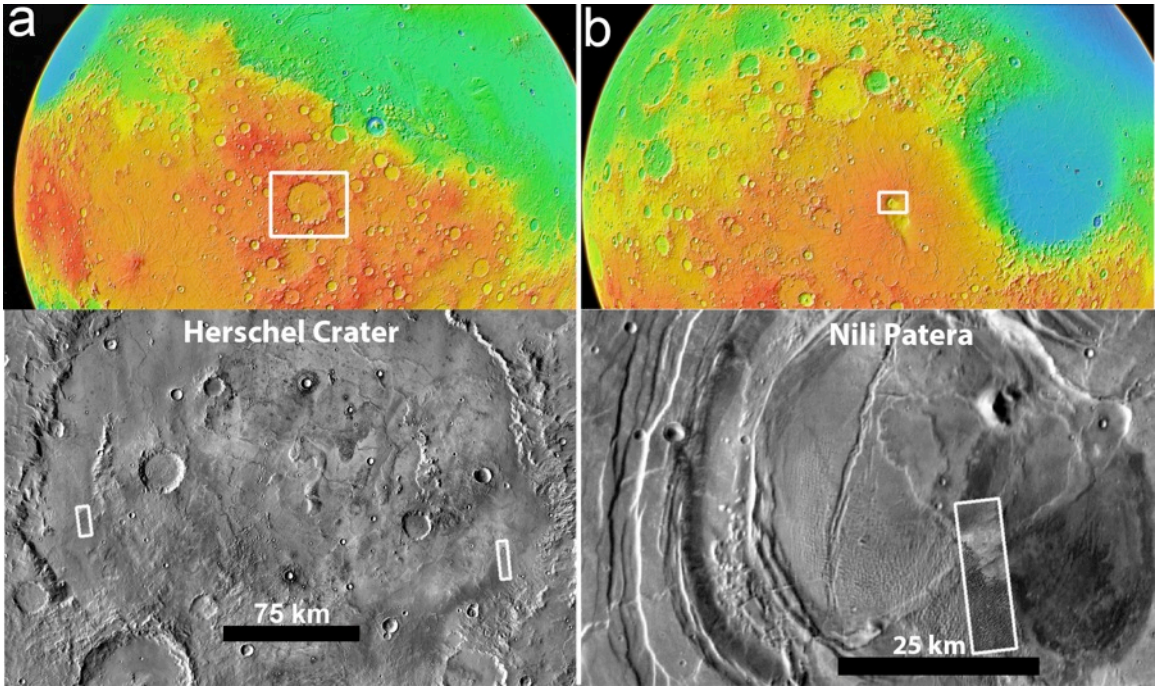

Figure 2.1. An overview of the locations (white boxes, top) of (**a**) Herschel Crater and (**b**) Nili Patera. Western and eastern Herschel dune fields are boxed in the lower blow-up of Herschel (**a**), corresponding to available HiRISE coverage. Global views are MOLA colored topography from GoogleMars where warm colors indicate higher elevations than cooler colors. Regional images are HiRISE embedded in daytime THEMIS mosaics from JMARS (*Christensen et al.,* 2009). North is up.

Geomorphologically, some dunes exhibit asymmetry. Asymmetric barchans in western Herschel alternate between the west and east horns being longer whereas in eastern Herschel the west horns are more consistently longer. Dunes in Nili Patera, in contrast, are highly symmetric with relatively few dunes exhibiting horn asymmetry. Whereas our case study sites are constrained by the HiRISE footprints (necessary for temporal comparison of small scale features), broader Context Camera (CTX; (*Malin et al.*, 2007)) images reveal the dune fields extending for many kilometers with the same broad morphological evolutionary sequence. Within this broader view provided by CTX, the long axes of barchans rotate a few degrees, suggesting a regionally varying resultant sand transport azimuth; this is substantiated by *Cardinale et al.'s* (2016) measurement of slip face directions.

2.1.2. Internal Boundary Layer Theory Applied to Aeolian Systems

Atmospheric and field studies on Earth show that flat-plate internal boundary layer (IBL) theory applied to the inland White Sands dune field accurately predicts the measured sand fluxes downwind and that this flux decrease corresponds to a spatially evolving dune morphology (*Jerolmack et al.,* 2012; *Anderson and Chemacki*, 2014); this has also been applied to coastal aeolian systems (*Rasmussen*, 1989). Dunes acting as roughness elements to the oncoming wind reduce the wind's shear stress downwind, either from the initial upwind roughness transition (*Jerolmack* et al. 2012) or from the field-wide roughness (*Pelletier*, 2015). Either way, the heterogeneous dune roughness controls IBL flow, shear stress, and therefore sediment flux at White Sands (*Pelletier*, 2015).

An IBL forms when an increase in surface roughness, such as the wind transitioning from blowing over bedrock to dunes, acts as a momentum sink and greatly increases turbulence (*Anderson and Chemacki*, 2014). At least one manifestation of this turbulence is in the form of Kelvin-Helmholtz instability rollers which form behind upwind dunes and impinge upon downwind dunes (*Anderson and Chamecki,* 2014). Due to turbulence and drag, momentum retardation diffuses upward and advects downwind such that the IBL thickens downwind (*McLean and Smith*, 1986). The region within the IBL is thus where the speed and shear stress are significantly different from upwind conditions (*Garratt*, 1990). The downwind thickening of the IBL occurs within the Atmospheric (or Planetary) Boundary Layer (ABL), which is a well-mixed turbulent layer of atmosphere between the Sun-heated ground and the stably stratified free atmosphere above. ABLs can be several km thick, and depending on the heat capacity of a planet's atmosphere may collapse (e.g. *Savijarvi and Maattanen*, 2010) to nearly zero height above the ground at night, as is often the case on Mars and is in accordance with our GCM.

Inspired by a similar geomorphological sequence observed at White Sands (*Kocurek et al.,* 2010; *Jerolmack et al.,* 2012) as in our Martian case study sites, we test the hypothesis that IBL theory can likewise describe the measured flux changes. *Cardinale et al*. (2016) hypothesized IBL-controlled sand fluxes for Herschel Crater dunes but did not test the hypothesis. Our work is the first time IBL theory has been quantitatively applied to Martian dune fields and correlated with spatially evolving dune morphologies downwind.

In addition to applying the "Jerolmack IBL flux model" to our case study sites, we also model the pronounced effect of dune topography on wind speed and flux: *Pelletier* (2015) notes that topographic ridges within White Sands locally enhance shear stress and therefore sand flux from streamline compression. We therefore add the prediction that flux deviations from IBL theory ("noise") can be partly explained by wind streamline compressions from local slopes (*Jackson and Hunt,* 1975; *Frank and Kocurek*, 1996; *Momiji et al*., 2000; *Gao et al.,* 2015) which operates as a secondary mechanism to the large-scale, dune field-wide IBL. The slope speedup occurs within a smaller, "nested" IBL on each dune (*Frank and Kocurek,* 1996).

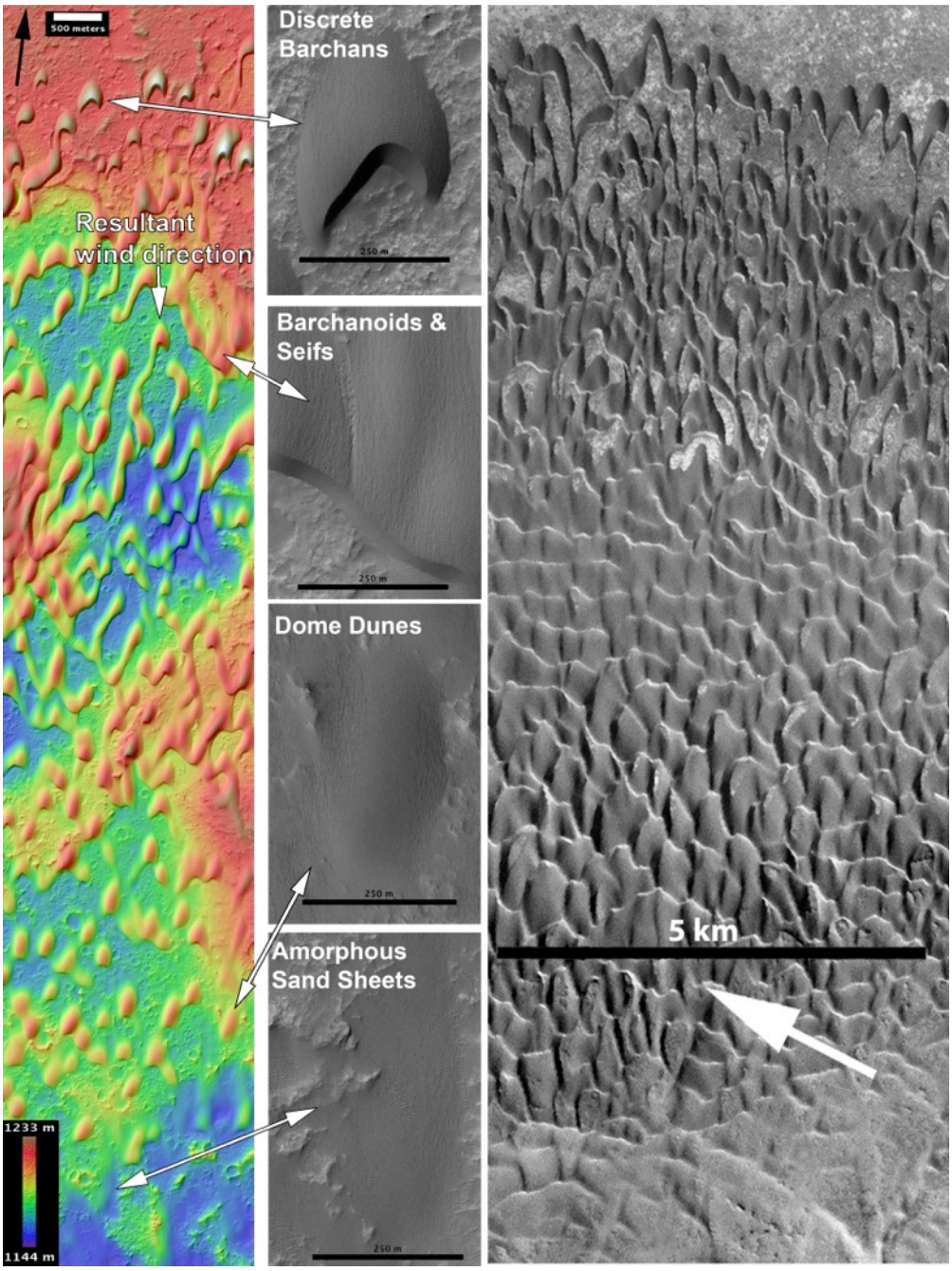

Figure 2.2. The western Herschel Crater dune field (far left, height-colorized HiRISE DEM) and Nili Patera dune field (far right, CTX image) are type examples of a changing morphology downwind from barchan, to barchanoid and seif, to dome dunes, to sand sheets, each with successively lower heights and sand fluxes (north is indicated in each with a single-ended arrow; they have been rotated so that "downwind" is down). The

term “downwind” is with regards to the apparent resultant transport direction evidenced by dune orientation. Less frequent but obliquely-blowing winds (up to angles > 90˚) likely produce asymmetrical dune elongation (*Courrech du pont* et al., 2014), but obliquity effects are averaged over the several years between observations. The effect of obliquity on our IBL model may be to merely add a noise component. This morphology change is consistent with a decrease in downwind sand flux from the formation of an IBL, as observed at the White Sands dune field on Earth (*Jerolmack et al.,* 2012). Note that the DEM is absolute elevation above Mars’ datum. DEM credit: NASA/University of Arizona/USGS; HiRISE subscenes from PSP_002860_1650; CTX image B21_017762_1891_XN_09N292W, Credit: NASA/MSSS.

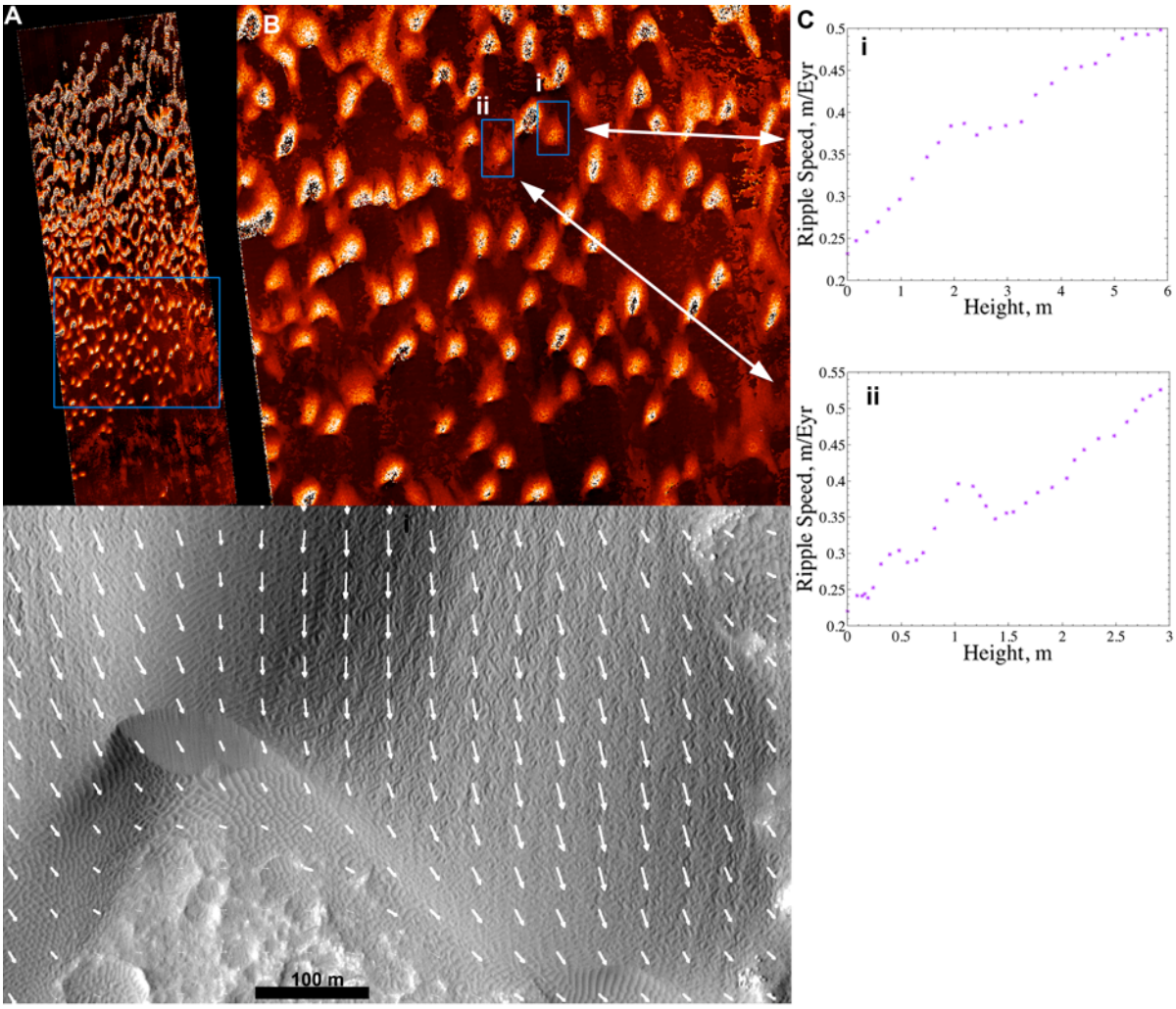

Figure 2.3. (**A, B**) A ripple displacement map of the western Herschel Crater dune field that has been covered by repeat HiRISE imagery. Brighter tones indicate greater ripple displacements (mostly north to south); speckled patterns indicate that ripples moved further than could be tracked by the COSI-Corr algorithm (see Methods). The HiRISE image is ~5 km across. (**C**) Ripple speeds (3.74 Earth years between images for western Herschel) increase up dunes' stoss slopes; this is likely from a wind speedup effect due to streamline compression up positive topography. *Bridges et al.* (2012) also found this to be the case on sand dunes in Nili Patera. (D) Ripple displacement vectors across dune (i) and its western companion dune. North is up.

IBL theory predicts average sand flux $\langle q_s \rangle$ as a function of distance downwind within an IBL as (*Jerolmack et al.,* 2012)

$$\langle q_s \rangle = 0.055 I \frac{\rho_{\text{atmo}}}{\rho_{\text{solid}}} \frac{C}{g} \sqrt{\frac{D}{D_0}} U^3 \left(\frac{\nu}{U z_{0L}^{1/5}} \right)^{3/8} x^{-3/10} \quad \text{(Eq. 1)}$$

where the ρ_{atmo} and ρ_{solid} are the atmospheric and grain densities, respectively; C is the aerodynamic drag coefficient; g is gravity; D is the characteristic sand grain size; D_0 is the standard reference grain size; U is the free stream air velocity at the top of the ABL, $\boldsymbol{\nu}$ is the atmospheric kinematic viscosity; z_{0L} is the Lettau roughness height (*Lettau,* 1969); x is the distance downwind starting at the upwind tip of the dune field; and 0.055 is an empirical constant that is notably 10 times larger than the value used on Earth by *Jerolmack et al*. (2012) and its use is further justified in Appendix A. This flux value is then multiplied by 3.154×10^7 s Earth-year^{-1} to give flux in units of m^3 m^{-1} Earth-year^{-1}. The variables are given in Table A1 and the sediment mobility intermittency I is considered below (Appendix A, Figure A2 ,Table A2).

The sediment mobility intermittency I is the fraction of time that sediment is mobilized by the wind and is related to the time-averaged dune field flux $\langle q_s \rangle$ as (*Jerolmack et al.,* 2012)

$\langle q_s \rangle = I q_{\text{instantaneous}}$.

The value *Jerolmack et al.* (2012) measured *in situ* at White Sands is $I = 0.03$, meaning that sediment moves 3% of the time.

The free stream velocity U associated with sand flux in Equation 1 is the unencumbered wind speed at the top of the ABL (the base of the stably-stratified free atmosphere) and is given by the law-of-the-wall

$$\boldsymbol{U = \frac{u_a^*}{\kappa} \ln\left(\frac{z}{z_{0L}}\right)} \quad \text{(Eq. 2)}$$

and is calculated from the average above-critical friction speed u^*_a from the GCM. The von Kármán constant $\kappa = 0.4$, z is ABL height, and z_{0L} is the Lettau roughness height (*Lettau,* 1969) (Appendix A, and Tables A1-A2). Atmospheric densities $\boldsymbol{\rho_{atmo}}$ are Martian-yearly averages corresponding to above-critical shear stresses for the study sites ranging from 1.3-1.5 $\times 10^{-2}$ kg m^{-3} as output from the GCM. Terrestrial deserts have ABL heights 1-3 km above the ground (*Lorenz & Zimbelman,* 2014) whereas from our GCM, Mars ABL heights are ~9-11 km high. For our Herschel and Nili case study sites using $u^*_a \sim 1.1$ m s^{-1} from our GCM, the estimated free stream velocities 10 km high are ~24-27 m s^{-1}. This compares favorably with the terrestrial value of 20 m s^{-1} 1.9 km high for White Sands, NM (*Jerolmack et al.,* 2012).

2.1.3. Slope Speedup and the Integrated Model

Our accounting for topographic wind speedup has its precedent in field, laboratory, and theoretical studies: terrestrial anemometer measurements (*McKenna Neuman et al.,* 1997) document accelerated wind speeds up reversing dune stoss slopes which agree with dune wind models (*Momiji et al.,* 2000). On Mars, slope-induced streamline compression accounts for the observation that ripples accelerate upslope (*Bridges et al.,* 2012). Several authors have discussed speedup ratios or speedup factors for wind blowing over hills and bedforms (e.g. *Jackson and Hunt*, 1975; *Momiji et al.*, 2000; *Gao et al.,* 2015; *Pelletier,* 2009; *Lancaster*, 1985), and *Pelletier* (2015) discusses the importance of wind flow line convergence (i.e., streamline compression) up slopes and the resulting increase in wind shear stress. Modeling wind speedups from

topographic slopes goes back to at least the 1970s with civil engineering applications in mind (*Jackson and Hunt,* 1975), though not all authors relate wind speedups with explaining increases in sand flux; authors that do include, e.g. *McKenna Neuman et al*. (1997), *Wiggs et al*. (1996), *Pelletier* (2015), *Momiji et al.* (2000), and *Bourke et al.* (2004). Given the higher shear stress and sand mobilization potential of topographically-accelerated wind, we consider a wind speedup factor in which 1 indicates no speedup, larger than 1 indicates speedup, and factors 0-1 indicate slowdown, such as for streamline divergence in the lee of topography (*Lancaster,* 1985). We use the speedup factor to modify U used in the IBL flux prediction (Equation 1) along a topographic transect and thus add to the Jerolmack IBL flux model to better explain the scatter in flux data. Figure 2.4 illustrates our model conceptually for dune flux evolution and describes the downwind morphological evolution in sand dunes and changes in crest flux by invoking an IBL modified by both bedrock and dune topography. The downwind-thickening IBL lowers flux, resulting in progressively smaller dunes downwind that eventually lack slip faces, which give way to sand sheets. Dunes perched on positive topography may experience higher sand fluxes because the streamline compression partially offsets decreases in wind speed. However, at sufficient height, the dunes should erode due to higher wind shear stresses which prevent deposition; this acts to limit dune height growth (e.g. *Kok et al.,* 2012).

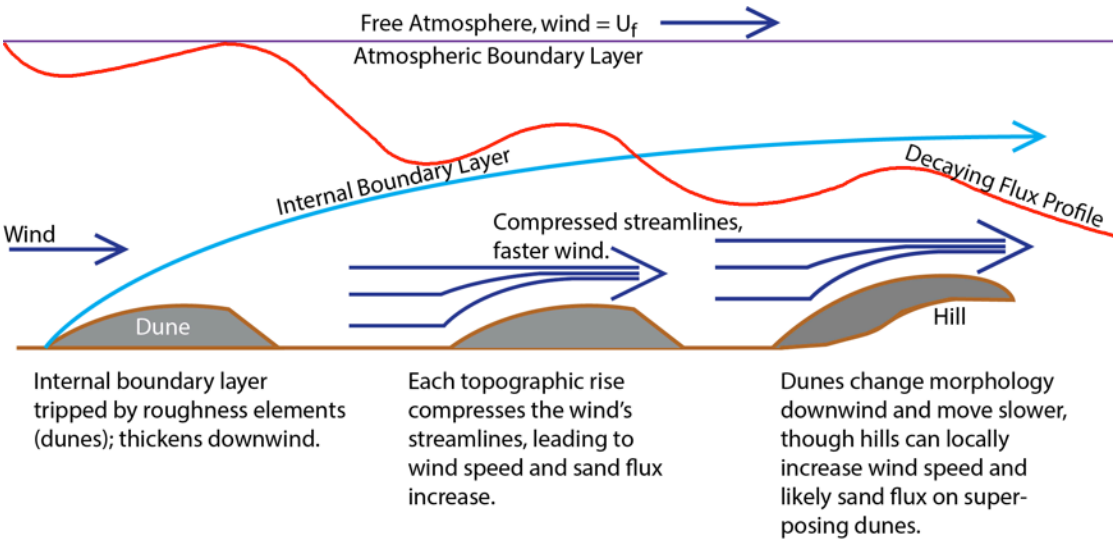

Figure 2.4. Conceptual model illustrating IBL formation and topographic wind speedup effect as competing phenomena. The left-most upwind dune serves as a roughness element to trip an IBL which thickens downwind (toward the right). Each topographic rise (dune or bedrock) compresses the wind's streamlines, leading to wind speed, shear stress, and sand flux increase at a local scale; our use of the panel method does not consider the low slopes of the broad wavelength topography. The bulk motion of dunes slows and the dune morphology changes further afield as the IBL thickens. The wavy red curve illustrates the combined sand flux effects from the IBL and the streamline compression with an overall flux decrease that follows a power law but with dune-scale flux increases.

2.2. Methods

2.2.1. Measuring topography and bedform displacement

The HiRISE camera, orbiting Mars on the Mars Reconnaissance Orbiter (MRO), provides ground imagery of ~0.25 m/px and derived Digital Elevation Maps (DEMs)

with post spacings of 1 m/px and 10s of cm of vertical precision, processed from stereo pairs (*Kirk et al.,* 2008). We re-projected HiRISE images onto stereo HiRISE-derived DEMs to create orthoimages, thus allowing for subpixel co-registration of images separated in time using the ENVI plug-in Co-registration of Optically Sensed Images and Correlation (COSI-Corr) (*Leprince et al.,* 2007). Thus, we used three HiRISE images per area for a total of nine HiRISE images for this study: two images to build a DEM and the first and third images for both manual change detection of slip faces and automatic change detection of ripple patterns using COSI-Corr in the manner of *Bridges et al.* (2012). We mapped the location of barchan dune slip faces along a downwind transect in both time-separated images (Figure A1) and divided the area of slip face advancement by the arc length of the active slip face, arriving at a characteristic displacement for a particular dune. Dividing by the time interval between images gives bulk dune speed; multiplying by dune crest height as measured from the DEM yielded dune crest flux.

2.2.2. Global Circulation Model and Grain Mobility Intermittency

In lieu of *in situ* wind speed measurements that are lacking at the Martian sites, we used a 2-degree resolution GCM to produce atmospheric predictions for our case study in Nili Patera and a 0.074-degree resolution nested mesoscale domain inside the GCM for our studies in Herschel Crater. At each grid point, the predicted friction speed u^* and near-surface air density ρ_a were output every three Mars hours (1 Mars hour = 1/24 of a sol) for one Mars year. The output from all grid points in each study region was then used to produce a combined wind shear stress histogram (1000 bins) for that region, where wind shear stress $\tau = \rho\, u^{*2}$. We used an effective critical shear stress τ_c of 0.01 ±

0.015 N m^{-2} which parameterizes both the initiation and continuation of basaltic sand grain movement ($\boldsymbol{\rho_{basalt}}$= 2850 kg m^{-3}). This value of τ_c resulted in the best match between the seasonality of observed sand fluxes in Nili Patera and those predicted by the same GCM used in this study (*Ayoub et al.,* 2014). *I* is derived from integrating and ratioing the wind shear stress histogram for all shear stresses and those only at and above threshold, thereby yielding the fractional time that wind is above τ_c. (We describe the detailed computation of *I* in Appendix A, and Figure A2, and Table A2.) The intermittency values are lower bounds since the wind stresses predicted by the GCM do not account for mesoscale and higher resolution effects such as local turbulent lee eddies (*Anderson and Chemacki*, 2014; *Palmer et al.,* 2012) and small-scale slope-induced wind speed changes; this may be a source of flux under-prediction. For western and eastern Herschel and Nili Patera, the average computed intermittency values are ~0.8%, 2.5%, and 9.2%, respectively, assuming a mean critical threshold shear stress of τ_c = 0.01 N m^{-2}. These values for *I* compare with 3% (0.03) measured at White Sands (*Jerolmack et al.,* 2012). We also used u^* from the GCM to calculate the free stream velocity, *U* at the top of the ABL (Equation 2) and the predicted IBL-controlled flux (Equation 1).

2.2.3. Wind Speedup from the Panel Method

Whereas much work (e.g. *Anderson and Chemacki*, 2014; *McLean and Smith*, 1986; *Palmer et al.*, 2012) was focused on wind speed and turbulence effects from dune topography, many of these studies did not make the less-clear link from wind speed to sand flux. To calculate the amount of wind speed increase, we assume incompressible and inviscid air flow, topographic rise ("bump") symmetry, and discretize the bumps into

"panels." Each bump is regarded as a symmetric isosceles triangle. Even though topographic features are not necessarily symmetric, the symmetry assumption is still valid: leeward eddies act as part of the bump to the wind passing overhead, rendering the effective bump essentially symmetric. This simple panel method (*Hess,* 1990) serves as an approximation to Laplace's equation and is a common approach to solving simple problems in incompressible and inviscid fluid flow around subsonic aircraft, and we justify its debut in aeolian geology from its successful application in aeronautical engineering. We calculate a parameter $\boldsymbol{\lambda}$ as

$$\lambda = \frac{6\pi \sin(\theta)}{-2\sqrt{3}\sin(\theta)+3\cos(\theta)+3\pi} \quad \text{(Eq. 3)}$$

where θ is the smoothed slope at each adjacent post spacing in our DEM. We then use λ to calculate the wind speedup factor, u_{inc}

$$u_{inc} = 1 + 2\left(\frac{\lambda\cos(\theta)}{\pi} + \frac{\lambda\cos(2\theta)}{\pi\sqrt{3}}\right). \quad \text{(Eq. 4)}$$

We calculated the slope from a downwind-trending topographic profile from a smoothed 1-m post-spacing DEM and used the slope at every DEM post (1 meter spacing) to determine the topographic wind speedup. The wind speed solution to the panel method at every point was then used for the wind speed *U* of equation 1 to calculate estimated flux profiles downwind in three areas of our case study. The speedup factor is only dependent on the slope of the bump, not its physical size, in part because the wind flow is fully turbulent at all length scales (*Kok et al.,* 2012). Typical wind speedup factors of between 1 and 1.15 are common, where a factor of 1 means no speedup. For example, the panel method predicts a wind velocity increase of factor 1.05 for a 2˚ slope. Appropriately, the panel method predicts a wind decrease for negative slopes.

The panel method gives speedup factors notably lower than the values of ~1.5-3 measured in the field (*McKenna-Neumann et al.*, 1997; *Lancaster*, 1985) and also only considers the slope of topography, not its physical size. Justifying our use of it and accepting its lower speedup factors is that *McKenna-Neumann et al*. (1997) measured speedup on steep reversing dunes with slopes up to 14.5˚; 5˚ is a common stoss angle for downwind western Herschel Crater barchan and dome dunes. Furthermore, when we use the panel method's speedup factors in the *Jerolmack et al.* (2012) flux equation, the flux predictions match the data. When we used higher speedup factors the predictions were at least an order of magnitude larger than the flux data.

The IBL flux equation (Equation 1) provides a baseline annual-average flux. In some sense, it assumes the dunes are flat, two-dimensional structures on the ground insofar as there is no topography term in the equation. The flux increase from the streamline compression up the dunes' stoss slopes is therefore superimposed on the baseline flux. As such, the slope speedup does not affect the field scale IBL but only affects local flux deviations from the IBL flux predictions.

2.3. Results

2.3.1. Measured Dune Heights and Fluxes

Measured dune crest fluxes for the three case studies are in Figure 2.5. Dune heights for both Herschel areas are in Figure 2.6.

Numerical values for the following are an average for both Herschel sites but the qualitative concept applies to Nili and elsewhere. Beginning in the upwind margin, the aeolian fields are composed of well-developed, discrete barchan dunes that are on

average ~17-22 m high at their crest with ~5-15 m^3 m^{-1} yr^{-1} of sand flux (Figure 2.5), the same as White Sands (*Jerolmack et al.,* 2012)), with an estimated flux measurement uncertainty of ~10% (Figure A1). Well-exposed bedrock crops out between dunes. Midfield (1-4 km downwind), the dunes overlap, forming barchanoids with well-developed slip faces, and seif dunes. Many barchan horns become elongated, forming incipient seif dunes attached to asymmetric barchans and on the whole, dunes interact via merging, lateral linking, calving, and off-center collisions, thereby evolving the dune field pattern (*Kocurek et al.,* 2010). Still further downwind (6-8 km from the upwind margin), the dunes are again separate and discrete from each other, though they are shorter (~10 m at their crests) than the most upwind dunes, and many are dome dunes which lack slip faces. Measured crest fluxes on the small barchans with slip faces are ~1-3 m^3 m^{-1} yr^{-1}. Furthest downwind (8-11 km), sand sheets cover the bedrock. All dunes are separated from their nearest upwind dune from zero to a few hundred meters with only a slight increase in dune spacing downwind. The morphology transitions cannot be uniquely tied to specific sand flux values and their associated transition distances are even more varied elsewhere.

2.3.2. Model Flux Predictions

Herschel dunes form larger roughness elements than the locally rough bedrock geology (Figure A3). Defining roughness as the standard deviation of the height of an area (*Jerolmack et al.,* 2012), the dunes are several (2-5) times rougher than the upwind bedrock for the western Herschel dune field, which we model as tripping the IBL. The flux data are consistent with a power-law decrease in volumetric sand flux, and this is

also predicted from Equation 1. This is—overall—consistent with the formation of an IBL (Figure 2.5) which predicts a flux decrease with power law slope = -0.3. High-frequency deviations from the IBL flux prediction from local topography likely cause some of the scatter in the flux profile measurements and are of the same magnitude as deviations in the flux measurements. These curves are for different values of *I* based on the ± 0.0015 N m^{-2} (15%) uncertainty in τ_c= 0.01 N m^{-2} (*Ayoub et al.,* 2014). The right-hand panels in Figure 2.5 show topography and slope used to calculate wind speedup effects along ~300-500 m-wide transects down the dune fields, which average topographies width-wise. A given dune may not necessarily lie along the representative topographic transects, thus a one-to-one correspondence between a power law flux deviation (i.e., a slope speedup) and a given crest-flux data point is not expected.

Figure 2.5 (next page). Trends in crest flux (in m^3 m^{-1} Earth-$year^{-1}$) (**a**), elevation, and slope (**b**) as a function of distance downwind from the upwind dune margin for western and eastern Herschel & Nili Patera. (**a**) The gray curves show flux predictions for different values of intermittency corresponding to uncertainty in critical shear stress (given in the text). Lower flux predictions correspond to higher-strength but more rare winds. Pink circles are measured volumetric crest flux measurements per sand dune. The data are enveloped by the range of *a priori* power law flux decay predictions. (**b**) Elevation (height above Mars datum) shown in purple on the left axis and the slope (derivative of elevation) shown in cyan (right axis). Each topographic transect was several hundred pixels wide to average width-wise over topography; it was subsequently smoothed over a few meters length-wise to minimize effects of very short wavelength topography or artifacts in the DEM. We only applied the panel method to adjacent DEM posts and so it is not sensitive to long wavelength topography. Note a strong correspondence between the slope and the slope-induced flux prediction. Panel method predictions of flux increase are of the same magnitude as scatter in the data and are superimposed as perturbations on the IBL flux decay curve.

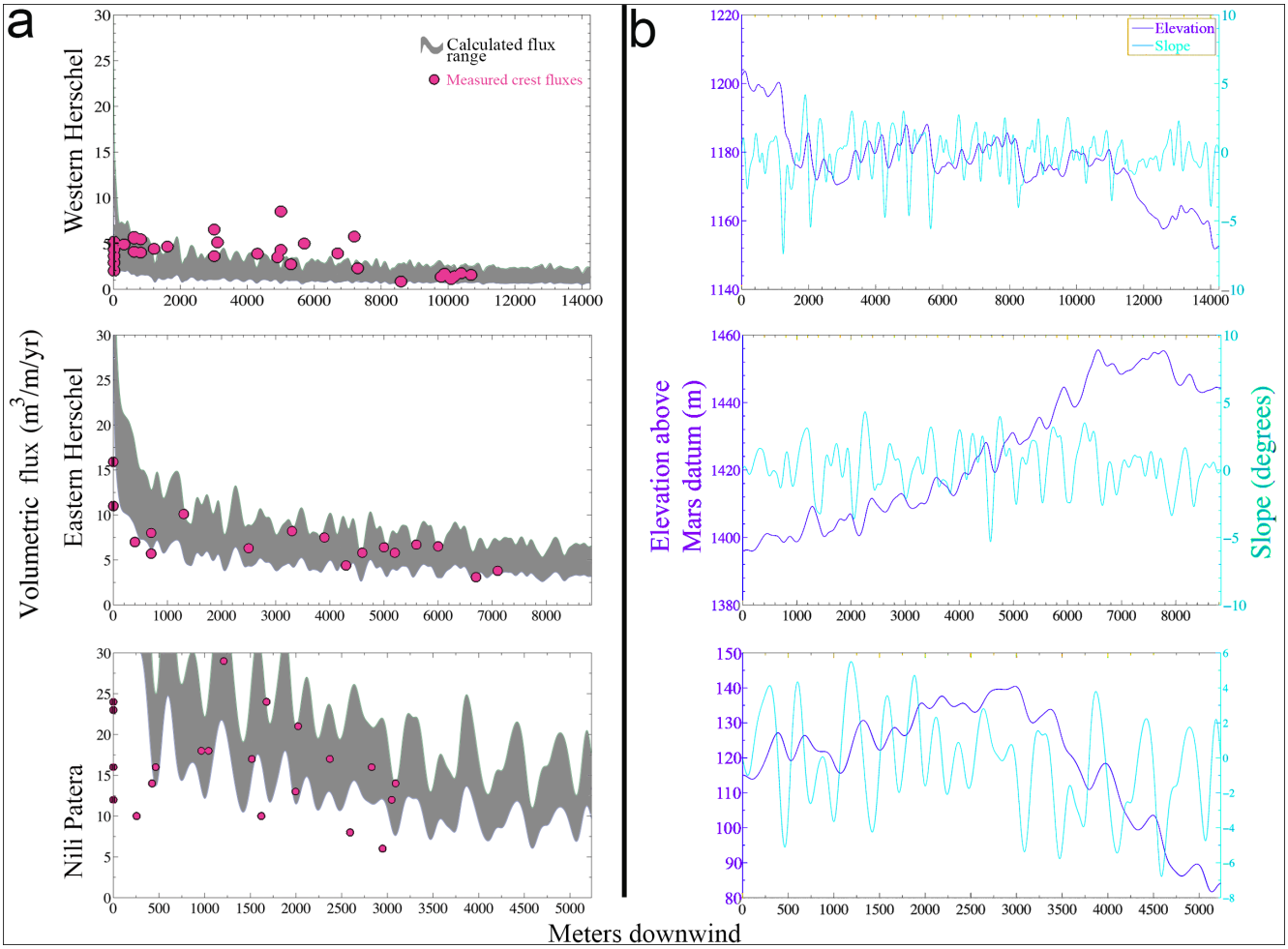
a
b
Western Herschel
Eastern Herschel
Nili Patera
Volumetric flux (m3/m/yr)
Calculated flux range
Measured crest fluxes
Elevation
Slope
Elevation above Mars datum (m)
Slope (degrees)
Meters downwind

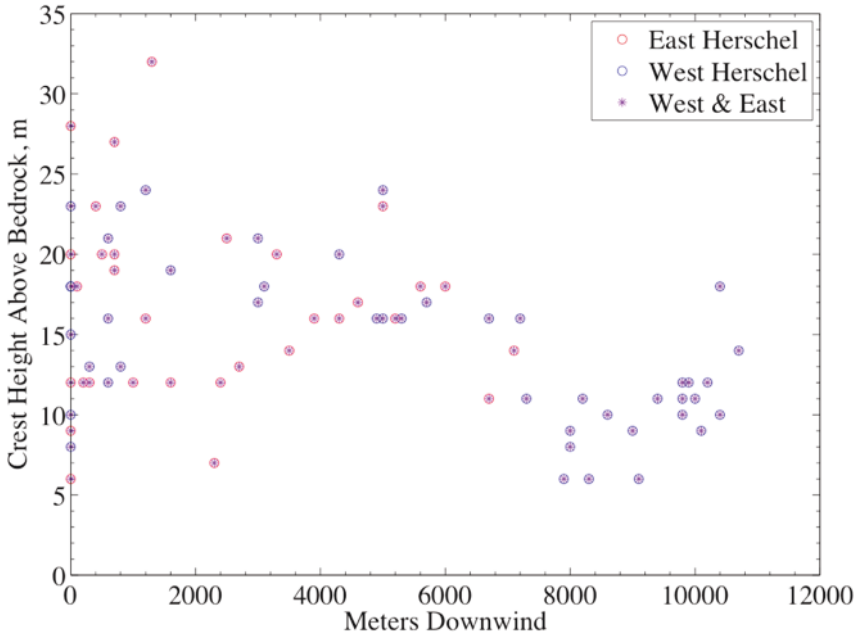

Figure 2.6. Dune heights measured from stereo HiRISE-derived DEMs plotted as a function of distance downwind for both western and eastern Herschel dune fields.

2.4. Discussion

2.4.1. Justification for Invoking IBL Theory

Bolstering the applicability of the Jerolmack flux equation (Equation 1) and thus the IBL interpretation of flux is that the model is agnostic regarding measured flux data and yet fits the overall measured flux values and their decay downwind, both on the Martian case study sites and at Earth's White Sands (*Jerolmack et al.*, 2012). IBLs are not the only way to explain lessening sand flux downwind, however. The decrease in sand flux downwind could be partly attributed to "substrate sequestration" of sand by deposition in interdune areas, which removes sand from the dynamic system. However, this effect is likely very minimal, as we observe the dunes to sit directly on bedrock. They

are not perched on a substrate of sand as is the case with White Sands (*Langford*, 2003 and references therein).

Pelletier's (2015) model may partly apply to the Martian dune field case studies. The principle difference between the *Pelletier* and *Jerolmack et al.* (2012) models is that Pelletier considers a dune field's overall topographic heterogeneity, not just the roughness transition at the upwind margin. However, whereas *Jerolmack et al.* (2012) explicitly mention the discrete roughness change upwind, their flux equation (our Equation 1) considers just the dune field roughness, not the transition from upwind roughness. Like us, *Pelletier* (2015) considers as important the convergence of wind streamlines for enhancing shear stress and sand flux, which is mentioned but not mathematically accounted for by *Jerolmack et al.* (2012). In our study, we account for streamline compression by applying the panel method to topography from both bedrock and bedforms. A component of *Pelletier's* (2015) model that is almost certainly not applicable on present-day Mars is the dryness versus dampness of bedform sands; Mars' active aeolian sands are undoubtedly dry. Our integrated model reasonably accounts for the observed spatial flux changes and combines the IBL-inducing roughness of the dune field (not undermined by *Pelletier's* analysis) and the streamline compressing attributes of *Pelletier* (2015).

2.4.2. Limitations and Uncertainties

Our model ignores the initiation and cessation of saltation. Because wind speed correlates with slope, there are times when the top parts of dunes are actively saltating and the lower reaches are not. This could result in over-prediction of the amount of dune

crest flux because our models assume that threshold friction speeds are met simultaneously for all parts of a stoss slope.

The R^2 fits between flux data points and IBL-only flux predictions are low (0.18, 0.64, and 0.04 for western and eastern Herschel and Nili, respectively). However, this is expected because of scatter from slope speedup, turbulence, and other effects. Another limitation of our model is that it does not account for variations in sand flux azimuth suggested by barchan horn asymmetry (Figure 2.7), some corrugated slip faces, and some incipient seif dunes. However, it is not clear that this makes a major effect on our model: *Lv et al.* (2016) showed that barchan asymmetry alone cannot be used to constrain the direction of a secondary wind. *Parteli et al.* (2014) describes several processes in addition to secondary winds which can cause dune asymmetry: ground slope, bedrock topography, and sediment flux direction, which are likely convolved in our case study sites. Regarding secondary flows which may be present in our study sites, *Parteli et al.* (2014) model that elongated barchan horns can become seif dunes and *Courrech du Pont et al.* (2014) demonstrate the elongating "fingering" of longitudinal and oblique dunes. Dune collisions seem to be prevalent, partly as evidenced from "stacked" slip faces. Our IBL-plus-slope speedup flux model is ideally suited for unidirectional transport azimuths (e.g. winds), yet still seems applicable with azimuthally varying sand transport (e.g. *Courrech du Pont et al.,* 2014), as long as one azimuth dominates, e.g., with a primary-to-secondary transport ratio of ~five (*Courrech du Pont et al.,* 2014). Our model is not applicable when more than one transport direction dominates (e.g., a lower transport ratio) or where the topography is extreme (near the

repose angle) and gravity begins to dominate over wind, e.g., in Valles Marineris (*Chojnacki et al.,* 2014).

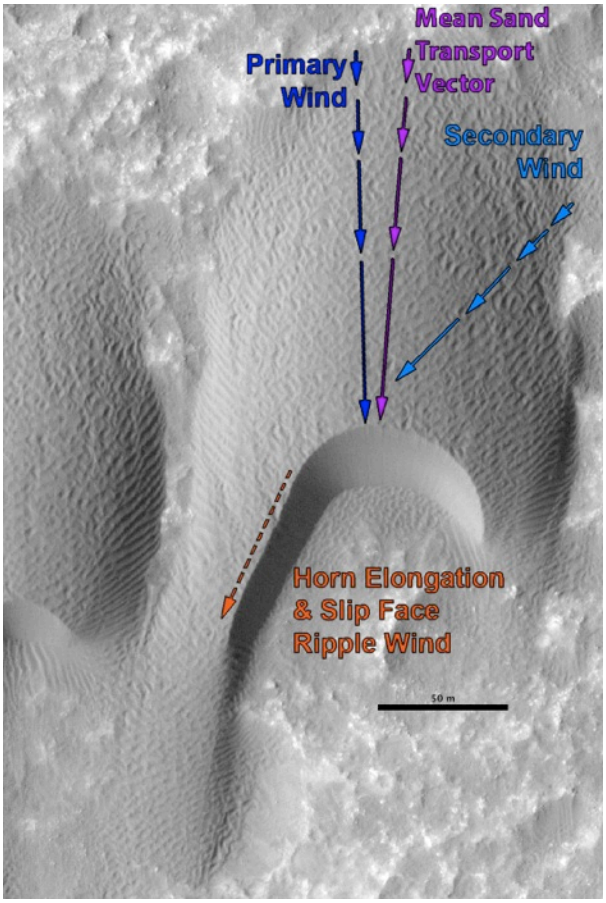

Figure 2.7. A western Herschel asymmetric barchan dune with arrows schematically illustrating primary (left, blue), secondary (right, cyan), and resultant (purple, center) wind directions. The secondary wind can elongate one of the barchan horns (left, orange) and also add corrugated ripples to part of the slip face. The three arrows on the dune's stoss side also schematically illustrate the stoss slope speedup effect via ever-lengthening arrows. HiRISE image PSP_002860_1650; north is up.

The lack of correlation between dune morphology and sand fluxes in different dune fields should not be a problem for our model. More factors besides downwind flux

decreases and upslope flux increases control dune morphology. These other issues may include sand availability, bedrock characteristics, sand transport azimuth, transport ratios (*Courrech du Pont et al*., 2014), and dune collisions (*Kocurek et al.,* 2010) (which in turn depend on the other listed items). The main point of our model remains that IBL theory and slope speedup can explain flux changes downwind in dune fields with similar boundary conditions as Herschel and Nili (i.e., a Herschel-type dune field).

Finally, slope speedup effects from the panel method under-predict wind slope speedup compared with field measurements; however, when we used field-based wind speedup factors of 2-3 (*McKenna Neuman et al.*, 1997), the predicted sand flux values were far above anything we measured from the slip faces. As in the case of *Jerolmack et al.* (2012), we ignored processes such as smaller-scale "nested" boundary layers (e.g. the "equilibrium layer" (*Garratt*, 1990)) (*Frank and Kocurek*, 1996), large and small scale eddies, flow re-attachment, and viscosity. We submit that these complications are implicitly parameterized in IBL theory and panel method slope speedup.

2.5. Implications

2.5.1. Dunes as Geologic Systems on Mars

Our proposed flux model should have widespread applicability where IBL development controls the flow of wind and where other factors, such as topography or sediment supply, do not dominate. Naturally, this model is not applicable to, for instance, falling dunes in Valles Marineris (*Chojnacki et al.,* 2014) or dunes with reversing slip faces, indicative of widely varying wind azimuths. But, for the many barchan dune fields on Mars, Earth, and perhaps Titan and Venus (which await reconnaissance at higher

resolution), the tenants of our model will provide useful and insightful sand flux estimations, especially when temporal image coverage or *in situ* sand volume measurements of a region are lacking.

2.5.2. Martian Aeolian Stratigraphic Record

Understanding current aeolian environments aids interpretation of lithified aeolian sediment, and the ongoing exploration of Mars is providing more instances of aeolian stratigraphy (e.g. *Grotzinger et al.,* 2005; *Milliken et al.,* 2014; *Grotzinger et al.,* 2015; *Lapotre et al.,* 2016). For example, *Lapotre et al.* (2016) demonstrate that new insights into Martian aeolian bedform dynamics can aid in the interpretation of sandstone records of paleo-environments. In their paper, *Lapotre et al.* (2016) re-interpret ripples seen in HiRISE images as subaerial fluid-drag ripples, analogous to subaqueous ripples on Earth, both of which are strongly influenced by the fluids' viscosity. They then identify these ripples preserved in exposed sandstone cliffs at Victoria Crater as imaged from the rover *Opportunity* and interpret the late-Noachian depositional paleo-environment as one with a thin, viscous atmosphere. More related to sand flux, in Gale Crater's sandstone deposits the rover *Curiosity* imaged foreset beds, cross stratification, and truncated erosional surfaces, interpreted as aeolian in origin (*Grotzinger et al.,* 2015). Similarly, *Milliken et al.* (2014) provide evidence that dunes may lithify and remain identifiable in both planform and eroded cross section from orbital imagery. In such cases the slip face and crest orientations remain identifiable, likewise indicating a paleo-aeolian environment in a region that may no longer be dominated by sand flux. Future surface exploration of Mars will undoubtedly discover more lithified aeolian sandstone in outcrop. Where

preserved in the Martian sandstone stratigraphic record, our documented morphologic evolution can be recorded as transitions from dunes with slip faces (preserved as foreset beds) to bedforms lacking slip faces (climbing and falling cross stratification), as well as grain size transitions from coarse to fine downwind (*Jerolmack et al.,* 2011).

With a downwind decaying sand flux for our Martian case studies and the White Sands case study (*Jerolmack et al.,* 2012; *Pelletier,* 2015), one would predict net accumulation due to the ever-weakening downwind flux. Rather, we see sand dunes transition to sand sheets, which thin before disappearing downwind in the case of the Herschel aeolian fields or abutting bedrock in the case of Nili's dune field. Reconciling the disparate prediction and observation is difficult. Perhaps the dune fields are quite young (few 10s kyr) and have not had time to accumulate an immobile sand layer atop the bedrock. To illustrate the potential youth of dune fields, it would take only 40 kyr for an upwind dune moving a typical speed of 0.25 m Earth-year^{-1} to reach the downwind margin 10 km away and given enough time, accumulation of aeolian strata will occur. Or, perhaps the maximum wind shear stress never falls below the fluid threshold and the entire dune and sand sheet field migrates downwind with a constant sand supply and no net accumulation ever occurs. Further research into Martian sediment pathways, bedform dynamics, and climate cycles may elucidate this mystery (e.g. *Chojnacki et al.,* 2014; *Lapotre et al.,* 2016).

2.6. Conclusions

We identify an aeolian dune morphological sequence as a type example on Mars with a downwind decreasing sand flux as consistent with the predictions from internal

boundary layer theory and wind-slope speedup effects. The spatially-evolving sequence (the "Herschel-type dune field") begins upwind with barchan sand dunes and proceeds downwind with barchanoid and seif, dome dunes, and finally, sand sheets, which we find across Mars. We also demonstrate a novel method to quantitatively estimate sand flux intermittency *I* by integrating wind speed histograms from GCMs. Our sand flux measurements and morphological classifications from the Herschel Crater and Nili Patera dune fields are applicable to other sand dune fields on any planetary body exhibiting Herschel-type dune field characteristics. Our model appears to accurately predict flux trends regardless if the *Jerolmack et al.* (2012) or the *Pelletier* (2015) roughness assumptions are made. Thus we offer the IBL-plus-slope speedup integrated model as a convenient semi-empirical model for predicting sand flux within Herschel-type dune fields on Mars, Earth, Venus, and Titan without the need for temporal image coverage.

References

Anderson, W. and M. Chemacki (2014), Numerical study of turbulent flow over complex aeolian dune fields: The White Sands National Monument, Phys. Rev. E, 89, doi:10.1103/PhysRevE.89.013005.

Ayoub, F., et al., (2014), Threshold for sand mobility on Mars calibrated from season variations of sand flux, Nature Comm. 6096, 1-8, doi:10.1038/ncomms6096.

Blasius, H., (1913), Das Aehnlichkeitsgesetz bei Reibungsvorgängen in Flüssigkeiten, Mitteilungen über Forschungsarbeiten auf dem Gebiete des Ingenieurwesens, 131, doi: 10.1007/978-3-662-02239-9_1.

Bourke, M. C., J. E. Bullard, and O. S. Barnouin-Jha (2004), Aeolian sediment transport pathways and aerodynamics at troughs on Mars, J. Geophys. Res., 109, E07005, doi:10.1029/2003JE002155.

Bridges, N.T., et al., (2012), Earth-like sand fluxes on Mars, Nature, v. 485, p. 339, doi:10.1038/nature11022.

Cardinale, M., et al., (2016), Present-day aeolian activity in Herschel Crater, Mars, Icarus, 265, 139-148, doi:10.1016/j.icarus.2015.10.022.

Cardinale, M., G. Komatsu, S. Silvestro, and D. Tirsch (2012), The influence of local topography for wind direction on Mars: two examples of dune fields in crater basins, Earth Surface Processes and Landforms, 37, p. 1437-1443, doi: 10.1002/esp.3289.

Chojnacki, M., D. M. Burr, J. E. Moersch, and J. J. Wray (2014), Valles Marineris dune sediment provenance and pathways, Icarus, 232, p. 187-219, doi:10.1016/j.icarus.2014.01.011.

Christensen, P.R. E. et al., (2009), JMARS – A Planetary GIS, http://adsabs.harvard.edu/abs/2009AGUFMIN22A..06C

Clemmensen, L. B. and K. Abrahamsen (1983), Aeolian stratification and facies association in desert sediments, Arran basin (Permian), Scotland, Sedimentology, 30, 311-339, doi:10.1111/j.1365-3091.1983.tb00676.x.

Courrech du Pont, S., C. Narteau, and X. Gao, (2014) Two modes for dune orientation, Geology, 42, 9, 743-746, doi:10.1130/G35657.1.

Eastwood, E. N. et al., (2012), Methodology for reconstructing wind direction, wind speed and duration of wind events from aeolian cross-strata, JGR, 117, F03035, doi:10.1029/2012JF002368.

Frank, A. J. and G. Kocurek, (1996), Airflow up the stoss slope of sand dunes: limitations of current understanding, Geomorphology, 17, p. 47-54, doi:10.1016/0169-555X(95)00094-L.

Gao, X., C. Narteau, and O. Rozier, (2015) Development and steady state of transverse dunes: A numerical analysis of dune pattern coarsening and giant dunes, JGR Earth Surf., 120, 2200-2219, doi:10.1002/2015JF003549.

Garratt, J. R., (1990), The Internal Boundary Layer – A Review, Boundary-Layer Meteorology, 50: 171-203.

Grotzinger, J. P. et al., (2005), Stratigraphy and sedimentology of a dry to wet eolian depositional system, Burns formation, Meridiani Planum, Mars, EPSL, 240, p. 11-72, doi:10.1016/j.epsl.2005.09.039.

Grotzinger, J.P. et al. (2013), A habitable fluvio-lacustrine environment at Yellowknife Bay, Gale Crater, Mars, Science Express 343, 1242777-1 – 1242777-14, doi:10.1126/science.1242777.

Hayward, R.K., et al. (2007), Mars global digital dune database and initial science results, JGR, 112, E11007, doi:10.1029/2007JE002943.

Hess, J. L., (1990), Panel methods in computational fluid dynamics, Annu. Rev. Fluid Mech., 22, 255-274.

Hunter, R. (1977), Basic types of stratification in small aeolian dunes, Sedimentology, 24, 361-387, doi:10.1111/j.1365-3091.1977.tb00128.x.

Jackson, P. S., and J. C. R. Hunt (1975), Turbulent wind flow over a low hill, Quart. J. R. Met. Soc., 101, p. 929-955, doi:10.1002/qj.49710143015.

Jerolmack, D. J., M. D. Reitz, R. L., Martin (2011), Sorting out abrasion in a gypsum dune field, JGR, 116, F02003, doi:10.1029/2010JF001821.

Jerolmack, D. J., et al., (2012), Internal boundary layer model for the evolution of desert dune fields, Nature Geoscience 5, 206-209, doi:10.1038/ngeo1381.

Kirk, R. L., et al., (2008), Ultrahigh resolution topographic mapping of Mars with MRO HiRISE stereo images: Meter-scale slopes of candidate Phoenix landing sites, JGR Planets, 113, E3, doi: 10.1029/2007JE003000.

Kocurek, G., R. C. Ewing, and D. Mohrig (2010), How do beform patterns arise? New views on the role of bedform interactions within a set of boundary conditions, Earth Surface Processes and Landforms, 35, 51-63, DOI: 10.1002/esp.1913.

Kok, J. F., et al., (2012), The physics of wind-blown sand and dust, Reports Prog. Physics, 75, doi:10.1088/0034-4885/75/10/106901.

Lancaster, N. (1985) Variations in wind velocity and sand transport on the windward flanks of desert sand dunes: Sedimentology, 32, 581-593, DOI: 10.1111/j.1365-3091.1985.tb00472.x.

Langford, R. P., (2003) The Holocene history of the White Sands dune field and influences on eolian deflation and playa lakes: Quaternary International, 104, p. 31-39, doi:10.1016/S1040-6182(02)00133-7.

Lapotre, M. G. A., et al., (2016), Large wind ripples on Mars: A record of atmospheric evolution, Science, 353, 6294, doi:10.1126/science.aaf3206.

Leprince, S., et al., (2007) Automatic and precise orthorectification, coregistration, and subpixel correlation of satellite images, application to ground deformation measurements, IEEE Trans. Geosci. & Remote Sensing, 45, 1529-1558, doi:10.1109/TGRS.2006.888937.

Lettau, H. (1969), Note on aerodynamic roughness-parameter estimation on the basis of roughness-element description, Research & Development Technical Report ECOM 66-G24-F, doi:http://dx.doi.org/10.1175/1520-0450(1969)008<0828:NOARPE>2.0.CO;2.

Lorenz, R. D. and J. R. Zimbelman (2014), Dune Worlds: How Windblown Sand Shapes Planetary Landscapes, Springer.

Lv, P., Z. Dong, C. Narteau, and O. Rozier (2016), Morphodynamic mechanisms for the formation of asymmetric barchans: improvement of the Bagnold and Tsoar models, Environ. Earth Sci., 75, p. 259, doi:10.1007/s12665-015-5083-2.

Malin, M. C., et al., (2007) Context Camera Investigation on board the Mars Reconnaissance Orbiter, JGR Planets, 112, E5, doi:10.1029/2006JE002808.

McEwen, S., et al., (2007) Mars Reconnaissance Orbiter's High Resolution Imagine Science Experiment (HiRISE), JGR, 112, E5, doi:10.1029/2005JE002605.

McKenna Neuman C., N. Lancaster, and W. G. Nickling, (1997), Relations between dune morphology, air flow, and sediment flux on reversing dunes, Silver Peak, Nevada, Sedimentology 44, doi:10.1046/j.1365-3091.1997.d01-61.x.

McLean, S. R., and J. D. Smith (1986), A model for flow over two-dimensional bedforms, J. Hydraul. Eng., 112(4), p. 300-317, doi: 10.1061/(ASCE)0733-9429(1986)112:4(300).

Milliken, R. E., R. C. Ewing, W. W. Fisher, and J. Hurowitz (2014), Wind-blown sandstones cemented by sulfate and clay minerals in Gale Crater, Mars, GRL, 41, 1149-1154, doi:10.1002/2013GL059097.

Momiji, H., R. Carretero-González, S. R. Bishop, and A. Warren (2000), Simulation of the effect of wind speedup in the formation of transverse dune fields, Earth Surf. Proc. and Landforms, 25, p. 905-918.

Palmer, J. A., R. Mejia-Alvarez, J. L. Best, K. T. Christensen (2012), Particle-image velocimetry measurements of flow over interacting barchan dunes, Exp. Fluids 52, p. 809-829, doi:10.1007/s00348-011-1104-4.

Parteli, E. J. R., et al., (2014), Origins of barchan dune asymmetry: Insights from numerical simulations, Aeolian Research 12, p. 121-133, doi:10.1016/j.aeolia.2013.12.002.

Pelletier, J. D., (2009) Controls on the height and spacing of eolian ripples and transverse dunes: A numerical modeling investigation, Geomorphology, 105, doi:10.1016/j.geomorph.2008.10.010.

Pelletier, J. D., (2015) Controls on the large-scale spatial variations of dune field properties in the barchanoid portion of White Sands dune field, New Mexico, JGR: Earth Surface, 120, 453-473, doi:10.1002/2014JF003314.

Rasmussen, K. R. (1989), Some aspects of flow over coastal dunes, Proc. R. Soc. Edin., Section B, 96, p. 129-147, doi: 10.1017/S0269727000010897.

Sagan, C., et al. (1972), Variable features on Mars: Preliminary Mariner 9 television results, Icarus, 17, 346-372, doi:10.1016/0019-1035(72)90005-X.

Savijarvi, H., and A. Maattanen (2010), Boundary-layer simulations for the Mars Phoenix lander site, Q. J. Meteorol. Soc., 136, 1497-1505, DOI:10.1002/qj.650.

Silvestro, S., L. K. Fenton, D. A. Vaz, N. T. Bridges, G. G. Ori (2010), Ripple migration and dune activity on Mars: Evidence for dynamic wind processes, GRL, 37, L20203, doi:10.1029/2010GL044743.

Tanaka, K. L., et al., (2014), Geologic map of Mars, USGS Scientific Investigations Map 3292, scale 1:20,000,000, pamphlet 43 p., http://dx.doi.org/10.3133/sim3292.

Wiggs, G. F. S., I. Livingstone, and A. Warren (1996), The role of streamline curvature in sand dune dynamics: evidence from field and wind tunnel measurements, Geomorphology, 17, doi:10.1016/0169-555X(95)00093-K.

Appendix A

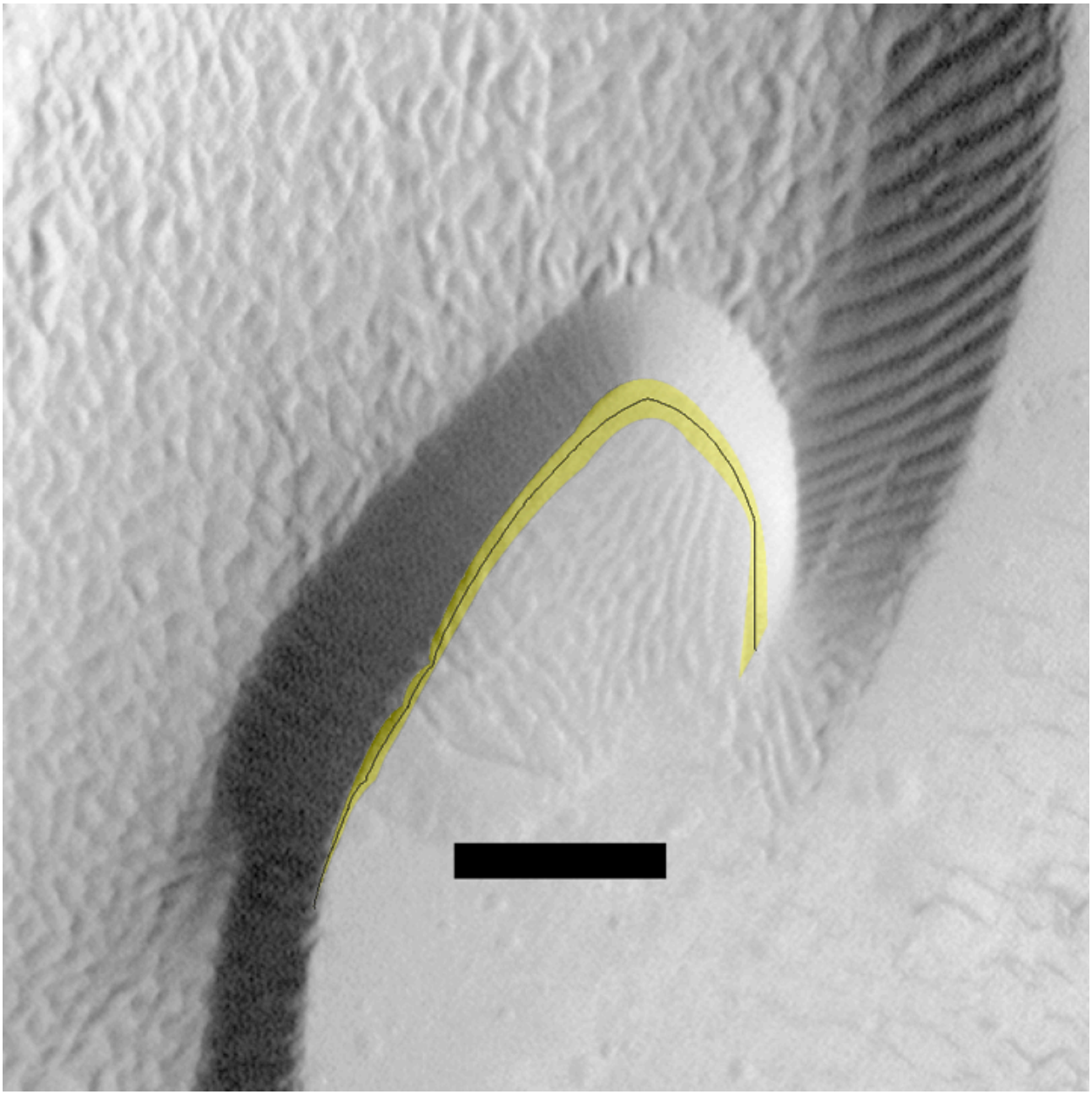

Figure A1. Illustration of measuring the slip face advance on a barchan sand dune. The yellow shaded region is the area covered by the slip face between the two co-registered HiRISE images. The black curve is the length of the active region of the slip face. These two values' ratios reveal the characteristic dune migration distance during the images'

time interval, giving dune speed. Multiplying the speed by the crest height gives the volumetric sand flux at the crest. The estimated uncertainty is 10 pixels in both the overlap area (± 0.6 m^2) and the arc length (± 2.5 m) measurement, and ± 1 m height from the DEM, giving an estimated flux uncertainty of ~10% for similar measurements. The scale bar is 50 m long and north is up. The co-registered HiRISE images are PSP_002728_1645 and ESP_037948_1645.

Study Site: Herschel Crater

Herschel crater (14.4˚S, 130˚E) is a degraded Noachian peak-ring basin almost 300 km in diameter located in the southern highlands (*Tanaka et al.*, 2014; *Cardinale et al*., 2016). It features multiple aeolian landforms: barchan, barchanoid, and dome dune fields; numerous sand sheets; sand ripples; and indurated transverse aeolian ridges (TARs). It thus serves as a natural laboratory for studying dune and ripple migration rates and direction, sediment flux, deposition and erosion rates, sediment sources and sinks, bedform induration, bedform morphology changes, and generally the evolution of a landscape as caused by wind-mobilized sediment over most of Mars' geologic history.

Nili Patera and HiRISE

The Nili Patera dune field has been studied extensively (*Bridges et al.*, 2012; *Ayoub et al.*, 2014) at 25 cm/px resolution from HiRISE's (High Resolution Imaging Science Experiment) orbital altitude and has shown to be quite active and to vary in activity seasonally and annually. We extended the use of HiRISE to monitor several portions of the Herschel Crater dune field.

In the manner of *Bridges et al.* (2012), we used three HiRISE images per location: two images taken close together in time (a few months) allowed digital elevation model (DEM) construction, and one of those images compared against a later orthoimage allowed for tracking dune migration.

Repeat HiRISE coverage at Nili Patera did not extend as far downwind as needed to measure crest fluxes on distal dunes. Thus we can only compare the central and upwind portions of the Nili dune field to the Herschel dune fields.

Mobility Intermittency Estimation

Our numeric atmospheric circulation models allowed us to investigate the fraction of time the wind was above the critical shear stress threshold τ_c. First we integrated under the histogrammed data using Matlab's trapezoid approximation method with the command "trapz" (blue and red data points in Figure S2). Then, we selected the shear stresses at and above threshold and integrated under those data (red in Figure S2). Then we took the ratio of above-threshold to all data (red/(red+blue) data points). In this case, illustrated in Figure S2 for East Herschel, the critical threshold value was $\tau_c = 0.01$ N m^{-2}, and the ratioed integrands are 0.035521/0.38661 = 0.092 ~ 9%. So, sediment should be mobile 9% of the time. Corresponding values of u^*, I, and U for $\tau_c = 0.01$ N m^{-2} are given in Table S2.

IBL Flux Equation Coefficient

Our usage of the 0.055 coefficient, by coincidence, is ten times greater than that used by Jerolmack et al. (2012) (see their Supplementary sections 4-5) and is a

phenomenological friction factor. The coefficient they use of 0.0055 is partly derived from Glauert's (1956) formulation of Blasius' (1913) boundary layer shear stress equation $\tau = 0.0225\rho_{atmo}U^2\left(\frac{\nu}{U\delta}\right)^{1/4}$, where δ is the thickness of the IBL. The numerical coefficient 0.0225 is an empirical value for turbulent water flow through pipes and is valid up to Reynolds numbers $Re \sim 10^5$ (Glauert, 1956). Considering the *Re* at the Martian dune fields using round, representative values (dune height = 20 m, free stream wind speed U = 25 m/s, kinematic viscosity ν = 6.8e-4 m^2/s), we get $Re = \frac{25\times20}{6.8\times10^{-4}} \sim 7.4\times10^5$. As this *Re* is approaching 10^6 and the analogy to water flowing in a pipe breaks down, we feel justified in using a different coefficient in the IBL flux equation for Mars than Jerolmack et al. used for Earth. Indeed, the Martian atmosphere is simultaneously less dense and more viscous than Earth's atmosphere and the sand is basalt (density ~ 2850 kg/m^3) instead of gypsum (density ~ 2360 kg/m^3), which likely justifies a modified coefficient. The specific value of 0.055 fits the data well and correlates to a coefficient value of 0.105 for the Blasius shear stress equation rather than 0.0225. Furthermore, 0.055 is an optimal value for all three case study sites: a higher value would cease to fit Nili Patera's dunes and a lower value would cease to fit western Herschel dunes. Either a higher or lower value would fit eastern Herschel dunes worse. However, the coefficient, we argue, is not so important for establishing IBL theory as controlling flux decay downwind, but rather the overall shape of the curve, which follows a -0.3 power law. A more detailed theoretical or experimental derivation and use of various coefficients as a function of planetary environment and local field conditions awaits further study.

Variable	Value & Units	Description
C	3.88	Friction coefficient for sand at Mars' Reynolds number < 10
D	250 μm	Characteristic grain size, μm
D_0	100 μm	Reference grain size (standard), μm
g	3.7 m/s^2	Mars gravity, m/s^2
u^*_a	Typically ~1.1 m/s	Critical threshold friction speed, m/s (not a physical speed)
U	Typically 24-27 m/s	Free stream air velocity, m/s
x	(Independent Variable)	Distance downwind from the upwind margin, m
h	17 m 22 m 28 m	W Herschel dune heights E Herschel Nili Patera
s	3009 m^2 2167 m^2 3136 m^2	Western Herschel frontal dune area (characteristic cross-sectional area per dune that the wind "sees") Eastern Herschel frontal dune area Nili Patera frontal dune area
n/A	9.5×10^{-6} dunes m^{-2} 1.38×10^{-5} dunes m^{-2} 6.8×10^{-6} dunes m^{-2}	W Herschel spatial dune density E Herschel spatial dune density Nili Patera spatial dune density
ν	6.8831 x 10^{-4} m^2/s	Kinematic viscosity of the atmosphere
H, z	10000 m	Top of atmospheric boundary layer
ρ_{atmo}	0.013-0.015 kg/m^3	Air density
ρ_{solid}	2850 kg/m^3	Density of basaltic sand grains

Table A1. Values used in calculating $<q_s>$ in the main text.

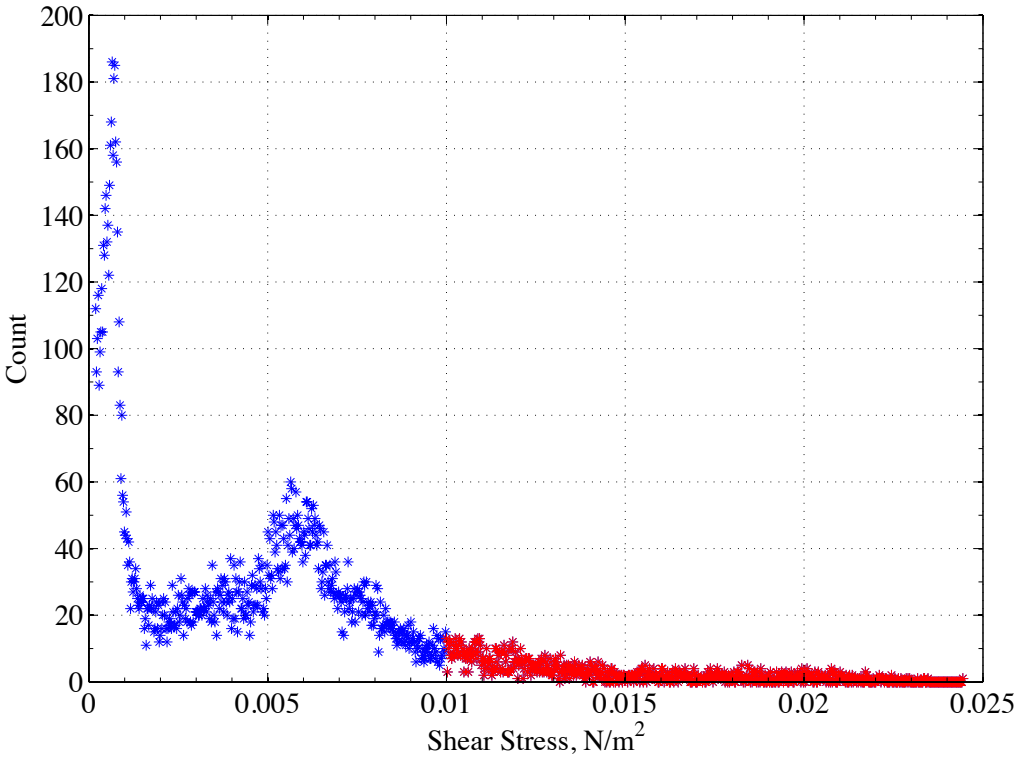

Figure A2. The predicted wind shear stress histogram for Nili Patera from our model. The ratio of the integrands of the above-threshold shear stresses (here, 0.01 N m^{-2}, red) to the total histogram (blue and red points) yields the mobility intermittency value *I*. Here, *I* = 0.09 (Table S2).

	Mean above-critical ρ_{atmo}, kg/m^3 (low, medium, high)	Mean above-critical u^*, m/s (low, medium, high)	I (low, medium, high) (slower wind occurs more frequently)
Nili	0.013777 0.01404 0.014307	0.92638 0.96386 1.002	0.13596 0.091879 0.060707
W. Herschel	0.01496 0.015326 0.015696	1.0205 1.0748 1.1299	0.0033553 0.007725 0.016063
E. Herschel	0.013398 0.013542 0.013687	1.0963 1.1251 1.1539	0.016191 0.025427 0.038209

Table A2. Atmospheric parameters for Nili and Herschel Crater used in calculating U and I using the critical shear stress of 0.01 ± 0.0015 N/m^2 (*Ayoub et al.*, 2014).

Roughness Height Estimation

Several values were needed and many assumptions had to be made to predict the downwind flux decay. The roughness height z_{0L} is controlled by the dunes (*Jerolmack et al*., 2012), and is computed after *Lettau* (1969):

$$z_{0L} = hsn/A$$

where h is a typical dune height, s is the silhouette cross sectional area encountered ("seen") by the oncoming wind, and n/A is the typical number n of roughness elements (dunes) per ground area A. For eastern Herschel Crater, those values are 22 m, 2167 m^2, and 1.38×10^{-5} dunes/m^2, respectively. This yields a roughness height of ~66 cm (0.6579 m). This is notably a different quantity from the Bagnold roughness (*Bagnold*, 1941) which sets the roughness height as 1/30th of a grain diameter, though Bagnold's roughness definition is with regards to flat beds of sand and not transitions from bedrock

to dunes. Notably, *n/A* is an imprecise value and changes within a dune field, for which our model does not account.

All other factors being equal, for a given wind speed, Reynolds numbers are lower on Mars compared to Earth due to the lower atmospheric density, and this serves to increase the drag coefficient to roughly ~3.88 versus ~1 for Earth. Along with the drag coefficient, we present in Table S1 the parameters used in calculating the theoretical sand flux.

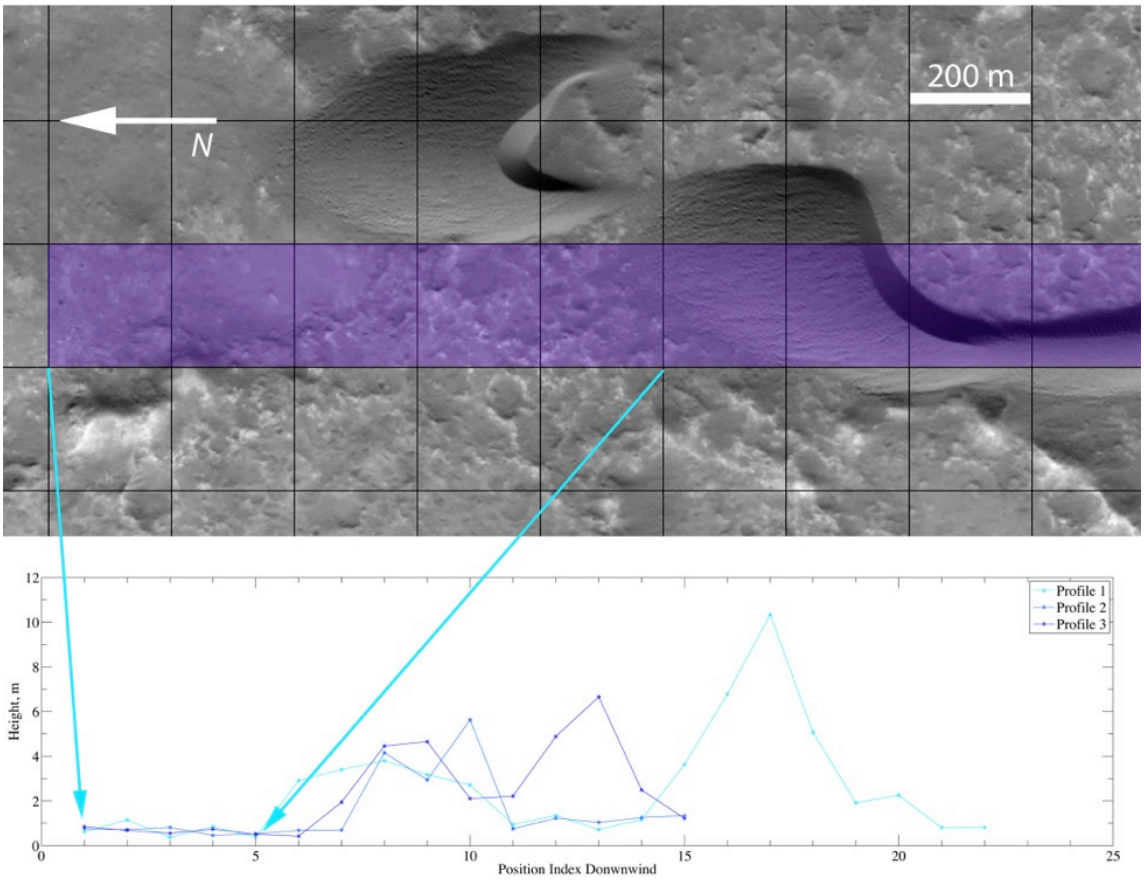

Figure A3. The dunes form a substantial increase in surface roughness compared with the upwind bedrock. We measured the mean and standard deviation of the height in 200 by 200 m squares (grids) along a bedrock-to-dune transect (purple shading). The standard

deviation of the height—plotted in blue shades—is a measure of roughness. We did this for three regions in western Herschel crater, which all show similar roughness trends. An example of upwind bedrock corresponding to Profile 1 is shown with cyan arrows between the image and the plot. Image is 1 m/px orthorectified HiRISE: PSP_002860_1650. Image credit: NASA/University of Arizona/Sarah Sutton.

Western Herschel Horizontal IBL

In Figure A4, we show how the profile of the upwind dune margin (blue trace) qualitatively resembles the profile of a horizontal boundary layer developing over a flat plate and transitioning from laminar flow (thin region) to turbulent flow (thick region). Herschel's peak ring mountain complex (purple trace) may serve as a "plate," creating a boundary layer which controls the location of the dune field. However, no obvious corresponding relationship exists on the eastern side of the peak ring complex.

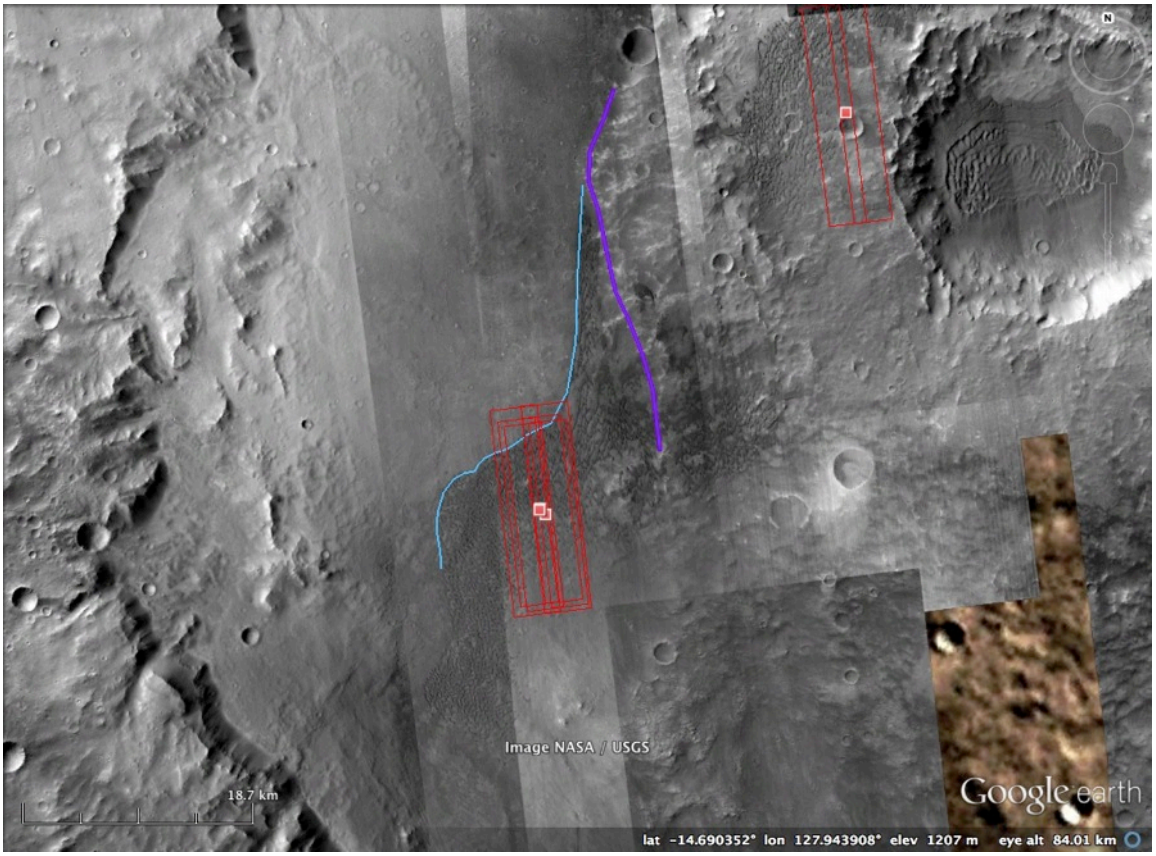

Figure A4. Putative "sideways IBL" highlighted in blue from the peak-ring complex highlighted in purple which possibly may control the shape of the western Herschel dune field margin. The red outlines denote the location of HiRISE "footprints." Context Camera image mosaic from GoogleMars.

Chapter 3: Martian Sand Sheet Characterization and Implications for Formation

Kirby D. Runyon, Nathan T. Bridges, and Claire E. Newman

Abstract

Windblown sand and dust dominate surface geologic processes in Mars' current environment. Besides sand dune fields, areally extensive sand sheets are common across Mars, blanketing the underlying topography with several meters of rippled sand. Earth's sand sheets form upwind or cross-wind to dunes and both partially trap and source sediment to downwind dunes. In contrast, Mars' sheets are located downwind of active barchan and dome sand dunes, suggesting they cannot be a sediment source for the dunes as on Earth. Here, we characterize a Martian sand sheet and its geologic context, model the regional atmospheric circulation, and more broadly consider the implications for sand sheet formation on Mars. Our case study sand sheet in central Herschel Crater is <5 m thick, with an upwind margin forming in the lee of topographic obstacles such as dunes, crater rims, and small hills. The sheet has active migrating superposing ripples with estimated sand fluxes nearly equal to local, regional, and global dunes, some of which have eroded away. A smooth geologic unit interpreted as outcrops of paleo-sand sheets is adjacent to the active sheets. Our observations and atmospheric modeling—which predict wind shear stresses above the sand suspension threshold—indicate that the upwind dunes are being eroded and their sand deposited downwind in sheets in what may be a cyclical process, possibly related to Mars' axial obliquity cycles.

3.1. Introduction

3.1.1. Sand Sheets and Dunes

Sand sheets are aeolian deposits several meters thick that mantle bedrock topography, are areally extensive (e.g. Fryberger et al., 1979; Fryberger et al., 1984; Greeley and Iversen, 1985), and are spatially associated with sand dunes. Both Earth and Mars feature sand sheets—by area, 47% of non-polar aeolian provinces on Mars are sand sheets (Hayward et al., 2006). Comparable global surveys of terrestrial dunes and sand sheets (e.g., Royal Geographical Society, 2010) are not as mature as for Mars, though sheets are still very common on Earth (e.g., Fryberger et al., 1979; Fryberger et al., 1984; Greeley and Iversen, 1985; Kocurek and Nielson, 1986; Kasse, 1997; Maxwell and Haynes, 2001). Because sheets constitute a large fraction of Mars' sediment budget, they naturally raise questions as to their contribution to sand flux and the stratigraphic record.

Several processes collect and concentrate sand, rendering it at least partially immobile and so prevent dune formation and promote sand sheet formation (Kocurek and Nielson, 1986). On Earth, at least five factors immobilize sand and thus control sheet formation (Kocurek and Nielson, 1986): (1) a near-surface water table, (2) surface binding of sand grains, (3) periodic flooding, (4) high proportion of coarse grains, and (5) vegetation. The mobile sub-population may then be free to blow downwind and form dunes. With liquid water and macrovegetation lacking on Mars at least throughout the Amazonian, sand sheets likely form differently between the two planets. Thus, for the last three or more billion years on Mars, only Factors 2 and 4 have likely been relevant. Furthermore, other, uniquely non-terrestrial processes may contribute to Martian sand

sheet production. Possible unique factors contributing to sand sheet development on Mars include different sediment supply levels, low atmospheric density, or lower gravity.

Constraining sheet formation involves understanding their relationship to dunes. Aeolian fields, termed "Herschel-type" after the crater in which they were first described (Runyon et al., 2017), are arrangements of dunes and sand sheets in which the sheets are downwind of the barchan dunes. These are common on Mars (Table S1), yet this arrangement is the reverse of the typical case for terrestrial aeolian fields with nearly unidirectional sand transport direction (e.g. Kocurek and Nielson, 1986; Maxwell and Haynes, 2001; see Table S2). Indeed, on Earth, the sediment supply for dunes commonly comes from upwind or adjacent sand sheets, yet the downwind sand sheets across Herschel Crater and elsewhere clearly cannot be a sand source for these dunes in the present climate. Instead, upwind dunes may be a source for downwind sheets, implying dune erosion.

We test this hypothesis throughout this paper by determining if dune erosion on Mars is possible. This involves measuring sand fluxes on dunes to see if the fluxes are similar to regions where dunes have been seen to totally erode away (Bourke et al., 2008; Chojnacki et al., 2015). Numerical models of wind shear stresses are capable of predicting sand suspension, so a positive prediction for suspension would indicate sand removal from dunes, especially if no clear upwind sand source were feeding the dunes. As will be shown, we have been able to support our hypothesis and it is quite possible that upwind dunes erode into downwind sheets.

3.1.2. Wind and Sand Dynamics

Along with sand sources, wind shear stresses at or above the fluid and impact saltation thresholds affect bedform and sheet migration rates and possibly upwind-to-downwind arrangement. Ayoub et al. (2014) used a combination of global atmospheric modeling and orbital observations of dune migration to estimate the saltation threshold for sand motion in Nili Patera on Mars. The seasonal variation of sand flux inferred from observations was compared with that predicted by the modeled wind field for different wind stress thresholds, with the best match found for a threshold of 0.01 ± 0.0085 Pa. Note that this is the appropriate value for use with output from atmospheric models that do not capture fine scale wind gusts (e.g., the model of Ayoub et al. had a resolution of ~120 km), thus it does not represent the true threshold on the Martian surface, nor the threshold that should be used with output from very high resolution models (such as those with ~10 m grid spacing).

The potential of wind to move sand, as above, is just one metric of aeolian dynamics. Wind intermittency, the fraction of time that wind mobilizes sand, is another useful metric. It can be estimated from integrating histograms of wind speeds or wind shear stresses, either from measurements (Jerolmack et al., 2012) or from atmospheric circulation models (Runyon et al., 2017).

In this work we present a case study of bedforms within three regions of the Noachian-age Herschel Crater (D = 300 km): western, central, and eastern Herschel, defined by imaging coverage. All three sites, together with the Nili Patera site, feature Herschel-type aeolian fields which terminate downwind in sand sheets. The four study areas were chosen for their geologic relevance and for how thoroughly they have been re-

imaged by the HiRISE (High Resolution Imaging Science Experiment) camera orbiting Mars. Wind shear stresses significantly higher than the threshold for saltation may lead to sand suspension, which brings with it the possibility of bedform erosion. We predict shear stresses at our study sites, the frequency of above-threshold winds, and any potential for sand suspension, using output from the Mars Weather Research and Forecasting (MarsWRF; Richardson et al., 2007) atmospheric model described in section 2.2. The model runs at ~4.4 km grid spacing in the study region, meaning that it cannot capture smaller-scale eddies or wind speed-ups caused by local topography. However, it does provide a baseline prediction for sand flux as a function of location, time of sol, and season. Given the relatively low resolution, we apply the Ayoub et al.-derived threshold value of 0.01 Pa.

Sand flux is partitioned between at least three mode of transport: saltation, reptation, and creep (Anderson, 1987). Dunes form from the contribution of all three modes. Classical impact ripples are driven by saltation but form and move via reptation and creep (Anderson, 1987). Mars' ripples that are visible from orbit have an uncertain mode of grain motion, though it is likely different from the grain motions responsible for dunes or classical impact ripples. We define these different modes of grain transport for dunes and large ripples as total and ripple flux, respectively, and their relative flux contributions as the flux partition ratio.

Sand dunes form in the first place from an instability of nonlinear hydrodynamic perturbations of the wind flowing over a small bump (Kok et al., 2012), commonly on a sand sheet. As the wind shear stress increases over a relatively smooth patch of sand sheet, sand grains begin to saltate by rising steeply into the wind, accelerating downwind,

and striking the sand patch at a low angle (Bagnold, 1941). The grain may rebound into another saltation path, launch another grain to take its place, "splash" several grains on small ballistic hops, or some combination or continuum among these options. Once saltation begins, given enough sand, it can continue even if the wind shear stress drops below the initial threshold value due to previously saltated grains mechanically lifting additional surface grains (Bagnold 1941). Given a small pre-existing bump on the sand patch, pressure differentials in the atmosphere promote sand erosion upwind of the bump and deposition on the bump's crest, leading to eventual growth into a sand dune. The sand dune is in dynamic equilibrium and does not change volume if equal amounts of sand are eroded on its upwind stoss slope as are deposited on its downwind lee slope, leading to a downwind-migrating dune. On Earth, the sand supply is commonly from upwind or adjacent sand sheets (e.g., Fryberger et al., 1983; Breed et al., 1987), and the dune can grow or shrink if it is not in equilibrium with the sand supply or wind. Mars' lack of obvious upwind sand sources is a mystery for both dune and sheet formation, which we address here in our case study.

3.1.3. Case Study Location

The portion of sand sheet in the case study is 25 km^2 in area (shaded blue in Figure 3.1, with a close-up in Box 4) and sits downwind of a 1-2 dune-wide string of barchan dunes (location shown in Figure 3.1 with its topography in Figure 3.2). As such, the upwind dunes and downwind sheets represent the end members of the geomorphological sequence identified as a Herschel-type dune field (Runyon et al., 2017). The sheet's upwind margin is sharply defined and jaggedly irregular, with bedrock

topography defining the upwind extent of sand tendrils which widen downwind into the massive sand sheet. The downwind margins are diffuse and poorly defined with the sand thinning, gradually revealing the underlying bedrock.

In Section 2 below, we describe the methods for characterizing the sand sheet's morphology and dynamics. These constraints then inform sheet formation.

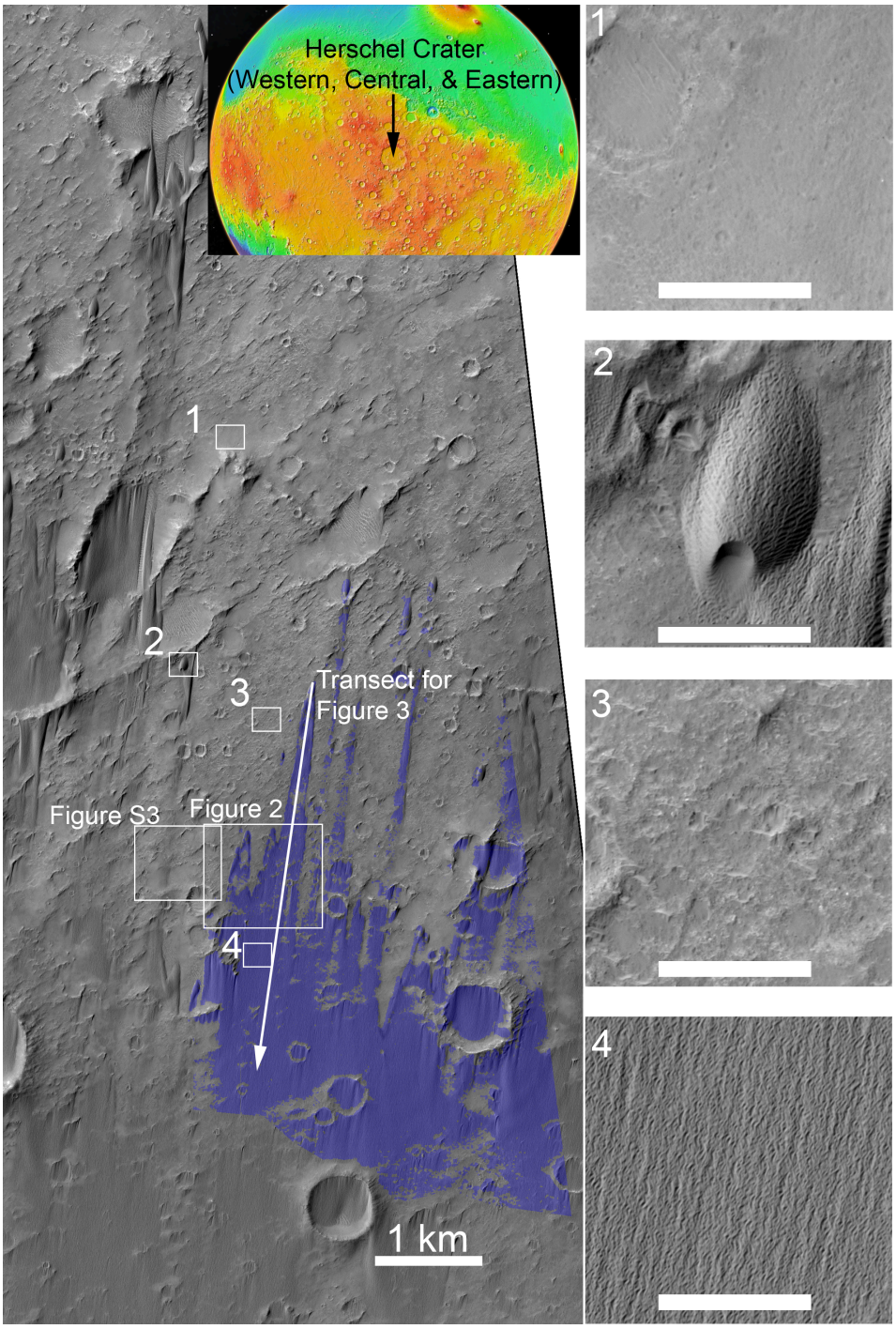

Figure 3.1. The Central Herschel case study sand sheet site is highlighted in blue. Gaps are bare rock. Ripple velocity and sheet thickness measurements are from this area. The four landform types (callout boxes on right) are, from north to south, 1) Smooth unit, 2) sand dunes, 3) bedrock, and 4) sand sheets. Scale bars in insets are 100 m. Inset at top

shows global context of Herschel Crater on a topographic Mars globe from Mars in Google Earth. Portions of HiRISE image ESP_017417_1655 from NASA/University of Arizona.

3.2. Methods

We characterize the sand sheet's morphology and dynamics using orbital images and a numerical wind model. To address the controlling mechanisms of sand sheets on Mars, and why they are common despite boundary conditions very different from those on Earth, we 1) characterize the morphological and dynamical aspects of a Martian sand sheet and the morphology and geologic context of putative remnant paleo-sheets in Herschel Crater (Figure 3.1); 2) model wind shear stresses using a mesoscale atmospheric model; and then 3) use a combination of 1) and 2) to infer the likely evolution of sand sheets and dunes. From their characteristics and atmospheric modeling we 3) suggest Martian sand sheets and dunes form cyclically from erosion of alternately upwind dunes and sheets; and 4) commonly indurate.

3.2.1. Remote Sensing Datasets and Data Products

We choose a section of sand sheet along with local dunes in central Herschel Crater (Figure 3.1) as a case study site with the western and eastern Herschel dunes and sheets providing regional context. Herschel Crater is ideal for several reasons. Nearly the entire southern (downwind) half of the basin is an aeolian province identified as Herschel-type; barchan dunes reveal large-scale winds that are nearly unidirectional throughout; Herschel is well-imaged; and studying Herschel leverages results from

previous work (Cardinale et al., 2016; Runyon et al. 2017). An additional site within the Nili Patera Herschel-type dune field provides a comparison basis and also builds off previous work (Silvestro et al., 2010; Bridges et al. 2012; Ayoub et al., 2014). High resolution (25-30 cm/px) orbital images from the High Resolution Imaging Science Experiment camera (HiRISE (McEwen et al., 2007)) allow for visual interpretation of the sand sheet and its environment. Derived digital terrain models (DTMs) and ripple displacement maps provide quantitative elevation and ripple migration measurement, respectively. DTM creation was done by selecting two HiRISE images (ESP_017417_1655 and ESP_016916_1655 (Table S3)) taken close enough together in time (39 Earth days) such that no ripple displacement was observed, but at different observation angles enabling parallax for computing topography. Creating DTMs of active aeolian settings requires care because ripple displacement can erroneously be attributed to parallax and thus topography.

In addition to characterizing the morphology, we also characterize the aeolian dynamics of the sand sheet's ripples. We estimate total sand flux on the sheet via the ratio of total flux to ripple flux from local dunes. Characterizing bedform dynamics further aids understanding the topographic and boundary layer controls on aeolian field sand flux (Runyon et al., 2017). However, given some ripples' linear patterns, measuring ripple displacement may not measure any along-crest longitudinal movement (Silvestro et al., 2016) of sand and therefore serves as a lower bound for ripple movement.

We measure ripple flux from ripple displacement maps from repeat HiRISE images of the same area that are geographically co-registered to orthoimages with sub-pixel accuracy using the ENVI Classic module Co-Registration of Optically Sensed

Images and Correlation (COSI-Corr) (Leprince et al., 2007) after the manner of Bridges et al. (2012). We use COSI-Corr to produce a ripple displacement map from which we extracted long transects of ripple displacement information. The algorithm COSI-Corr (Leprince et al., 2007) uses tracks patterns of pixels (px) within a moving search window, which we set at 70-by-70 px in size with a step distance of 16 px. The ripple displacement map returned by COSI-Corr has pixel values corresponding to north-south and east-west displacement distances with 4 m/px resolution as a consequence of the step distance and HiRISE's 0.25 m/px resolution. COSI-Corr's algorithm returns null results in locations of very high ripple activity, and we are not able to use these small portions of the image displacement map. When combined with a DTM of the same region, ripple displacement vectors (and hence migration rate, given the known time between change detection images) can be correlated with elevation. To sub-pixel accuracy (average mis-registration of 8×10^{-4} px) we orthorectified a HiRISE image onto the HiRISE DTM of an area and used it and the first image to create the ripple displacement map and to track dune slip face advancements. Image details are in Table S3.

Orthophotos of all HiRISE images for a given location (Table S3) allowed displacement measurements of dune slip faces. With HiRISE datasets, COSI-Corr optimally tracks patterns of ripples but not dune slip face advancements. Manual tracking of slip face displacements—which, when multiplied to the height of the dune crests from the DTM and divided by the time between images gives a measure of dune crest sand flux (units of m^3/m/Earth-year (Eyr))—involved mapping the area covered by the avalanching slip face between subsequent images. We then divided that area by the arc

length of the slip face to arrive at a characteristic rate—and hence crest flux—for that dune.

Measuring total flux on a sand sheet is not as straightforward as measuring dune flux. The boundaries of sand sheets are diffuse, which makes tracking their bulk migration problematical. Instead, we use ripple flux as a proxy for total flux. This requires assuming a characteristic height for the ripples because they are below the DTM's vertical resolution. We assume a triangular ripple profile (Bridges et al., 2012) and use the average (half) height of 15 cm estimated from rover measurements of similar ripples (Lapotre et al., 2016). Multiplying the ripple speed by the half-height yields ripple flux. Measuring both the total flux and ripple flux on dune crests from local dunes gives a ratio for total flux-to-ripple flux. Multiplying this ratio by the ripple flux on the sheets allows for a reasonable estimate of the total sand flux on a sheet and thus the degree of activity on sheets compared with dunes.

3.2.2. Atmospheric Circulation Models

In addition to the circulation models from previous work (Runyon et al., 2017), we also produced a nested mesoscale circulation model for central Herschel Crater. As previously, the resolution is 0.074° (4.4 km at the equator) in a mesoscale domain nested within a global atmospheric model (the MarsWRF GCM; Richardson et al. (2007), Newman et al. (2017)). The model outputs friction speed (u^*) and atmospheric density (ρ) every three Mars hours (1 Mars hour = 1/24th of a Martian day (sol)) for a Mars year. From these values the year-averaged basal wind shear stress $\tau = \rho u^{*2}$ may be calculated. Dunes and the small craters in their midst have a length scale on the order of 100 m;

hence, they are not resolved by a model with 4.4 km grid spacing. Therefore, actual local winds, such as those turbulent eddies shed from dunes (Anderson and Chemacki, 2014; Newman et al., 2017), will have more widely varying magnitudes and directions than our broad, baseline predictions. In addition to wind strength and direction, ratioing the integral of the shear stress histogram from above the threshold shear stress (0.01 Pa) and to the integral of the whole shear stress histogram gives the intermittency for the Herschel and Nili sites.

3.3. Results

3.3.1. Geomorphological Characteristics of the Central Herschel Sand Sheet

The Herschel sand sheet case study area in Figure 3.2 is <5 m thick, with sloping margins of 1-4˚, similar to western Herschel dome dunes, which lack slip faces, and lower than the 4-8˚ for local barchan stoss slopes in central Herschel and also for barchans in Nili Patera (Ayoub et al., 2014). The sheets preferentially fill topographic lows such as craters and occupy areas in the lee of positive topography such as crater rims, knobs, and dunes. Long, thin sand tendrils form in the lee of topography, composing sheet-bounding margins close to 5 m thick. The DTM reveals that elevation contours only weakly correlate with the sheet's margins and thus the sand sheet subtly mimics the underlying bedrock topography.

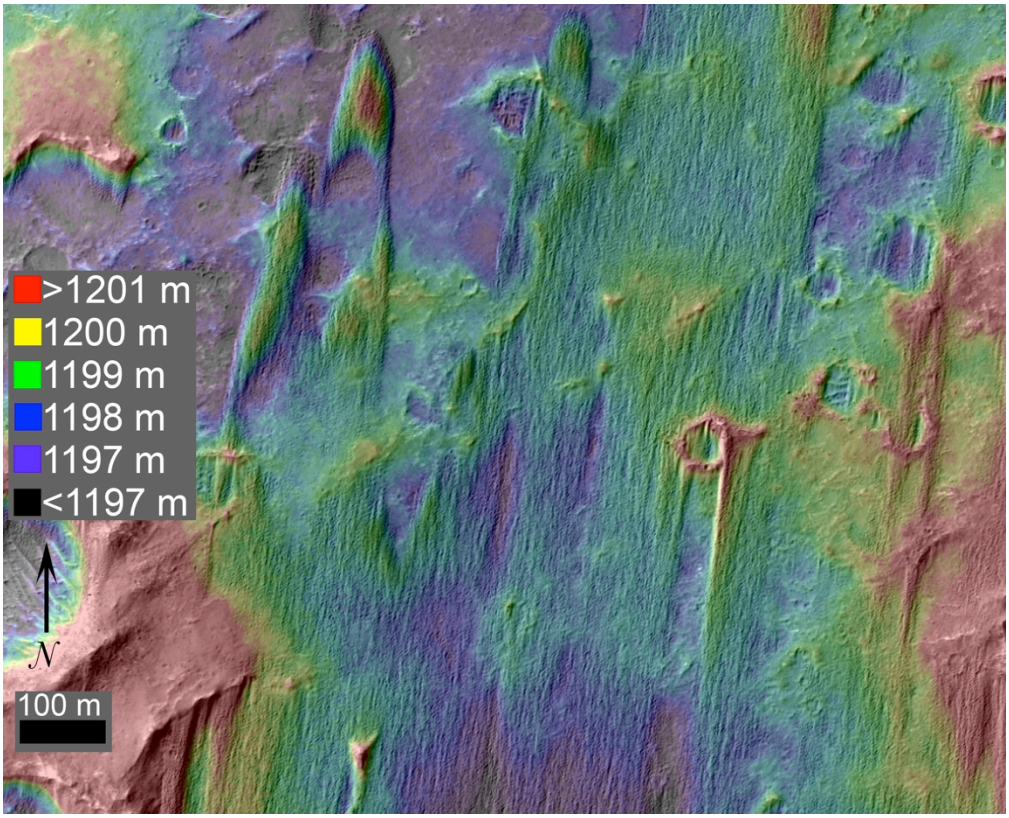

Figure 3.2. HiRISE DTM elevation (color) overlaid on a HiRISE image (gray scale) of the primary sand sheet case study site in central Herschel Crater. The elevation only weakly correlates with the presence of the sand sheet, with the most pronounced correlation in the lee of topographic obstacles. The visible elevation range is only ~4 m. From edge thickness measurements in a stereo-derived DTM, the edges are <5 m thick with low slopes of 1-4°. Image is HiRISE ESP_017417_1655 and color coded with elevation information is from HiRISE DTM DTEEC_017417_1655_016916_1655_A01. Image and DTM credit: NASA/JPL/University of Arizona.

3.3.1.1. Geologic Landforms in Central Herschel

An example of each of the four major geologic landform is shown in Figure 3.1. Both dunes and sand sheets feature superposing ripples. The dunes and sheets are darker

than the surrounding terrain and commonly form their upwind margins in the lee of bedrock topography.

Bare bedrock is characterized as a light-toned, rough unit. It is heavily cratered with degraded 10-100 m-scale craters. Knobs and small hills create wind shelters which may trap sand in their lees.

There are smooth, darker, and nearly featureless outcrops within and around small (few 100 m diameter) craters in Herschel (Figures 3.1, B1). They form a distinct geologic unit and embay rougher and brighter terrain. Some are overprinted with transverse aeolian ridges (TARs), which are immobile across Mars (Geissler et al., 2013). Common clusters of much smaller craters (10 m scale diameter) are present on some of these smooth outcrops. Other Smooth Unit outcrops have rippled, mobile sand in "microsheets" overprinting them.

The meter-scale ripples superposing the dunes and sand sheets have a similar morphological pattern and wavelength (Figures B2, B3) as the "large Martian ripples" described and measured on Gale Crater dunes from the ground and from Mars orbit (Lapotre et al., 2016; Silvestro et al., 2016). We have been using the term "ripple" throughout this paper for brevity when referring to large Martian ripples as distinct from smaller impact ripples, which are not resolved in HiRISE images. While large ripples across Mars have wavelengths of 2-3 m, slight variations exist in Gale Crater ripple wavelength measurements of 1.9 ± 0.2 m (Silvestro et al., 2016) and 2.1 ± 0.6 m (Lapotre et al., 2016). From 11 globally-distributed sites on Mars, ripples are larger and have a broader range of wavelengths of 2.9 ± 0.7 m (Lapotre et al., 2016), which is close to the wavelengths in Herschel of 3.0 ± 0.5 m. Transverse, longitudinal, "box" (Silvestro et al.,

2016) and "braided" ripples occur across both Gale and Herschel craters. Ripples' heights are estimated at 0.3 m based on ground measurements (Lapotre et al., 2016). Given the similar length scale and geomorphology in plan view (Figure B2, B3) to those in Gale, we presume the Herschel ripples' heights are also similar to those in Gale. The formation mechanism of Martian dune ripples is not known conclusively. However, these ripples are larger than impact-splash or reptation ripples found on Earth (Anderson, 1987; Lapotre et al., 2016; Silvestro et al., 2016), suggesting a different formation mechanism. The mechanism may be related to the Martian atmosphere's higher kinematic viscosity relative to Earth leading to "fluid-drag" ripples, perhaps analogous to subaqueous ripples on Earth (Lapotre et al., 2016). The similar ripple morphologies found across Mars (Lapotre et al., 2016; Figure B2) lead us to assume that Herschel ripples are the same type of bedforms with similar formation mechanisms.

3.3.2. Aeolian Dynamics

3.3.2.1. Bulk Ripple Movement: Figure B4 (Supplementary Information) shows a Gaussian distribution for ripple migration rates across the primary sand sheet case study site in central Herschel. The average ripple speed of 1.25 ± 0.36 m/Eyr (Eyr = Earth year) which, although faster than typical dune speeds of 0.2-0.5 m/Eyr, are similar to ripple speeds in Gale Crater (Silvestro et al., 2016). The ripple speeds correspond to a ripple flux of 0.19 ± 0.05 m^3/m/Eyr along the sheet. The average azimuth of ripple migration is toward the SSW at an azimuth of 196° ± 9° (one standard deviation), which is consistent with the overall orientation of the regional dunes and sand tendrils.

3.3.2.2. Downwind-Trending Profiles: Combining the COSI-Corr ripple displacement maps with the DTM revealed associations between ripple migration rates and the underlying topography (the ripples themselves are at or below the 1 m/px resolution of the DTM). Ripple speeds generally decrease further downwind with speeds from just under 2 m/Eyr to a few decimeters/Eyr (Figure 3.3). The downwind decrease in speed is the same trend observed for slip-faced barchan dunes elsewhere on Mars (Bridges et al., 2012; Runyon et al., 2017) and Earth as consistent with boundary layer-controlled flow (Jerolmack et al., 2012). On short spatial scales of 10s-100s m we observer ripple speedups that correlate with bedform and bedrock topography, consistent with the observations of ripple speed increases up barchan dune stoss slopes (Bridges et al., 2012; Runyon et al., 2017).

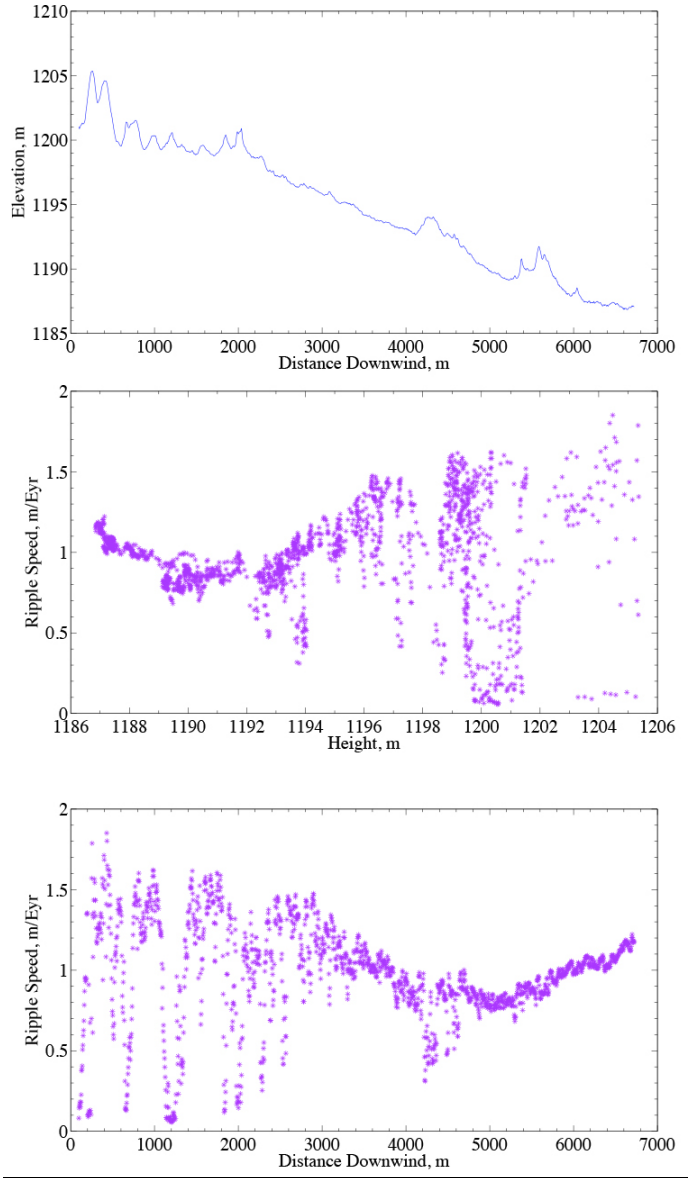

Figure 3.3. Ripple and topography profiles from a ~7 km-long transect on a sand sheet, shown in Figure 3.1. *Top:* Topography generally decreases downwind (to the right) except for short wavelength hills in the distal reaches which may account for the downwind "tail" in the bottom plot. (Central Herschel ROI 5.) *Middle:* Ripple speed generally increases with height (correlation coefficient = ~0.7) except for small wavelength topographic highs interrupting a long wavelength downhill trend. *Bottom:* Ripple speed generally decreases with downwind distance (correlation coefficient ~ 0.8,

not including small areas of bedrock) along the sand sheet except at the distal "tail" where topography seems to control ripple and wind speed.

3.3.2.3. Cross-wind Profiles: Similarly, we extracted ripple displacement and topographic profiles perpendicular to the sand transport direction (i.e., perpendicular to the dominant wind direction) in order to isolate the effects of topography and downwind distance. Calculating the correlation coefficient for the plot of ripple speed versus height gave a low value of 0.2 (for ROI #8) and -0.4 (ROI #9). This low correlation between height and speed is not surprising because nearly all interaction between adjacent sand patches is from upwind to downwind such that adjacent topography in the cross-wind direction is largely irrelevant. The main exception to that, however, is that adjacent cross-wind topography may laterally channelize the wind flow, leading to a local wind and ripple speedup in some locations. Figure 3.3 illustrates such a correlation between the downwind "tail" in the ripple speed data and local topographic highs. This also suggests that short wavelength dominates over long wavelength topography in controlling wind and ripple speed, which is also consistent with our prior assumptions (Runyon et al., 2017).

3.3.2.4. Total, Ripple, and Ratio-ed Fluxes: The plots in Figure 3.4 report various aeolian dynamic metrics related to ripple and total flux, flux ratios, and above-threshold intermittency necessary to estimate total flux when only ripple rates are measureable. Figure 3.4a plots the average upwind dune crest fluxes as measured from slip face advancement and dune crest height. Fluxes are similar to each other across the three Herschel sites while Nili fluxes are much higher. We also plot the ripple-only flux on both dune crests and sheets in Figure 3.4b. Notably, Central Herschel has the most areally

extensive sand sheets and features a significantly higher ripple flux than the other Herschel sites. For each of the four study sites, we divided the dune crest flux averaged over several local dunes (4c, maroon bars) to the ripple flux at the dunes' crests (4b, maroon bars), which is nearly always the maximum ripple speed on a given dune. We derive the ripple flux at the top of dunes (4b, gold bars) by multiplying the average per-ripple half-height of 15 cm by the ripple speed to yield volumetric flux after the manner of Bridges et al., (2012). We take the ratio of total flux to ripple fluxes, plotted in d). From Figure 3.4d's flux partition ratios, we estimate the total flux on the sand sheets, which are the gold-colored bars in Figure 3.4c. Multiplying these locally-derived flux partition ratios by the ripple flux on sand sheets (Figure 3.4d), we compared the total flux measured on the downwind dunes and the total flux estimated for the sand sheets (Figure 3.4c, gold bars). We note a very broad range in measured flux ratios, suggesting that nearby dunes with slip faces are necessary to establish the appropriate ratio in order to accurately estimate total flux on sand sheets. In other words, there is no single ratio that can be used across Martian aeolian fields to estimate total flux from ripple flux.

The temporal characteristics of aeolian dynamics is arguably as important as the spatial characteristics. Accordingly, following the convention of Runyon et al. (2017), we calculated and plotted the wind intermittency in Figure 3.4e for central Herschel based on results from our nested mesoscale atmospheric circulation models (Figure 3.4f) along with values from the other case study sites (Runyon et al., 2017) and White Sands, NM (Jerolmack et al., 2012) for comparison.

The central Herschel sand sheet has a higher total estimated flux than the local dunes and higher ripple mobility than western or eastern Herschel. However, Nili Patera

dunes are more mobile (Bridges et al., 2012) than any bedforms in Herschel. (The repeat stereo HiRISE images needed to quantify the Nili sand sheet ripple flux have been requested at the time of this writing.)

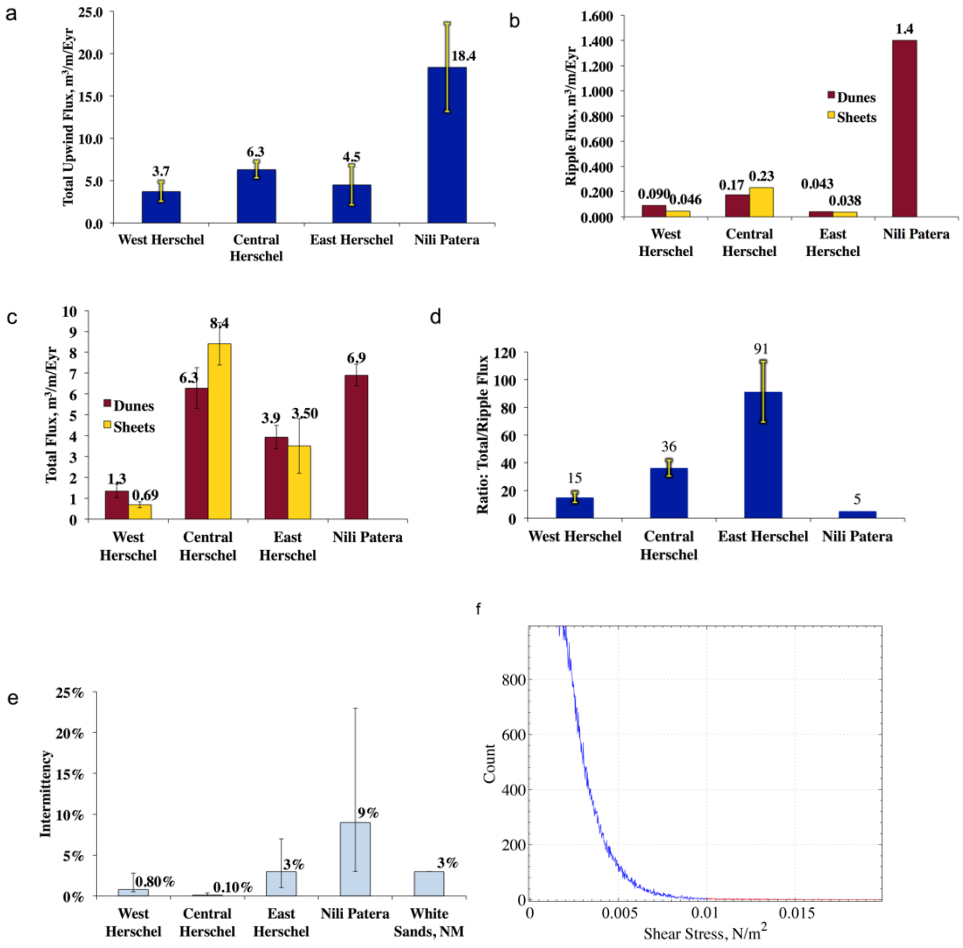

Figure 3.4. a. Average *upwind* total fluxes measured for the most-upwind dunes at each site. Nili data from Bridges et al. (2012). **b.** Ripple-only flux measurements (speed × 0.15 m) from the average of maximum fluxes across dunes or sheets for each study site. Standard deviations are less than 0.05 m^3/m/Eyr and not plotted as error bars. **c.** Multi-dune averaged total fluxes for dunes are shown in maroon and average estimated fluxes from locally-derived flux partition ratios for sheets shown in gold. Estimating total flux from ripple flux is considered in the text. Error bars are 1 standard deviation for each population. **d.** Flux partition ratio from dividing the total flux measured on slip faced-dunes to the maximum ripple flux from the crest of the given dune. Given the paucity of dunes in central Herschel we used the three available upwind dunes rather than more

local dunes. The numerical values in the figure are the average values and are not associated with the error bars. Data from Nili Patera taken from Bridges et al., (2012). **e.** Annual-average intermittency for central Herschel crater is 0.1%, which is anomalously low compared with the other study sites, which show correspondence between intermittency and flux. The error bars represent the uncertainty in intermittency due to the ± 0.0015 Pa uncertainty in threshold wind shear stress (Ayoub et al., 2014). **f.** Wind shear stress histogram for central Herschel Crater in which the values above threshold (> 0.01 Pa) are highlighted in red, as taken from our nested mesoscale atmospheric model. As for the other sites, we calculated the intermittency of 0.1% for Central Herschel in (e) by taking the ratio of the integral above threshold (red) to the integral of the whole plot (blue and red). The histogram uses 1000 bins.

3.4. Discussion

3.4.1. Arrangement and Deflation: Sand Sheets from Upwind Dune Erosion

Our hypothesis of upwind dune erosion via sand suspension into downwind sheets on Mars is consistent with the unusual spatial arrangement of Herschel-type aeolian fields in which sand sheets occur downwind of dunes, rather than upwind. Here, we consider the evidence for dune erosion and sheet accumulation. On Earth, sand sheets overwhelmingly occur upwind or laterally adjacent to dunes. Several examples include sheets in Saudi Arabia (Fryberger et al., 1983; Fryberger et al., 1984), White Sands (which actually has an upwind playa with loose sand; McKee, 1966), and the Selima Sand Sheet in northwest Sudan and southwest Egypt (Breed et al., 1987). Searches in Google Earth (Table S2) and the mentioned literature reveal that this sheet-dune

relationship exists across Earth in regions with fairly unidirectional wind regimes. In terrestrial sheet-dune fields, the upwind sheets serve as a sand source for the dunes; this relationship cannot be the case when the sheets are downwind of the dunes, in contrast to Herschel Crater and across Mars (Table S1).

Bolstering the hypothesis of dune erosion is the precedence of confirmed dune erosion and thus non-equilibrium aeolian processes on modern Mars. North polar Martian dunes have been observed to shrink and then disappear as observed in Mars Orbiter Camera (MOC) images over a period of under six Earth years (Bourke et al., 2008). The dunes which eroded away were small (several decameters in length and width) and no downwind sand sheets were present. These north polar dunes had fluxes comparable to those in Herschel Crater of 1.4-3.1 m^3/m/Eyr (calculated from data in Bourke et al. (2008)), demonstrating that these sand flux values can correlate with—though not necessarily demand—dune erosion. Dunes in Endeavour Crater, Mars, also show net erosion (Chojnacki et al., 2015). Joint observations between HiRISE, MOC, and the Mars Exploration Rover *Opportunity* show deflation of small dome dunes (Chojnacki et al., 2015). In addition to dune erosion, downwind bedrock darkening occurred, indicating sand deposition. The low sand volumes from the small dome dunes apparently did not permit sheet formation in this case. Sand fluxes in Endeavour Crater (2-13 m^3 m^{-1} Eyr^{-1}; Chojnacki et al., 2015) are comparable to those in Herschel Crater (1-16 m^3 m^{-1} Earth-yr^{-1}; this study; Runyon et al., 2017b), indicating that upwind erosion and downwind deposition could occur at the measured fluxes.

It is notable that both the sheets and the dunes have comparable fluxes. From the estimated shear stresses, the dunes' flux is likely partitioned between suspension and

saltation such that the dunes are out of equilibrium and erode. The suspended load of dune-eroded sand eventually settles on the sheets but enters into saltation.

3.4.2. Indications of Cyclic Aeolian Activity

If Mars' upwind dunes are in non-equilibrium and erode into sand sheets, it may be a transient phenomenon controlled by changing environmental boundary conditions. Milankovich cyclicity, especially from Mars' chaotic spin state, strongly control Martian climate (Haberle et al., 2003; Laskar et al., 2004), and could have produced different aeolian regimes in the past. Past epochs of sand sheet formation, immobilization, and induration may have occurred as evidenced by the Smooth Unit (Figures 3.1 and B1). The observations of the Smooth Unit presented in Section 3.1.1 suggest it represents indurated paleo-sand sheets with eroded (planed-off) ripples as shown schematically in Figure 3.5. If Smooth Unit outcrops are paleosheets, their presence points to past, perhaps cyclic, epochs of sheet formation and induration.

One possible mechanism for induration and preservation of aeolian bedforms is by ice burial (Kocurek and Ewing, 2012) followed by diagenesis, e.g., dissolution, recrystallization, and cementation. Dust infiltration between sand grains can facilitate immobilization of sand sheets and dunes (Bridges et al., 2010), thus allowing slow diagenetic processes to operate. This represents a process that has likely occurred over most of Mars throughout its history. Because Martian obliquity changes can alter the climate on timespans of a few kyr (Laskar et al., 2004), equatorial ice (Head et al., 2003) could immobilize and lithify sand cyclically. Throughout different obliquities, monolayers of water adsorbed onto grains can diffusively mobilize S, Cl, and other

cementing salts (Clark, 1982; Jakosky and Christensen, 1986; Bridges et al., 2010). Thus, diagenesis may operate on aeolian sands throughout Martian Milankovich cycles but only successfully cement and lithify sands during periods of low aeolian activity, which likely correlate with low obliquity and thus low shear stresses (Haberle et al., 2003) but also very high obliquities with low-latitude ice. Once-mobile sand sheets may now be exposed as the identified Smooth Unit. This hypothesized aeolian cycle is shown schematically in Figure 3.6.

3.4.3. Mars versus Earth

These observed dune, sheet, and Smooth Unit arrangements together with measured and estimated fluxes raise further questions. 1) How is it that upwind sand sheets are absent or uncommon on Mars whereas they are common on Earth? 2) How is it that downwind sand sheets are absent or uncommon on Earth whereas they are common on Mars?

To address Question 1, we posit that sheets do not form upwind of dunes on Mars due to the lack of sand entrapment via the non-existence of liquid water, vegetation, and overlying coarse pebbles. However, in past environmental Martian epochs, any existing upwind sheets may have been reworked into dunes, as is common on Earth. However, if the aeolian system were cut off from an upwind sand source (such as from the depletion of that source), the last of the sheet would be reworked into dunes and the aeolian system would migrate downwind. As the environmental boundary conditions changed and winds rose above the suspension threshold, upwind dunes could erode into downwind sheets. Thus over multiple environmental epochs we hypothesize that dunes and sheets may

"leapfrog" each other, alternately serving as sand sources and sinks and the entire aeolian system would migrate downwind as it recycles its own sand. This would explain the vast expanse of bare bedrock upwind of the Herschel and Nili dunes and sheets. While the precise details of this hypothesis require further testing, the overall recycling of sand in a downwind-migrating aeolian field that has been at least partially cut off from an upwind source appears quite plausible.

Addressing Question 2, we posit that, on Earth, as weakening downwind shear stresses reduce sand flux, vegetation takes hold and stabilizes local parcels of sand. However, rather than forming a sheet, the lack of coarse pebbles allows saltation to continue, leading to vegetation-stabilized dunes such as the parabolic dunes at White Sands (Jerolmack et al., 2012). On Mars, dunes are almost always perched directly on bedrock, not on sand sheets, pointing to a minimal to non-existent role for vertical accumulation, unlike the situation for Earth. Remote sensing surveys in Google Earth show that sheets may also form laterally on the periphery of dune corridors, as in the western Sahara in Mauritania and the eastern Sahara in Egypt (Figure B5). This is consistent with many dunes sitting atop sand sheets in, e.g., the eastern Sahara Selima Sand Sheet (Breed et al., 1987). Finally, Earth's varied water-rich environments cause many aeolian fields to terminate by immobilizing sand at downwind bodies of water or from high ground water tables, as shown schematically schematized in Figure 3.5.

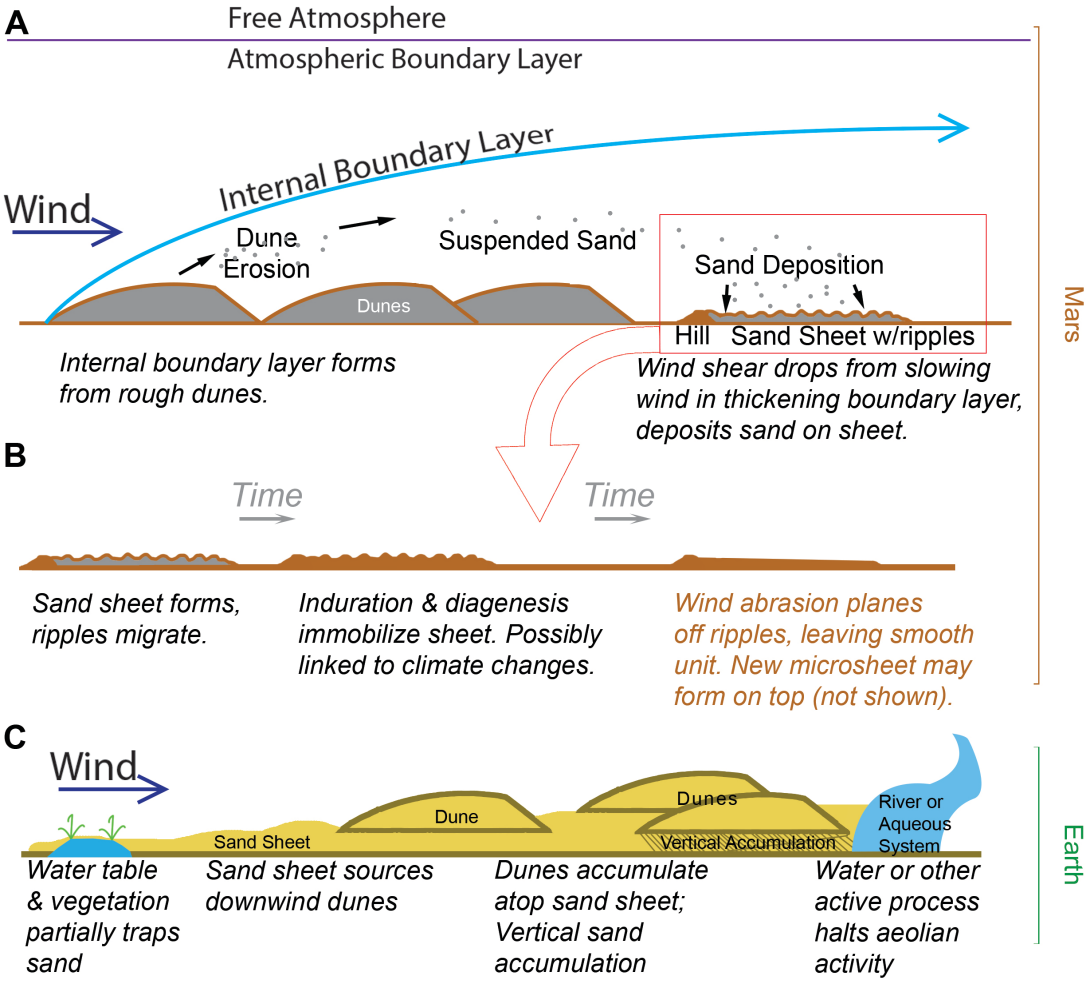

Figure 3.5. Cartoon of our hypothesized model of dune erosion, sand sheet accumulation, and sheet induration. A) From our GCM and likely unresolved eddies, the wind shear stress is occasionally strong enough to suspend sand and thus erode the upwind dunes. As the wind shear decreases downwind in the thickening boundary layer (Runyon et al., 2017), the sand falls out, promoting the formation of the sheet. B) Over time, non-aeolian (e.g., water, salt cementation (Clark, 1982; Jakosky and Christensen, 1986)) and aeolian (dust infiltration) processes indurate the sand sheet, and continued aeolian abrasion planes off the ripples. New sand sheets may form on top of the Smooth Unit. C) On Earth, vegetation and water can partially trap sand, allowing it to slowly source downwind dunes which are often perched on the sand sheet. Bedrock, water, or other

active processes commonly terminates the downwind extent of the aeolian system. This may allow vertical accumulation of sand.

3.4.4. Hypothesis Bolstering: Atmospheric Controls on Flux and Sand Sheet Formation

Sand can only move as often as the wind is above the threshold shear stress, so a clear control on sand flux is the intermittency (e.g. Jerolmack et al., 2012; Runyon et al., 2017), that is, what fraction of the time the wind is at or above threshold. Calculations of intermittency from MarsWRF (Figure 3.4) show that, except for central Herschel, intermittency and sand flux measurements from time series HiRISE images correlate. Central Herschel has the highest measured fluxes for our case study areas but the lowest intermittency. This exception could indicate that MarsWRF fails to accurately predict accurate shear stresses in this area. Or, if the predictions are correct, then these results could indicate that exceptionally rare winds are far enough above threshold to mobilize large amounts of sand in short times and thus make up the difference. Normally, it seems, greater intermittency values can lead to higher annual fluxes due to a longer amount of time for sand to move. However, on Earth, it has been shown (Nishimura and Hunt, 2000; Jerolmack et al., 2011) that if the shear stress is greater than 2.25 times the critical threshold shear stress, net erosion will occur due to sand entering suspension as opposed to saltation. This suspension is hypothesized to be the result of aerodynamic lift forces and upward eddies at sufficiently high shear stresses, as discovered in wind tunnel studies (Nishimura and Hunt, 2000). If this hypothesis is correct and can be applied to Mars, a threshold shear stress of 0.01 ± 0.0015 Pa (Ayoub et al., 2014) implies a calculated suspension shear stresses of 0.019-0.042 Pa. Rare, powerful eddies associated with lower

average shear stresses could still suspend sand even if these average shear stresses aren't quite reached or if the suspension threshold hypothesis is incorrect for Mars. Our atmospheric model predicts maximum shear stresses above the minimum predicted suspension threshold, predicting that at least some dunes should experience erosion due to sand suspension (Table 1).

Another line of reasoning which favors sand suspension considers the relationship between sand's terminal fall velocity and the threshold friction speed. For Martian conditions, shear stresses of ~0.04 Pa can suspend fine sand of ~150 μm size (Bridges et al., 2010). As shown in Table 1, this shear stress should be attainable for at least eastern Herschel. Fine grain sizes of ~150 μm are also realistic, especially given that dune crests have the finest sand grain sizes (Bagnold, 1941).

Wind shear stress could be even higher near the dune crests than we predict: the topography of the dunes is not resolved in the atmospheric model, and wind speeds (and ripple speeds) accelerate up both dune and bedrock slopes on Earth and Mars (Jackson and Hunt, 1975; Lancaster, 1985; Frank and Kocurek, 1996; McKenna Neuman et al., 1997; Momiji et al., 2000; Bridges et al., 2012; Runyon et al., 2017). Turbulent eddies shed from dunes can create powerful updrafts (Anderson and Chemacki, 2014) which may loft grains into higher and faster winds, aiding sand transport downwind where grains may fall out, forming sheets (Figure 3.5). Finally, rapidly fluctuating wall-shear stresses near bedforms' surfaces can create highly localized and brief shear stresses (Orlu and Schlatter, 2011; Mathis et al., 2013) far above the suspension threshold. Considering together the amplification of predicted high shear stresses on dune crests together with

the easily mobilized fine sand strengthens the plausibility of dune erosion from suspension.

In addition to suspension, long-hop saltation could also erode the dunes. At sufficiently high wind shear stresses it may be possible for a sand grain at a dune brink to be launched on a long enough saltation hop so as to land beyond the dune and hence contribute to the dune's erosion. With increasing wind shear stress, the mean saltation speed remains constant but more grains participate in saltation; the speed distribution broadens with more slower and faster grains in the tails of the speed distribution (Kok et al., 2012). It therefore seems plausible the same long-hop saltation erosion could operate on Mars to erode dunes.

Location	Maximum Predicted Shear Stress, Pa
Western Herschel	0.0192
Central Herschel	0.0198
Eastern Herschel	0.0482
Nili Patera	0.0244

Table 3.1. Locations and maximum predicted wind shear stresses from our GCMs, which predict that all locations should experience some dune erosion as the minimum shear stress necessary for suspension may be 0.019 Pa (Nishimura and Hunt, 2000; Jerolmack et al., 2011; Ayoub et al., 2014).

3.4.5. Other Mechanisms

Other hypotheses for sand sheet formation in Herschel-type aeolian fields appear unlikely. Coarser sand grain populations could "armor" the underlying sand and inhibit saltation (Maxwell and Haynes, 2001). However, the presence of active ripples and comparable fluxes on Martian sand sheets suggests that the sand is not much coarser than the sand in active dune fields, if at all, and that a coarse lag deposit is absent. Lower sand volumes than dune fields could also explain sheet formation over dune formation, though not likely in the current upwind to downwind arrangement. The volume of sand in the case study sand sheet, assuming an approximate thickness of 5 m, is ~10^8 m^3. For a comparable 25 km^2 area in the upwind western Herschel dune field where the average dune height is ~22 m with an assumed equivalent uniform sand thickness of ~8 m, the volume of sand is ~2×10^8 m^3. These comparable volumes of sand within a study region suggest the preferential formation of sheets over dunes in central Herschel is not due to lack of sand. Thus these two leading alternate hypotheses seem unlikely, though other processes we have not considered could operate.

The downwind decay in flux observed on the sand sheet is approximately what is predicted from IBL theory (Runyon et al., 2017). The lessening wind shear stress downwind within the IBL—although slightly offset by topography—is the agent we propose ass responsible for allowing sand to come out of suspension and accumulate on the sheets (Figure 3.5).

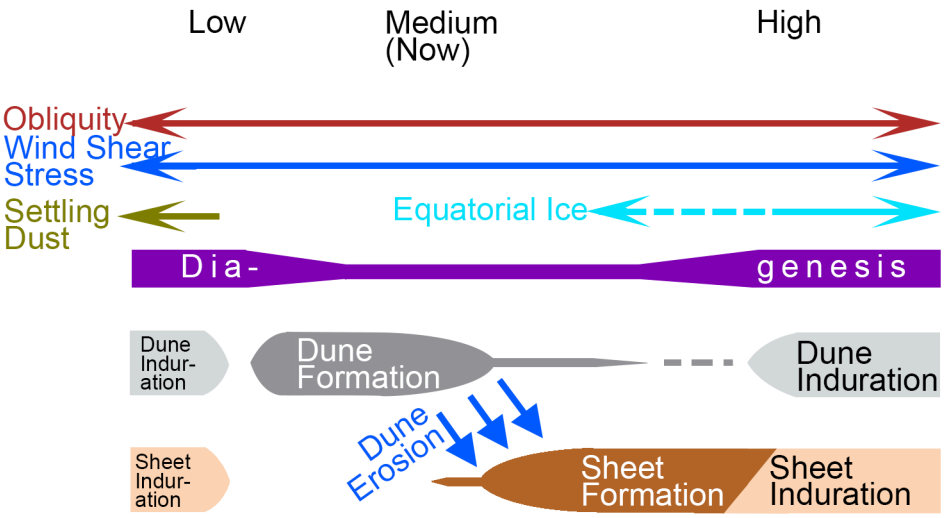

Figure 3.6. Cartoon of obliquity-controlled bedform creation, erosion, and induration cycle. Raising and lowering obliquities change atmospheric density and wind strengths (Haberle et al., 2003), affecting the formation, destruction, and preservation of aeolian deposits. We hypothesize that dune erosion (blue arrows, mid-figure) transfers sand from upwind dunes to downwind sheets. Ice, dust, salt, (Clark, 1982; Jakosky and Christensen, 1986; Bridges et al., 2010) and/or other processes may stabilize and help indurate bedforms (including sheets). Dust suspended in the atmosphere may settle and infiltrate into bedforms when Mars periodically reaches low obliquity.

3.5. Conclusions

We have supported our hypothesis that upwind dunes on Mars erode via suspension into downwind sand sheets on Mars. Characterization of a sand sheet downwind of dunes shows actively migrating ripples in central Herschel Crater with ripple speed behavior consistent with boundary layer flow affected by topography. By taking the locally-unique ratio of ripple flux to total crest flux of local dunes, we used the

ripple flux on the sheet as a proxy for total sand flux. The sheet showed an estimated total sand flux similar to that for dunes on Mars and are therefore not static or armored with coarse grains and are likely sourced from the upwind dunes. Earth's water and vegetation seem to play controlling rolls in both upwind and distal downwind stretches of terrestrial aeolian fields, perhaps leading to drastically different bedform and sheet arrangements compared to Mars.

Observations of sand sheets downwind of sand dunes (uncommon or non-existent on Earth) and wind modeling suggest that at least some current Martian environments are eroding dunes via suspension into sand sheets. This is further substantiated from atmospheric modeling showing shear stresses above the sand suspension threshold and by observing dunes elsewhere on Mars that erode away (Bourke et al., 2008; Chojnacki et al., 2015). Deposits interpreted as paleo-sand sheets suggest cycles of sand deposition and mobilization; dune erosion into sand sheets; and sand sheet induration, which could be followed by depositional epochs of new dunes or re-activation of current dunes, thus repeating the cycle. In such a cycle, sand sheets and dunes may recycle each other's sand, alternately serving as each others' upwind sand source while the whole aeolian system migrates downwind. This appears consistent with other cyclic activities on Mars such as modeling results of Mars' axial obliquity changes (Haberle et al., 2003; Laskar et al., 2004) and observations of glacial landforms (e.g., Head et al., 2003). Future work should include a survey of global Martian sand sheet, paleosheets, and dune activity. Comparing flux estimates to local nested mesoscale atmospheric models could likewise suggest whether other Martian dunes are eroding into sand sheets.

Acknowledgements

N.T. Bridges was supported via NASA grant MDAP NNX12AJ41G, "Advanced Change Detection of Martian Dunes." Claire Newman was supported by NASA Mars Fundamental Research Program grant number NNX11AF59G and all simulations were performed on the NASA High End Computing Pleiades cluster at NASA Ames. K.D. Runyon is funded by the support of the APL Graduate Student Fellowship Program. The original remote sensing data are available online via the NASA Planetary Data System (PDS) and at www.uahirise.org. The atmospheric circulation data, DTMs, and co-registered images are available upon request from the corresponding author. We are grateful to Sarah Sutton for providing the DTMs as part of the HiRISE project and to Matt Chojnacki for helpfully answering DTM-related questions. We thank M. Day, R. Ewing, P. Johnson, G. Kocurek, N. Lancaster, and D. Rubin for engaging and helpful discussions.

References

Almeida, M.P., E.R.J. Partelli, J.S. Andrade Jr., and H.J. Herrmann, 2008. Giant saltation on Mars. PNAS 105, 17, 6222-6226, www.pnas.org/cgi/doi/10.1073/pnas.0800202105.

Anderson, R.S., 1987. A theoretical model for aeolian impact ripples. Sedimentology, 34, 943-956, doi:10.1111/j.1365-3091.1987.tb00814.x.

Anderson, W., Chemacki, M., 2014. Numerical study of turbulent flow over complex aeolian dune fields: The White Sands National Monument. Phys. Rev. E 89, doi:https://doi.org/10.1103/PhysRevE.89.013005.

Ayoub, F., et al., 2014. Threshold for sand mobility on Mars calibrated from season variations of sand flux. Nat. Commun. 6096, 1–8. http://dx.doi.org/10.1038/ncomms6096.

Bagnold, R.A. 1941. The physics of blown sand and desert dunes. Metheun, London, 265 pp.

Bourke, M.C., K.S. Edgett, and B.A. Cantor, 2008. Recent aeolian dune change on Mars. Geomorphology, 94, 247-255, doi:10.1016/j.geomorph.2007.05.012.

Breed, C.S., McCauley, J.F., Davis, P.A., 1987. Sand sheets of the eastern Sahara and ripple blankets on Mars. From Desert sediments: Ancient and modern. Frostick, L., and Reid, I., eds. Geological Society Special Publications no. 35, p. 337-359, doi:10.1144/GSL.SP.1987.035.01.23.

Bridges, N.T., et al., 2010. Aeolian bedforms, yardangs, and indurated surfaces in the Tharsis Montes as seen by the HiRISE camera: Evidence for dust aggregates. Icarus, 205, 165-182, http://dx.doi.org/10.1016/j.icarus.2009.05.017.

Bridges, N.T., et al., 2012. Earth-like sand fluxes on Mars. Nature 485, 339. http://dx.doi.org/10.1038/nature11022.

Chojnacki, M., Burr, D.M., Moersch, J.E., Wray, J.J., 2014. Valles Marineris dune sediment provenance and pathways. Icarus 232, 187–219. http://dx.doi.org/10.1016/j.icarus.2014.01.011.

Chojnacki, M., Johnson, J.R., Moersch, J.E., Fenton, L.K., Michaels, T.I., Bell, J.F. III, 2015. Persistent aeolian activity in Endeavour crater, Meridiani Planum, Mars; new observations from orbit and the surface. Icarus, 251, p. 275-290, http://dx.doi.org/10.1016/j.icarus.2014.04.044.

Clark, B., 1982. Analysis and interpretation of Viking inorganic chemistry data (Mars Data Analysis Program). Final Report, MCR-81-653, from NASA Technical Reports Server, https://ntrs.nasa.gov/search.jsp?R=19820022330.

Ehlmann, B.L., et al., 2011. Subsurface water and clay mineral formation during the early history of Mars. Nature, 479, 53, doi:10.1038/nature10582.

Frank, A. J. and G. Kocurek, 1996. Airflow up the stoss slope of sand dunes: limitations of current understanding, Geomorphology, 17, p. 47-54, doi:10.1016/0169-555X(95)00094-L.

Fryberger, A.M. Al-Sari, T.J. Clisham, 1983. Eolian dune, interdune, sand sheet, and siliciclastic Sabkha sediments of an offshore prograding sand sea, Dhahran Area, Saudi Arabia. AAPG Bull., 67, 2, 280-312.

Fryberger, S.G., A.M. Al-Sari, T.J. Clisham, S.A.R. Rizvi, and K.G. Al-Hinai, 1984. Wind sedimentation in the Jafurah sand sea, Saudi Arabia. Sedimentology, 31, 413-431, doi:10.1111/j.1365-3091.1984.tb00869.x.

Fryberger, S.G., T.S. Ahlbrandt, and S. Andrews, 1979. Origin, sedimentary features, and significance of low-angle eolian “sand sheet” deposits, Great Sand Dunes National Monument and vicinity, Colorado. J. Sed. Petrol., 49, 3, p. 733-746.

Golombek, M.P., and Bridges, N.T., 2000. Erosion rates on Mars and implications for climate change: Constraints from the Pathfinder landing site. JGR, 105, E1, 1841-1853, doi:10.1029/1999JE001043.

Greeley, R., J.D. Iverson 1985. Wind as a geological process on Earth, Mars, Venus, and Titan. Cambridge UP, 348 p., ISBN-13: 978-0521359627.

Haberle, R.M., Murphy, J.R., Schaeffer, J., 2003. Orbital change experiments with a Mars general circulation model. Icarus, 161, 66-89, http://dx.doi.org/10.1016/S0019-1035(02)00017-9.

Hayward, R.K., et al., 2006. Mars global digital dune database: MC2-MC29. U.S. Geological Survey Open-File Report 2007-1158. http://pubs.usgs.gov/of/2007/1158/.

Head, J.W., F.J. Mustard, M.A. Kreslavksy, R.E. Milliken, D.R. Marchant, 2003. Recent ice ages on Mars. Nature, 426, 797-802, doi:10.1038/nature02114.

Jackson, P. S., and J. C. R. Hunt (1975), Turbulent wind flow over a low hill, Quart. J. R. Met. Soc., 101, p. 929-955, doi:10.1002/qj.49710143015.

Jakosky, B.M., Christensen, P. R., 1986. Global duricrust on Mars: Analysis of remote-sensing data. JGR, 91, B3, p. 3547-3559, doi:10.1029/JB091iB03p03547.

Jerolmack, D.J., Reitz, M.D., Martin, R.L., 2011. Sorting out abrasion in a gypsum dune field. J. Geophys. Res. 116, F02003. http://dx.doi.org/10.1029/2010JF001821.

Jerolmack, D.J., et al., 2012. Internal boundary layer model for the evolution of desert dune fields. Nat. Geosci. 5, 206–209. http://dx.doi.org/10.1038/ngeo1381.

Kasse, C., 1997. Cold-climate aeolian sand-sheet formation in north-western Europe (c. 14-12.5 ka); a response to permafrost degradation and increased aridity. Permafrost and Periglacial Processes, v. 8, 295-311, doi:10.1002/(SICI)1099-1530(199709)8:3<295::AID-PPP256>3.0.CO;2-0.

Kocurek, G., and R.C. Ewing, 2012. Source-to-sink: An Earth/Mars comparison of boundary conditions for eolian dune systems. SEPM Spec. Pub. No. 102, http://dx.doi.org/10.2110/pec.12.102.0151.

Kocurek, G., and J. Nielson, 1986. Conditions favourable for the formation of warm-climate aeolian sand sheets, Sedimentology, 33, p. 795-816, doi:10.1111/j.1365-3091.1986.tb00983.x.

Kok, J.F., Parteli, E.J.R., Michaels, T.I., Bou Karman, D., 2012. The physics of wind-blown sand and dust. Rep. Prog. Phys. 75. http://dx.doi.org/10.1088/0034-4885/75/10/106901.

Lancaster, N., 1985. Variations in wind velocity and sand transport on the windward flanks of desert sand dunes: Sedimentology, 32, 581-593, DOI: 10.1111/j.1365-3091.1985.tb00472.x.

Lapotre, M.G.A., et al., 2016. Large wind ripples on Mars: A record of atmospheric evolution. Science, 353, 6294, doi:10.1126/science.aaf3206.

Laskar, J., et al., 2004. Long term evolution and chaotic diffusion of the insolation quantities of Mars. Icarus, 170, 343-364, http://dx.doi.org/10.1016/j.icarus.2004.04.005.

Leprince, S., et al., 2007. Automatic and precise orthorectification, coregistration, and subpixel correlation of satellite images, application to ground deformation measurements. IEEE Trans. Geosci. Remote Sens. 45, 1529–1558. doi: 10.1109/TGRS.2006.888937.

Mathis, R., Marusic, I., Chernyshenko, S.I., and Hutchins, N., 2013. Estimating wall-shear-stress fluctuations given an outer region input.

Maxwell, T.A., and C.V. Haynes Jr., 2001. Sand sheet dynamics and Quaternary landscape evolution of the Selima Sand Sheet, southern Egypt. Quaternary Sci. Rev., 20, 1623-1647, doi:10.1016/S0277-3791(01)00009-9.

McEwen, S., et al., 2007. Mars Reconnaissance Orbiter's High Resolution Imagine Science Experiment (HiRISE). J. Geophys. Res. 112 (E5). http://dx.doi.org/10.1029/2005JE002605.

McKee, E.D., 1966. Structures of dunes at White Sands National Monument, New Mexico (and a comparison with structures of dunes from other selected areas). Sedimentology, 7, 1, 3-69, doi:10.1111/j.1365-3091.1966.tb01579.x.

McKenna Neuman C., N. Lancaster, and W. G. Nickling, 1997. Relations between dune morphology, air flow, and sediment flux on reversing dunes, Silver Peak, Nevada, Sedimentology 44, doi:10.1046/j.1365-3091.1997.d01-61.x.

Mitasova, H., M. Overton, and R.S. Harmon, 2005. Geospatial analysis of coastal sand dune field evolution: Jockey's Ridge, North Carolina. Geomorphology, 72, 204-221, doi:10.1016/j.geomorph.2005.06.001.

Momiji, H., R. Carretero-González, S. R. Bishop, and A. Warren, 2000. Simulation of the effect of wind speedup in the formation of transverse dune fields, Earth Surf. Proc. and Landforms, 25, p. 905-918.

Newman, C.E., et al., 2017. Winds measured by the Rover Environmental Monitoring Station (REMS) during the Mars Science Laboratory (MSL) rover's Bagnold Dune campaign and comparison with numerical modeling using MarsWRF. Icarus, in press, http://dx.doi.org/10.1016/j.icarus.2016.12.016.

Nishimura, K., and J.C.R. Hunt, 2000. Saltation and incipient suspension above a flat particle bed below a turbulent boundary layer. J. Fluid Mech., 417, 77-102, I: https://doi.org/10.1017/S0022112000001014.

Orlu, R., Schlatter, P., 2011. On the fluctuating wall-shear stress in zero pressure-gradient turbulent boundary layer flows. Physics of Fluids, 23, http://dx.doi.org/10.1063/1.3555191

Ould Ahmedou, D. et al., 2007. Barchan dune mobility in Mauritania related to dune and interdune sand fluxes. JGR Earth Surf., 112, F2, doi:10.1029/2006JF000500.

Richardson, M.I., Toigo, A.D., Newman, C.E., 2007. PlanetWRF: A general purpose, local to global numerical model for planetary atmospheric and climate dynamics. JGR-Planets, 112, E9, doi:10.1029/2006JE002825.

Royal Geographical Society, 2010. Global sand seas: past, present, future. British Society for Geomorphology, one-day meeting abstracts. ftp://ftp.shef.ac.uk/pub/uni/academic/D-H/geog/namibsandsea/conference/Global_Sand_Seas_abstracts.pdf

Runyon, K.D., N.T. Bridges, F. Ayoub, C.E. Newman, and J.J. Quade, 2017. An integrated model for dune morphology and sand fluxes on Mars. Earth Plan. Sci. Lett., 457, 204-212, doi:10.1016/j.epsl.2016.09.054.

Runyon, K.D., N.T. Bridges, F. Ayoub, C.E. Newman, and J.J. Quade, 2017. Corrigendum to An integrated model for dune morphology and sand fluxes on Mars. Earth Plan. Sci. Lett., 460, 320-321, http://dx.doi.org/10.1016/j.epsl.2016.12.026.

Silvestro, S., Fenton, L.K., Vaz, D.A., Bridges, N.T., Ori, G.G., 2010. Ripple migration and dune activity on Mars: Evidence for dynamic wind processes. GRL 37, 20, doi:10.1029/2010GL044743.

Sutton, S.S., M. Chojnacki, and A. Kilgallon, 2015. Precision and accuracy of simultaneously collected HiRISE digital terrain models. LPSC Abstract #3010.

White, B.R., Greeley, R., Ivesen, J.D., Pollack, J.B., 1976. Estimated grain saltation in a Martian atmosphere. JGR, 81, P. 5643–5650, doi:10.1029/JB081i032p05643.

Appendix B: Supplementary Information

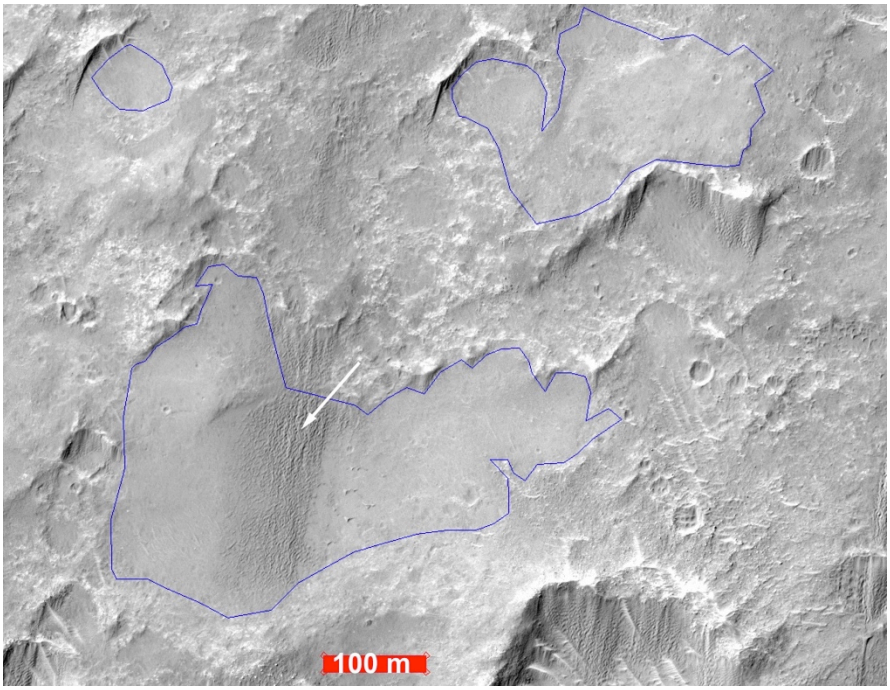

Figure B1. The blue outlines roughly define the boundaries for a few of the many Smooth Unit outcrops in central Herschel Crater. Their location downwind of topography (often crater rims) suggests they may be indurated paleosheets. A new "micro" sand sheet appears (white arrow) atop the putative paleo-sand sheet in the lee of topography. HiRISE image ESP_025487_1655. Credit: NASA/University of Arizona.

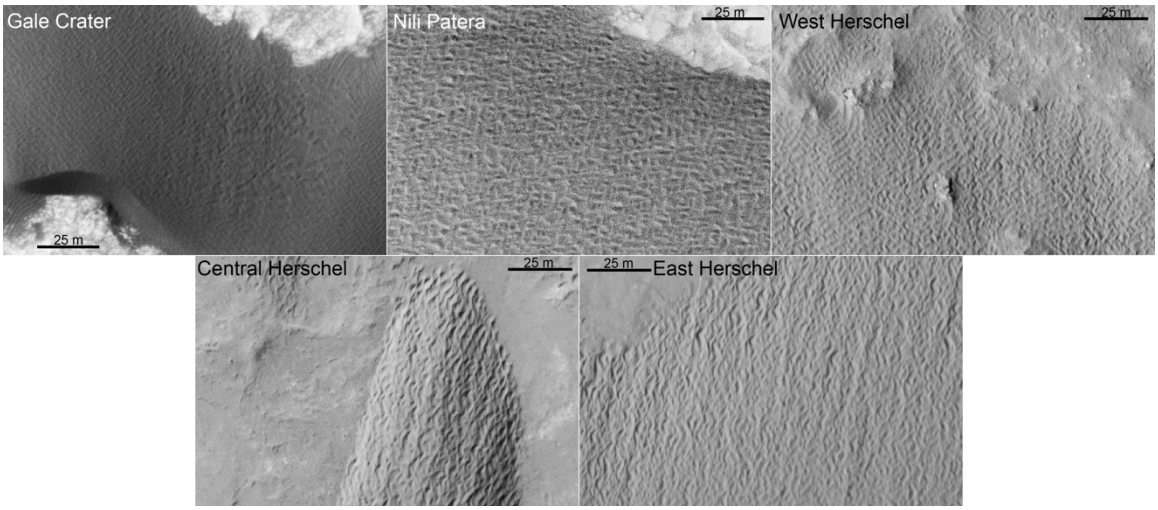

Figure B2. Ripple morphology comparison between five Martian locations. Globally on Mars, ripples span a small range of wavelengths of 2.9 ± 0.7 m (Lapotre et al., 2016; error is 1 standard deviation) with Gale Crater ripples being a bit smaller at 2.1 ± 0.6 m (Lapotre et al., 2016) or 1.9 ± 0.2 m (Silvestro et al., 2016). We classify the central Herschel ripples as the same type found elsewhere on Mars. Each HiRISE image cutout was displayed in JMARS at a scale of 524288 pixels/degree. From left to right, top to bottom, the HiRISE images are ESP_035917_1755, PSP_004339_1890, PSP_002860_1650, ESP_016916_1655, and PSP_002728_1645. Image credit: NASA/JPL/University of Arizona.

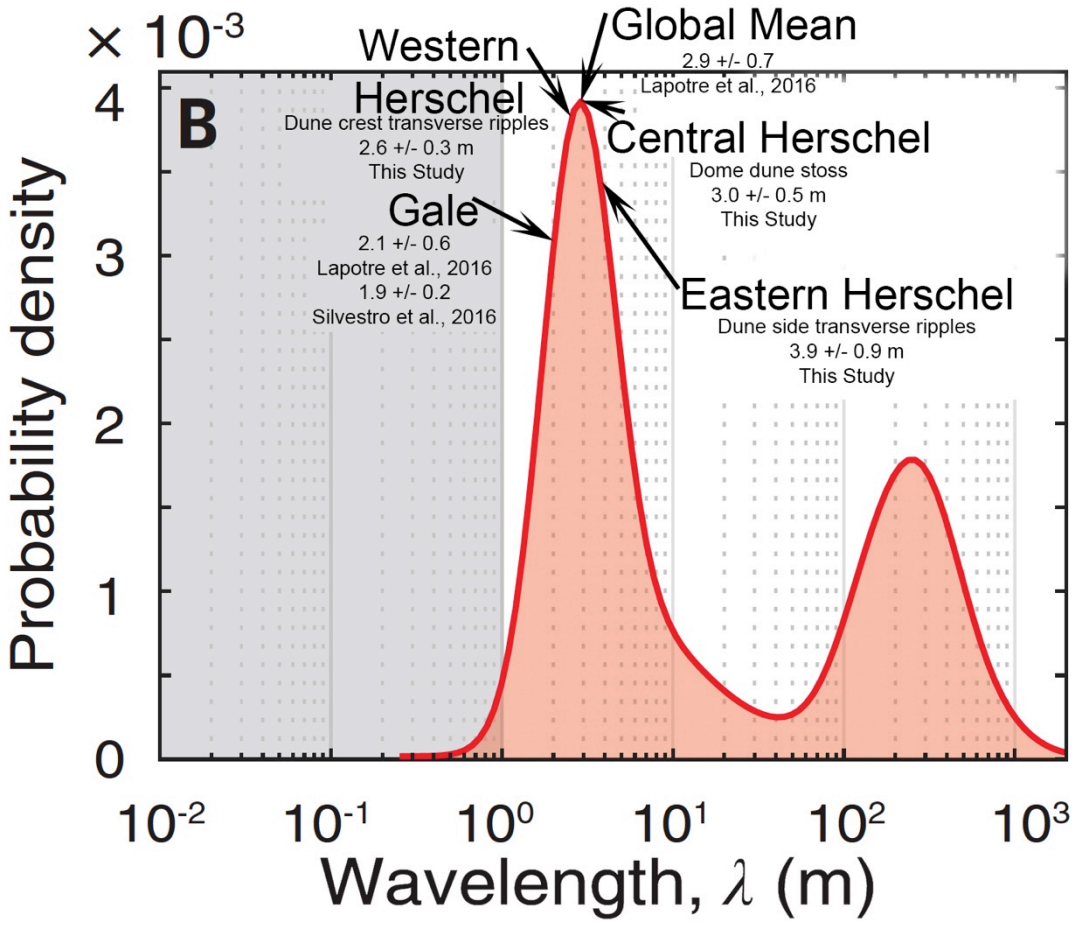

Figure B3. Probability density function of ripples (left spike) and dunes (right spike) for Mars as measured from orbital data. The wavelength of ripples (in meters) for different locations are highlighted. All ripples considered in the text are in the same size population. Figure modified from Lapotre et al. (2016).

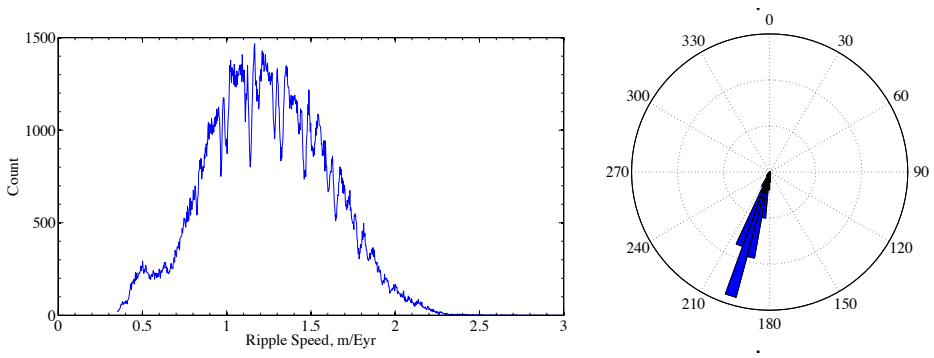

Figure B4. *Left:* The mean ripple speed is 1.25 ± 0.36 m/Eyr (±1 sigma) for the central Herschel sand sheet case study. *Right:* The central Herschel sand sheet wind directional azimuth (where the wind blows *to*) is 196˚ ± 9˚ (to the SSW). Both histograms used 1000 bins.

Name or Description	Latitude, ˚N	Longitude, ˚E
270 km east of Gledhill Crater in Aonia Terra	-53.4	-94.8
Western side of Lowell Crater	-52	-83.4
Crater 254 km northeast of Lowell Crater	-48.5	-77.5
Ogygis Undae	-49.7	-66.5
80 km southeast of Eger Crater in NW Argyre Planitia	-48.7	-49.9
Rabe Crater	-43.8	34.8
Crater 953 km west of Herschel Crater	-13.8	113
Crater 853 km west of Herschel Crater	-15.4	114.4
Crater 400 km west of Herschel Crater	-14.7	122.9
Crater 370 km west northwest of Herschel Crater	-13.7	123.4
Crater 293 km west northwest of Herschel Crater	-13.6	124.8
Crater 242 km west northwest of Herschel Crater	-13.8	125.7
Intercrater plain 223 km west northwest of Herschel Crater	-14	126

Table B1. Non-exhaustive list from Google Mars survey of examples on Mars of sheets downwind of dunes other than Herschel Crater, Gale Crater, and Nili Patera.

Name or Description	Latitude, ˚N	Longitude, ˚E
White Sands, NM	32.9	-106.3
Southeastern Abu Dhabi, UAE	22.8	54.7
Akchar Desert, Mauritania	19	-11
Rigestan Desert, Kandahar, Afghanistan	30.6	65.1
Taklimakan Desert, China	40	88.3
Near Quillian Mountains, China	40	99.4

Table B2. Non-exhaustive list from Google Earth survey of examples on Earth of sheets upwind of dunes, serving as the dunes' sand source.

	Western Herschel	Central Herschel	Eastern Herschel	Nili Patera
Stereo 1	PSP_002860_1650*	ESP_016916_1655	ESP_037948_1645*	ESP_017762_1890*
Stereo 2	PSP_003572_1650	ESP_017417_1655*	ESP_038291_1645	ESP_018039_1890
3rd Ortho-photo & Change Detection	ESP_020384_1650*	ESP_025487_1655*	PSP_002728_1645*	PSP_004339_1890* PSP_005684_1890*

Table B3. HiRISE images used in this study. Stereo 1 and Stereo 2 are HiRISE images used in generating the DTM and initial orthoimages. A third image is then orthorectified to the DTM. *Used in ripple and slip face change detection.

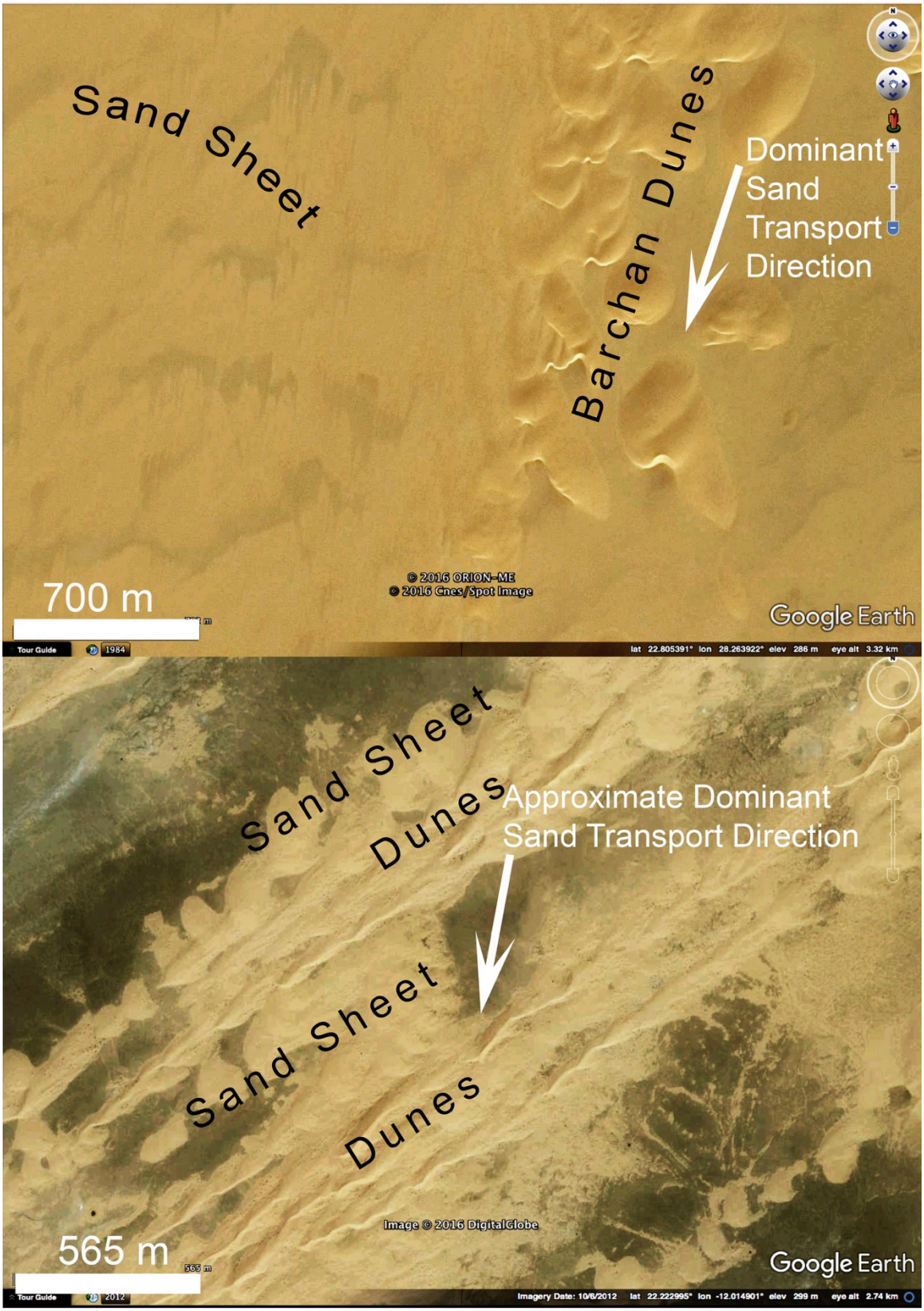

Figure B5. Examples from Earth of sand sheet and dune arrangement in contrast to Mars.

Top: Southern Egypt (22.8˚N, 28.5˚E). The sand sheet is adjacent to the dunes relative to the dominant sand transport direction based on slip face orientation. *Bottom*: Northwest Mauritania (22.2˚N, -12.0˚E) where the sheets form upwind to dunes. The entire aeolian system terminates downwind to the south where dunes (not sheets) abut against a bedrock butte (not shown). Contrast-enhanced images from Google Earth. Note the different scale bars in the lower left corner of each.

Chapter 4: Preliminary laboratory investigations of ejecta emplacement dynamics and morphology with planetary applications

Kirby D. Runyon and Olivier S. Barnouin

Abstract

The preponderance of impact craters and the associated crater ejecta facies are leading agents of geomorphic change across the Solar System. Interpretation of planetary landscape evolution, sample provenance, and regolith gardening all benefit from a thorough understanding of ejecta emplacement dynamics. Constraining ejecta emplacement dynamics has eluded experimentation even as the effects of primary impacts have become well-constrained from experiments and numerical simulations and have been shown to follow power law scaling rules. To address the knowledge gap surrounding granular ejecta emplacement, we built and characterized a novel ejecta emplacement catapult and showed it to accurately reproduce the ejecta mass and velocity profiles predicted for in-flight natural ejecta curtains. Based on this dynamic similarity to larger, natural systems, we proceeded with a preliminary suite of experiments to constrain runout and erosion efficiencies of flowing ejecta. Our quantitative results 1) may suggest a new set of scaling rules for granular systems emplaced more slowly than hypervelocity impacts; and 2) show ejecta runout efficiencies of ~1-2, which are similar to terrestrial debris flows 12 decades more voluminous with significant erosive efficiencies of ~2-4%. Our qualitative results reveal ejecta emplacement to be a stochastic, heterogeneous, erosive, and depositional system capable of lateral and vertical mixing and displacement of both ejecta and regolith. Together with the initial results showing ejecta emplacement

to be violently dynamic, the development of this new laboratory technique will allow more detailed study in the future to better inform interpretations of sample provenance, ejecta stratigraphy, and geochemical boundaries.

Key Words: Impact Cratering, Ejecta, Experimental Methods

4.1. Introduction

Impact cratering is the most common geologic process that influences the surfaces of solid worlds across the solar system (Shoemaker, 1962; Gault et al., 1968; Oberbeck, 1975; Housen and Holsapple, 2011). It follows that on worlds where the gravity is sufficient to retain ejecta, the emplacement of the excavated crater ejecta might be just as influential given that the surface area of ejecta deposits is typically large relative to its source crater (Figure 4.1). Compared to the extensive studies exploring cratering mechanics and crater geomorphology (e.g., Holsapple, 1993; Melosh 1989; Schultz and Gault, 1985; Barnouin-Jha et al., 2007), few investigations have addressed the dynamics of ballistic ejecta emplacement, especially within a few crater radii from the rim (e.g., Oberbeck et al., 1975; Pieters et al., 1985).

Ejecta does not simply remain where it lands: Oberbeck (1975) introduced the concept of ballistic sedimentation in which deposited ejecta creates secondary craters, erodes, and incorporates itself with the original pre-impact regolith. Evidence from striae, polish, and detachment folds in limestone ejecta fragments at Germany's Ries Crater (Chao, 1974; Chao, 1976; Hörz et al., 1983; Kenkmann and Ivanov, 2006; Kenkmann and Schönian, 2006;) indicate that ballistic ejecta slide while eroding local material, yet

this has been largely ignored or, early on, even contested (Oberbeck et al., 1975) when considering ejecta on other planets, including the Moon and Mars. Ghent et al. (2016) used radar and near infrared observations of lunar ejecta to strongly suggest post-depositional runout to explain abrupt boundaries of radar haloes around craters. In the case of Mars, layered ejecta that show contiguous ramparts and lobate deposits (e.g., Carr, et al. 1977; Mouginis-Mark, 1979; Schultz, 1992; Barlow, 1994; Boyce and Mouginis-Mark, 2006; Barnouin-Jha et al., 2005; Robbins and Hynek, 2012; Barlow et al., 2014; Wada and Barnouin-Jha, 2006) show abundant evidence for surface flow and underscores the importance of understanding the detailed mechanics of ballistic ejecta emplacement and subsequent lateral flow after its initial deposition (Carr et al., 1977; Schultz, 1992; Ivanov et al., 1994; Ivanov et al., 1997; Wada and Barnouin-Jha, 2006). Numerous geomorphologies in ejecta facies on Mars and some icy moons suggest post-depositional flow emplacement such as distal ramparts in Martian ejecta which appear to divert around obstacles or otherwise flow (e.g, Carr et al, 1977; Schultz et al., 1992; Mouginis-Mark, 1979; Baloga et al., 2005; Barlow, 2005; Boyce and Mouginis-Mark, 2006; Wada and Barnouin-Jha, 2006; Boyce et al., 2010).

Besides addressing observed flow of ejecta and the resulting morphologies, a better understanding of the range of possible transport histories of ejecta and regolith parcels also will aid in petrologic and provenance interpretation of samples and remote sensing datasets. For instance, compositions across physiographic boundaries on the Moon remain difficult to explain. Detailed investigations of the processes associated with regolith mobilization and mixing ("gardening") by ejecta should provide needed clarity, given that such process are often invoked to explain multispectral and morphological

observations (Li & Mustard 2000, 2003, and 2005; Oberbeck, Morrison, and Horz, 1975). Such investigations of ejecta dynamics should also illuminate how transportation of geologic materials away from their source lithologies influence sample provenance interpretation, geochronometry, and other geochemical investigations. To wit: recent analyses of Apollo and Luna samples suggest Imbrium ejecta dominates the sample collections (Haskin 1998; Cohen et al., 2005).

Historically, cratering experiments and nuclear explosions, along with data from a few lunar craters, have led to a commonly used model (e.g. Melosh, 1989) where ejecta thickness decays with distance from a crater rim as a power law with a slope of -3 (McGetchin et al., 1973). Crater scaling relations (Housen et al., 1983) predict such a relationship when ejecta does not flow along the ground after deposition for gravity-controlled craters where target strength is not important. Rather, the crater scaling relationship assumes that ejecta are deposited as a coherent blanket with some bulking; and that the origin and volume of the ejected material in the blanket can be directly traced back along ballistic trajectories to source regions within the crater (Hartmann, 1985; Housen et al., 1983 and Holsapple, 2011).

Many investigations (e.g., Oberbeck, 1975; Chao, 1974; 1976; Hörz et al., 1983, Kenkmann and Ivanov, 2006; Kenkmann and Schönian, 2006) indicate that it is likely not so simple to trace ballistic paths from the ejecta blanket back into the crater to determine ejecta provenance. Recent topographic and radar data from the Moon reveal that ejecta topography and thickness (e.g., Stickle et al., 2016) often show wide variation in the power law slope of ejecta thickness decay profiles. This thickness variation is possible evidence for post-depositional flow and near surface gardening, such as would happen

during surface erosion and mixing. A detailed assessment of the dynamics of ejecta emplacement would lead to quantifying the degree of mixing between primary ejecta and target and how much lateral displacement might be expected. This assessment would better link observed ejecta thicknesses and the volumes of ejecta excavated from craters. For those cases where significant local material has not been incorporated in the deposit during ejecta emplacement, such an assessment will also help establish the provenance of ejecta from within a crater.

Given the importance quantifying the dynamics of ejecta emplacement, we initiated a series of novel large-scale laboratory experiments that investigate the emplacement of a granular ejecta simulant. Inspired by the use of debris flow flume studies in the terrestrial geohazard community (Iverson, 1997; Iverson et al., 2011; Iverson, 2015) and clustered hypervelocity impact experiments (Schultz and Gault, 1985), we use an ejecta catapult (Figure 4.2) to simulate ejecta curtains using gravel as an ejecta simulant. We use these experiments to gain new inferences on how ballistic ejecta—a granular system—interacts with a target surface. The catapult allows us to measure the ability of ejecta to erode and flow across a target surface.

In the next sections, we provide the theoretical framework for the suite of experiments we undertook that is necessary to show how the catapult ejecta are representative of crater ejecta. We include a discussion of the derivation of the energy balance between the kinetic energy of sliding ejecta and runout (e.g., Erismann and Abell, 2001), and a dimensionless model for ejecta erosive efficiency. We then describe in detail the laboratory catapult and demonstrate that an experimental ejecta curtain is dynamically similar to natural ejecta and can therefore scale to the planetary-sized impact

craters. This is followed by a set of experiments where we explore laboratory results for ejecta runout, erosive efficiency, and gardening, which may be indicative of the type of processes occurring at planetary craters. A discussion extrapolating some of our findings to natural craters concludes our paper along with a discussion of future research directions.

4.2. Theoretical Framework

Because this is the first use of our laboratory catapult to simulate ejecta, our objectives are two-fold: 1) to characterize the range of real world conditions our laboratory experiments simulate and then 2) to use those results to quantify and characterize the range of sedimentological processes that occur during ejecta emplacement at planetary scales. The first task requires comparison of experimental results to theoretical models of crater excavation and ejecta flight developed over decades (e.g., Gault et al., 1968; Schmidt and Holsapple, 1980; Schultz and Gault, 1985; Holsapple, 1993; Housen and Holsapple, 2011) to demonstrate that our lab ejecta curtain can be representative of a larger, natural ejecta curtain using reasonable scaling arguments (Objective 1). With confidence that the lab curtain is thus dynamically similar to larger, faster, crater-derived ejecta, we can use our results to infer how the ballistic emplacement of crater ejecta affects geologic processes on planetary surfaces (Objective 2).

4.2.1. Erosive Efficiency and Gravity Scaling

One geologic metric of granular flow is its erosive efficiency, defined as the ratio of eroded mass *M* to emplaced mass *m* as *M/m*. In hypervelocity clustered impactor cratering studies (Schultz and Gault, 1985), this is called cratering efficiency (borrowing the term developed for cratering by Holsapple and Schimdt, (1982)), but is conceptually identical to erosive efficiency. In their hypervelocity impact experiments, Schultz and Gault (1985) found that clustered "clouds" of impactors with increasingly higher dispersion were much less efficient at cratering than monolithic impactors of the same mass. In fact, their most disperse hypervelocity clustered impactors produced "crater" morphologies more reminiscent of erosive gouging than classical cratering. This clustered gouging is what one might expect to occur from ejecta deposited beyond the edge of the continuous ejecta of a primary crater and in crater rays. They also showed that more projectile material stayed on the surface during a clustered impact, thus strengthening the analogy between clustered impactors and proximal ejecta emplacement.

The analogy between clustered impactors and ejecta facies extends to crater rays as well. The extreme heterogeneity of both the geomorphology and spectra from the rays of Copernicus Crater on the Moon are consistent with the clustered cratering experiments, especially where modeled spectra better matches large *M*/*m* values (Pieters et al., 1985). For more dispersed individual secondary craters associated with more distal rays, Pieters et al.'s (1985) results follow the expectations of the Oberbeck et al. (1975) model in which individual ejecta particles are treated as individual projectiles, and ejecta emplacement is highly erosive, resulting in deposits dominated by locally eroded material (i.e., $M/m >> 1$). Here, we make use of relationships between the inertial properties

(described below) of incoming ejecta and measured *M/m* of the deposit, and data on the physical displacement of the target surface during ejecta emplacement, to gain similarly useful insights regarding the role of ejecta erosion in displacing and mixing regolith.

We use non-dimensional scaling to capture the erosive efficiency of the ejecta. This allows our results to scale up to planetary scales. Using non-dimensional terms also has the advantage that it avoids the need for our experiments to simultaneously match both the velocity and mass distribution profiles from a true impact event because these values are parameterized in the terms (Eq. 1). We assume the inertial properties of the ejecta drive surface erosion as opposed to the ejecta's kinetic energy. Given the similarities between continuous ejecta's dynamics and the sparsely clustered projectile impacts investigated by Schultz and Gault (1985), we use their same approach and employ the dimensionless parameter π_2 to parameterize the erosive efficiency of ejecta, where

$$\frac{M}{m} = f(\pi_2) = f\left(\frac{3.22gr}{v_c^2}\right). \quad \text{(Eq. 1)}$$

The factor of 3.22 is maintained for historical reasons (see Holsapple, 1993 for details) so we can compare our results for ejecta to past cratering and clustered impact results. Historically, impact experiments demonstrated that for dispersed projectiles simulating distal ejecta, cratering efficiency *M*/*m* as a function of π_2 follows simple power laws, albeit with some scatter compared to monolithic projectiles (Schultz and Gault, 1985). Power laws from impact experiments spanned several orders of magnitude for both π_2 and *M*/*m*. Extrapolating these power laws to planetary surfaces revealed the degree of cratering efficiency expected. In cratering and clustered impact experiments *r* is a measure of projectile radius, and the other variables are defined in Table C1 (Appendix

C). The parameter π_2 is the inverse of the usual definition of the Froude number, and states the inertial effects of the falling ejecta are countered by the gravitational forces preventing erosion of the target when the ejecta interacts with the surface. By using the Froude number, we assume all impacting ejecta interacts with the surrounding target surface in the gravity regime as opposed to the strength regime. This assumption is probably reasonable because most planetary surfaces encountered by ejecta are loose and unconsolidated granular regoliths that are easily overwhelmed by the inertia of thick (>50 m) and fast-moving (>100 m/s) ejecta expected from large craters (>1 km in diameter). In the case of ejecta deposition, the physical scale of an ejecta curtain just prior to impact is captured by the length scale, *r*, which we have chosen to be the width, *w* of the curtain's footprint on the surface (Figure 4.3). We assume that this length scale is the most reasonable primary physical length scale that drives surface erosion by ejecta at each ejecta landing position. This implies that unlike for cratering, the ejecta's π_2 value changes radially away from the crater due to the shortening footprint (Richardson, 2011) and the increasing landing velocity of the debris in the ejecta curtain. In order to employ Equation 1 to predict erosive efficiency, we need an estimate of the thickness of a natural ejecta curtain, considered next.

4.2.2. Ejecta Curtain Width and Position

In nature, the thickness and therefore footprint of an in-flight ejecta curtain depends on the target rock's strength (Holsapple and Housen, 2007; Richardson, 2011). The material in the leading (anti-crater-facing) edge of the curtain is launched essentially at $t = 0$ as the shock-rarefaction waves passes through the target (Melosh, 1989); the

curtain's trailing (crater-facing) edge is populated by grains launched from progressively deeper depths, and its location relative to the impact point depends on how easily the crater was excavated. The curtain is thicker for gravity-dominated and progressively thinner for strength-dominated cratering events (Richardson, 2011). The thickness is controlled by energy conservation: in strengthless materials, a maximum of energy is available for excavation and not for breaking material (i.e. overcoming strength). This results in a more massive and therefore thicker ejecta curtain for a strengthless target.

For our investigation, we estimate w (=r in Equation 1) by using ejecta crater scaling rules that have been tuned to impact experiments in weak, gravity-controlled granular media, which is a reasonable assumption when considering planetary scale impacts. Combining Z-model predictions (Maxwell, 1977) with results from impact experiments (Cintala et al., 1999; Barnouin-Jha et al., 2007), Richardson and colleagues (Richardson et al., 2007; Richardson, 2011) derived equations for calculating the position of the front and back of an ejecta curtain, thus giving the footprint of the curtain width projected on the ground. Using this approach, we calculate a footprint width as a function of radial distance beyond the transient crater center (Figure 4.4). We determine the landing positions of the back and front of the curtain using ballistics as (see the Appendix for more detail)

$$L_{cb} = x_{db} + \frac{\cos(\theta) v_{eb} t_b}{R} \quad \text{(Eq. 2)}$$

$$L_{cf} = x_{df} + \frac{\cos(\theta) v_{ef} t_f}{R}, \quad \text{(Eq. 3)}$$

where L_{cb} and L_{cf} are the back and front positions of the ejecta curtain and the variables are defined in the Appendix. Then

$$w(x_{land}) = L_{cf} - L_{cb} \quad \text{(Eq. 4)}$$

where x_{land} is the landing position at the middle of the curtain. The ejecta mass m deposited at x_{land} from a crater of transient radius R found across w is given by the ejecta scaling rules as

$$m(x_{land}) = \rho k_m R^3 (x_{df}^3 - x_{db}^3) \quad \text{(Eq. 5)}$$

where k_m is described in the Appendix. Predicting m will allow correlating our catapult ejecta results with the theoretical radius of the corresponding "imaginary crater." We will normalize this m by the area over which the ejecta is deposited in order to facilitate comparisons with the mass per unit area measured in our experiments. This new term is defined as m_a.

Besides w, π_2 calls for the ejecta landing velocity v_c (before sliding) at x_{land}. This is obtained by using the launch velocity equation

$$v_c = k_2 \sqrt{Rg} \left(\frac{x_\ell}{R}\right)^{\frac{-1}{\mu}} \quad \text{(Eq. 6)}$$

with

$$x_{land} = x_\ell + v_c T_f \cos(\theta) \quad \text{(Eq. 7)}$$

and inverting the results to establish a relationship for $v_c = v_e$ as function of x_{land}, which for ballistic situations is true when an atmosphere does not significantly decelerate individual ejecta.

4.2.3. Runout Efficiency

When an ejecta curtain lands on the ground, it continues to flow along the ground for a given distance until friction stops it. In the case of debris flows or rock avalanches, the runout efficiency measures how effectively the flow's original potential energy is lost as it slides along the ground (see review by Iverson, 1997). Traditional *post-hoc* analyses

of runout efficiency for such gravity-driven flows balance the gravitational potential energy of the moved mass before flow begins (mass × gravity × height, H) to the work done by the flow (mass × gravity × flow length, L × flow resistance (coefficient of friction), R_f); then $R_f = H/L$ and its reciprocal, efficiency, is $1/R_f = L/H$ (Hayashi and Self, 1992; Iverson 1997). Strictly speaking, this work-energy balance treats the flow as a point mass, and thus applies to the system's center of mass (Erismann and Abele, 2001). In practice, it is common to use the deposits' distal extents of the highest part on the hill where it started (maximum potential energy) to the furthest point of where it stopped (maximum work done by the deposit). This "distal extents method" has greater geological relevance and is also easier to measure. The analog to this in ejecta geology is to measure the distance traveled by a parcel of ejecta from where it hits the ground to where it stops sliding, giving L, and comparing it to the maximum kinetic energy achieved by the curtain, which occurs just before the curtain strikes the ground. This distal extents method is the approach we will take in the lab experiments.

We apply this concept of runout efficiency from a work-energy balance for flowing ejecta deposits (Barnouin-Jha and Buczkowski, 2007) but consider the ejecta's kinetic rather than potential energy. We use the mass and velocity scaling relations (Holsapple, 1993) that provide reasonable first order models of ejecta mass and velocity distributions (e.g., Housen et al., 1983; Wada, et al., 2006; Yamamoto et al., 2009, Richardson, 2011). We ignore known limitations of crater scaling rules for ejecta modeling that only break down after 90% of the transient crater width is achieved (Yamamoto et al., 2009; Richardson, 2011), but only influence a small percentage of the total ejecta volume (Austin et al., 1980). This allows us to derive an expression for ejecta

kinetic energy *KE* (of the familiar and general form $KE = \frac{1}{2}mv^2$) just prior to deposition as

$$KE = \frac{1}{2}\int_{R_b}^{R}\left[c\sqrt{Rg}\left(\frac{x}{R_t}\right)^{-\frac{1}{\mu}}\right]^2 \frac{3M_e}{R^3}x^2 dx \qquad \text{(Eq. 8)}$$

$$= \frac{3c^2 M_e Rg}{2\left(3-\frac{2}{\mu}\right)}\left[1-\left(\frac{R_b}{R}\right)^{3-\frac{2}{\mu}}\right]. \qquad \text{(Eq. 9)}$$

When this is ratioed with the work done by the flowing ejecta, the mass and gravity terms cancel and we arrive at an analogous runout efficiency $1/R_f$ of

$$\frac{1}{R_f} = \frac{2L\left(3-\frac{2}{\mu}\right)}{3c^2 Re}\left[1-\left(\frac{R_b}{R}\right)^{3-\frac{2}{\mu}}\right]^{-1}, \qquad \text{(Eq. 10)}$$

where the definitions and values (if applicable) of the variables are given in Table C1. Using the ejecta's kinetic energy in Equation 8 assumes its originating crater was gravity- and not strength-controlled, justified since most planetary craters with visible ejecta typically occur when the effects of gravity are more significant than target strength.

The ratio of the kinetic energy lost by ejecta at impact and just prior to sliding is given by *e* (in Equation 10) and requires constraints from laboratory measurements; Barnouin-Jha and Buczkowski (2007) suggested representative values for *e* of 0.01 and 0.03. Using *e* assumes that some fixed fraction of the initial kinetic energy of the in-flight ejecta curtain is lost to interactions with the surface. In practice, we determined *e* by taking the ratio between *KE* of the ejecta as it began to slide on the target to its *KE* just before landing: $e = KE_{\text{slide}}/KE_{\text{curtain}}$. By constraining *e* in the lab, we can apply this value to interpreting the geology of natural ejecta deposits.

4.3. Laboratory Investigation: Experimental Apparatus

Our novel ejecta simulating catapult (Figure 4.2) at the Johns Hopkins University Applied Physics Laboratory (APL) produces a portion of an impact crater's ejecta curtain, whose flight and subsequent deposition can be assessed in detail. The simulated ejecta curtain is an outward-sweeping semi-conical "wall" of gravel ejecta simulant inclined about 45˚ to the ground, and is composed of individual grains on ballistic trajectories. The catapult is a roughly 1 m^2 steel plate, on which we have placed sand paper to limit gravel slip during launch. The steel plate pivots on a stiffly-sprung fulcrum and simulates a wedge of a conical ejecta curtain from an imaginary impact crater by launching any desired ejecta simulant. The catapult is capable of launching a wide range of mass, but we focus here on gravel ejecta simulant loads that range from 6 to 10 kg placed along the center of the catapult in a 20-40 cm wide, ~40 cm high, and 4-6 cm thick curved trapezoidal prism (see arrangement in Figure 4.2). Varying these fairly small masses did not noticeably affect the catapult's launch speed nor the speed of the ejecta.

To characterize the velocity distribution of the ejecta generated by the catapult, we used a Miro-4 Phantom® high speed video camera. The Phantom camera is capable of recording movies at 1200 frames per second (fps) that allows measuring the velocity of the ejecta gravel in flight and during emplacement on our various target surfaces. Exporting the individual frames as an image sequence, we mapped the images from pixel space to physical space using a calibration image of a grid in the camera's focal plane (identical to the method of Barnouin-Jha et al, 2007). This calibration also corrected for lens distortion (see Barnouin-Jha et al., 2007), essentially orthorectifying the image. Measuring the velocity components of grains then simply involved visually identifying

the same grains between subsequent frames and dividing the displacement by the time interval. We achieved this using two computer-based approaches (manual and semi-automatic) that were consistent with each other. The flight of the curtain grains (which are largely non-interacting) is dominated by simple Newtonian ballistics; accordingly, measuring the speed of the ejecta at the instant of impact is highly repeatable and consistent between experiments. This consistency allowed the discovery of an empirical model of catapult ejecta emplacement velocity as a function of distance from the catapult (Appendix) for a fixed 40˚ pull back angle of the catapult.

In addition to characterizing the curtain's velocity distribution, we also needed to characterize its mass distribution. Mass is an input to erosive efficiency among other parameters. Using ejecta catchment buckets arranged downrange (Figure 4.2b), we weighed the gravel in each bucket after shots using 6-10 kg of ejecta. Dividing the mass in each bucket by the surface area of the bucket opening gave the mass per unit area m_a. which allowed discovery of an empirical model of catapult ejecta emplacement mass as a function of distance from the catapult (Figure C1, Appendix C). A constant 40˚ pull-back angle for the catapult was used, and altering the gravel mass on the catapult did not change the model except by extending its applicability downrange.

The relevant length scale for ejecta deposition is the width, w (r in Eq. 1). We measured this from side-looking movies of ejecta deposition in images that showed the curtain depositing itself on gravel or plywood. The curtain's curvature and the dynamic deposit contributed to uncertainty in the width measurement and the associated empirical model (Figure C2).

4.3.1. Experiments Performed

Our experiments had two broad objectives: 1) To demonstrate dynamic similarity between catapult ejecta and larger-scale natural ejecta and then leveraging that similarity to 2) constrain the ejecta runout and ejecta erosive efficiency, validate scaling rules, and investigate qualitatively the geologic phenomena of ejecta emplacement. We do this by undertaking the following suite of experiments (Figure 4.2 and Table 4.1). Every experiment involved 6, 8, or 10 kg of either plain or colored gravel as an ejecta simulant. We winched the catapult back to 40˚ from the vertical. We placed fins on either side of the catapult's centerline to correspond to the size of the deposition target area.

We used two granular targets: pea gravel and a finer clay gravel. The well-sorted pea gravel is coarse (mean grain size of 5.1 ± 0.3 mm; Table C2; Figure 4.5). The finer clay (1-3 mm; Table C2, Figure 4.6) was used to so that the ejecta deposit would be thick compared to the size of the target grains (i.e., thicker than a few grain diameters). As discussed below, the non-granular targets were plywood or catchment buckets.

We used three types of ejecta: 1) well-sorted, coarse, plain pea gravel, which is the same as that used in the targets; 2) well-sorted, coarse, colored aquarium gravel deposited onto the plain gravel; and 3) and fine, colored, clay gravel which we used as both an ejecta and a target. The pea gravel is coarse enough that is not appreciably affected by air resistance at our laboratory speeds under 7 m/s. The colored aquarium gravel allowed distinguishing between the ejecta deposits and the pre-existing plain gravel targets, and permitted assessing mixing between the colored ejecta and the pea gravel. The use of several colored layers of aquarium gravel in the ejecta curtain in one experiment (160701 (year month day format)) allowed tracking different heights along

the curtain during flight and deposition. For this layered color experiment, we placed orange gravel at the base of the catapult, followed by blue, green, red, and cyan gravel at the top (Figures 4.5 and 4.6). The use of the red clay ejecta gravel and blue clay target gravel in the final two experiments (160810 and 161123) also permitted investigating mixing between the ejecta and target in the situation where the grain sizes are significantly smaller than the thickness of the deposits. These finer clay gravels, however, possess grain sizes still coarse enough that air resistance effects were minimized. A discussion of air resistance effects is in Appendix C.

4.3.1.1. Ejecta on Plywood

Our initial experiments focused on depositing 6, 8, and 10 kg of coarse, plain pea gravel onto a 2.75 m-long plywood stage downrange of the catapult. The plywood target is a hard, smooth, non-erodible surface representing an end-member case analogous to ejecta emplacement on a hard surface (possibly cooled lava or impact melt surfaces lacking regolith) where the ejecta momentum is insufficient to erode a pre-existing surface. From the side-looking Phantom camera, we measured the change in the ejecta velocity during curtain deposition. Measuring the footprint width w of the curtain was also possible from these videos. Experiments with only 6 kg of ejecta gravel were more amenable to measuring L because the curtain was short enough to not land or slide beyond the length of the plywood stage.

4.3.1.2. Ejecta in Buckets

For several experiments (Table 4.1), we replaced the plywood stage with a double-wide row of buckets extending downrange (Figure 4.2b). Early experiments (prior to experiment 160207) used dividers in the 3-foot long target box with buckets further downrange. The last mass experiment (160207) used all buckets in a 2 × 9 arrangement. The catchment buckets allow measurement of the ejecta mass distribution before sliding occurred by simply weighing the coarse gravel in each bucket after a catapult shot (the buckets are thus not supposed to represent any geologic target) in a similar manner as Wünnemann et al. (2016). Dividing by the area of the bucket openings yielded m_a for the experiments.

4.3.1.3. Ejecta on Gravel

We removed the buckets and replaced them with a clear-sided target box filled with coarse or fine gravel. The gravel target, which matched the ejecta simulant in composition and grain size, is the most geologically representative of the targets that we used. It allowed measurement of erosive efficiency and other forms of regolith mobilization by ejecta emplacement. An early experiment (160303) used a 3-foot long, 2.5 inch deep target box and later experiments (160701, 160810, and 161123) used a 6-foot long, 4 inch deep target box, both of which were 18 inches wide. Prior to each experiment we leveled the gravel in the box (the "regolith") to be flush with the top of the box.

These experiments used the same side placement of the high speed Phantom camera but also used handheld video cameras above the catapult looking down on the

ejecta curtain to acquire additional data. Having multiple perspectives on the same event allowed better tracking of boundaries during curtain flight and ejecta runout. The handheld cameras recorded video between 120-220 fps compared to the 1200 fps Phantom side-looking camera.

Following each experiment, we photographed the ejecta deposit and the erosional contact between the ejecta and regolith through the clear walls of the target box. Photogrammetric control of these photographs using calibration grids in the image allowed translation of pixel positions to physical locations. This photography allowed measuring the depth of erosion and the thickness of deposition. It also permitted counting ejecta grains penetrating below the erosional contact or regolith grains exhumed atop the ejecta.

4.3.1.4. Measuring e, L, M, v_c, and $1/R_f$

We measure *e* by finding the total kinetic energy of the sliding ejecta and ratio it to the kinetic energy of the about-to-land ejecta: $v^2_{\text{sliding ejecta}}/v^2_{\text{curtain ejecta}}$ (the ½ and masses cancel out). We use the velocity measurements obtained from the Phantom high speed camera. We assume that the change in ejecta velocity is the dominate cause of the change in the ejecta's kinetic energy, and so do not include the target mass excavated by the ejecta when it flows over erodible surfaces. Including the target's eroded mass in the calculation would over-estimate the energy remaining in the ejecta to do work on the target.

To measure *L* for the experiments using the plywood or gravel targets, we track the distance between where the top of the ejecta curtain first lands to where it stops

flowing (Table 4.2). This first landing point of the curtain's top (Figure 4.7) is defined by the bucket experiments where the mass profile of the curtain precipitously drops off beyond a certain catapult distance, called the mass rollover. The furthest runout extent of the bulk of the ejecta is the distance where 50% of the underlying surface is visible "through" the ejecta deposit as defined by pixel values in photographs. We call this measurement approach the "distal extents method." From an energy perspective, this is analogous to how landslide runouts are measured on Earth: from the top of the detachment scarp where it has the greatest potential energy to the furthest extent of the runout where it did the maximum work. For ejecta, the base of the curtain an infinitesimal amount of time before it strikes is where it has the most kinetic energy. Just as for landslides, the distal extent is where it did the most work. Thus from the perspective of an energy-work balance, landslides and ejecta runout are treated similarly. (In the multi-colored coarse gravel experiment (160701), we rather tracked the landing and stopping distances of red-green color boundary on the plain gravel target surface as opposed to using the distance of the mass rollover.)

To determine the distal extent of the gravel ejecta in photographs, we found the catapult distance where half the pixels were from "ejecta" gravel and the other half were the substrate (whether plywood or "regolith" gravel). In the case of the multi-colored coarse gravel (experiment 160701), we found the catapult distance where half the ejecta grains were green (more proximal) and half the ejecta grains were red (more distal). Thus, we measured L from where the top of the representative curtain struck the ground (from the mass versus distance plot, Figure 4.7) to where only 50% ejecta cover remained. However, using the system's center of mass (COM) would be more physically

correct (Erismann and Abele, 2001) though the distal extents method is more geologically relevant, more readily measureable, and has more historical precedence for forming a basis of comparison (Hayashi and Self, 1992; Iverson, 1997).

All our measurements of L suffered from some uncertainty primarily due to the diffuse nature of the boundary describing the edge of the flow and the stochastic nature of granular systems. On average, this uncertainty measured ± 21% (Table 4.2).

Experiments of coarse colored gravel onto coarse plain gravel (experiments 160303 and 160701) and fine red clay gravel onto fine blue clay gravel (experiments 160810 and 161123) allowed estimating the displaced target mass M. The fine grain size (<3 mm; Table C2) allowed more confident topography measurements because the grain sizes were small compared to the ejecta deposit thickness. For both coarse and fine grained experiments, we measured the depth to the top of the target ("regolith") layer below the top of the target box. We mapped the erosional profile from photogrammetrically controlled images taken through the clear side of the target box (Figures 4.6, C3, C4). Centimeter-ruled grids visible in the images allowed translation of pixel position to physical location (see Appendix C).

Similar to mapping geomorphology from pixel space to physical space, we also measured the grains' velocities by exporting frames from the Phantom camera, tracking grains in the images, and converting their pixel speed (pixels/frame) to physical space (m/s). This approach is detailed in Appendix C and illustrated in Figure C5.

Having measured the dynamics and morphology in lab space, we then scaled the results to larger, natural regimes using the π_2 scaling arguments presented in Section 2. The approach we follow is similar to past efforts to investigate clustered impacts

(Holsapple and Schmidt, 1982; Schultz and Gault, 1985) where we calculate π_2 based on the ejecta's velocity v_c, Earth's gravity (g = 9.8 m/s^2), and the curtain's footprint width, w. We observed the footprint width in the videos to widen with distance downrange and we measured the trend. The empirical linear relationships for 6 and 10 kg gravel masses are given in Figure C2.

Finally, to apply runout efficiency $1/R_f$ to catapult gravel, we compared the specific KE ($\frac{1}{2}mv^2$) of the flowing ejecta to the work it did on the target. We calculate the work, W, by the flowing ejecta on the target as

$W = Fd$ (force times distance)

$= NR_fL$ (normal force times the coefficient of friction times runout distance)

$= mgR_fL$ (mass times gravity times the coefficient of friction times runout distance).

Equating this work done on the target to the maximum kinetic energy yields the runout efficiency $1/R_f$:

$\frac{1}{2}mv^2 = mgR_fL$

$1/R_f = 2gL/v^2$. (Eq. 11)

4.4. Science Results

Section 3 explains the experimental methodology we undertook. In this section, we present detailed qualitative results on the observed dynamics of ejecta emplacement and preliminary quantitative assessments of erosive efficiency and ejecta runout.

4.4.1. Dynamic Similarity: Matching Theoretical Ejecta Models to Experiments

To extend the laboratory results to planetary-scale crater ejecta, we show that the laboratory ejecta velocity-mass distribution possesses similar physical attributes to a natural ejecta curtain just prior to deposition. We captured the pre-deposition physical attributes of the ejecta in two ways: (1) by establishing the cratering conditions in which the catapult ejecta velocity and mass profiles match the profiles produced by a crater of a given radius on Earth (i.e. finding the size of the imaginary crater that could produce the lab ejecta's mass and velocity profiles); and (2) by rendering our velocity and width measurements dimensionless via π_2 that takes into account the ratio of gravity relative to the inertial properties of the ejecta.

The experimental measured ejecta mass per unit area m_a made with our catchment bins compare favorably with the ejecta model presented in Section 3.2 (Figures 4.7, C1). Larger masses extended the downrange distance of the deposits relative to smaller masses but otherwise gave the same m_a profile, which matched a true crater ejecta curtain. A best fit of the laboratory data for m_a was obtained with an ejecta model that assumes an imaginary terrestrial crater of R = 3 m. For the catapult to generate an identical ejecta m_a distribution to that for R = 3 m, the catapult must be presumed to sit 1.8 R (5.4 m) from the imaginary crater rim (Figure 4.8). Combining the offset of the catapult from the imaginary crater rim and the throw range of the catapult, we find that the catapult simulates ejecta deposits between 1.9 and 2.3 R (5.7-6.9 m) from the imaginary crater rim.

Unfortunately, the catapult experiments cannot match both m_a and v_c of a R = 3 m crater. In order for the velocity distribution of our ejecta model to equal the measured

ejecta velocity obtained with the catapult, we obtained a best fit using an imaginary crater with R = 6.0 m and a landing distance from the transient crater rim of 1.2 to 2.3 R (7.2-13.8 m) (Figure 4.9).

The inability to simultaneously match all the physical attributes of a process, in this case v_c and m_a of crater ejecta, is frequently an issue when using a scaled laboratory experiment such as the ejecta catapult. To circumvent this issue, we use the non-dimensional parameter π_2 and M/m of Equation 1 that allows assessing the inertial effects of both the velocity and a characteristic curtain length scale in π_2, and m_a effects in the erosive efficiency term M/m. By taking this approach, we find an imaginary crater with R = 1 m, with the catapult located 2.8R from the rim, best fits the observed data (Figure 4.10). While this is a small imaginary crater size compared to the velocity and mass craters estimated above, it is near the same size predicted from the relatively thin curtain: a ~0.13 m wide curtain footprint (Figure C2) implies a transient crater radius of ~0.43 m. These ejecta scales are significantly larger than anything that can be created in impact facilities such as the NASA Ames Vertical Gun Range; in these cases, the largest craters have radii of ~15 cm and ejecta curtains are at most ~5 cm thick.

Having established that the catapult gravel provides a meaningful simulation of crater ejecta prior to emplacement, we now turn our attention to the geological consequences of ejecta emplacement.

4.4.2 Qualitative Ejecta Curtain and Deposit Description

When viewed from the side (i.e. when the line of sight is perpendicular to the gravel's direction of travel), gravel launched from the catapult plate forms a well-defined

curtain. In flight, individual gravel grains have only a small component of velocity relative to each other and very little rotation. The small component of relative motion causes the curtain to slowly widen with time and distance, and because the top of the curtain spends more time aloft than the bottom, it experiences more widening. Like natural crater ejecta, the gravel curtain is inclined relative to the ground between 40-50˚. As the ejecta curtain sweeps and deposits itself laterally across the target surface, it leaves behind a highly mobile granular deposit. This dynamic ejecta deposit (which also incorporates eroded local material), has also been called a surge (Oberbeck, 1975). The deposit—whether emplaced on plywood or gravel target surfaces—initially takes on a wedge shape with the narrow, tapered end just trailing the curtain (Figure 4.3). The narrow portion just behind the deposition front is where the ejecta has transferred the vertical component of its velocity into the ground but is still near its maximum horizontal velocity and has not yet had time to bounce or begin tumbling. As grains begin to bounce and tumble, the flow's horizontal motion slows, and the wedge thickens towards the catapult or crater rim. The ejecta grains in the flow are re-acquiring a vertical velocity component, and the overall porosity of the deposit increases. As the ejecta grains continue to interact with each other and the target surface, the dynamic deposit thins and the forward velocity lessens. Finally, the individual ejecta grains come to a stop some distance downrange of their initial ground-contact points. At a real impact crater, we would expect the edge of the ejecta towards the rim to thicken steadily, partly due to rim uplift, which the catapult does not attempt to simulate. In erosion experiments (i.e. gravel-on-gravel), we noticed that more distal grains from the target box were energetically mobilized (~1.8 J/kg) by the impacting curtain and traveled downrange,

away from the catapult. These prior "regolith" (*in situ*, non-ejecta) grains travel along paths very reminiscent of what is observed during aeolian saltation (Figure 4.11).

In addition to the runout of ejecta, the target regolith can be significantly eroded and gardened ("bulldozed") by the ejecta curtain and dynamic deposit. The profiles in Figure 4.6 and C3 show that passage of the ejecta curtain and its dynamic deposit erodes the pre-impact surface heterogeneously. In the experiment, where colored gravel was used to assess the degree of mixing, we noticed occasional instances of ejecta burying or embedding itself into the target regolith (Figure 4.6, Figure C3). These experiments also indicate that regolith can be partly exhumed and incorporated into the ejecta facies along the entire deposit. Video stills captured before and after deposition (experiment 160810) show deep regolith grains displaced in the direction of ejecta deposition in a shearing motion with offsets of 1-4 mm. This shearing distance is the equivalent of 1-4 $\times 10^{-3}$ crater radii for a 1 meter π_2 crater, where crater size scaling is discussed in Section 3.3. The displacement gradient reduces with depth but seems to affect grains down to at least 5 cm (0.05 π_2 crater radii) in the 10 cm deep target box. Experiments with coarser grains (160303 and 160701) show that occasional regolith grains can be moved above the pre-impact surface suggesting that regolith was exhumed and placed on top of the ejecta deposit by the ejecta flow.

The most distal portions of the ejecta deposit lightly mantle the regolith but do not erode. For the fine gravel experiments 160810 (8 kg ejecta) and 161123 (7 kg ejecta), the erosion halts at a distance from the catapult of 1.33 m and 1.29 m, respectively. However, ejecta mantling of the surface extends further, from 1.25-1.51 m and 1.36-1.42 m, respectively.

4.4.3. Toward Scaling: Erosive Efficiency

From the two fine gravel experiments (160810 and 161123) we showed that the falling ejecta can erode target material that is on average 3.4% of its mass, and can vary from 2-11% of its mass as a function of distance (Figure 4.12, *top, middle*). Both depth of regolith erosion and the thickness of the ejecta deposit are thickest closer to the catapult and both thin with distance (Figure C4). Distal ejecta from the catapult lands faster than the proximal ejecta but is less massive and more porous owing to the gradient in the ejecta velocity and resulting spreading during flight. As such, the distal ejecta can laterally mobilize ("saltate") regolith, whereas closer to the catapult vertical "bulldozing" dominates. Other than a general thinning with distance, the erosion and deposition profiles are wavy and heterogeneous.

The erosive efficiency falls rapidly with increasing π_2 (Figure 4.12, *middle*), which is as we might predict: slow ejecta (high π_2) near a crater rim will not erode regolith as efficiently as fast ejecta far from the rim. Indeed, this fast (low π_2) distal regime is where ejecta emplacement begins to mimic primary cratering with high erosive (or cratering) efficiency. While M/m falls with increasing π_2 (slower ejecta), it still highly variable at any given point along the ejecta deposit.

The highly variable erosive efficiency profile is due to the stochastic nature of coarse and dispersed granular systems. Over short distances, particle spin, surface roughness (Gutt, 1989), angularity, variable grain size, and variable particle packing contribute toward unpredictable erosion. The in-flight grains have various dispersions due to small differences in relative flight velocity and strike the surface with

unpredictable grain orientations. Because of these contributions to stochasticity, and because the catapult only simulates a short range from a natural crater near the continuous ejecta deposit's edge, we combined the results from both experiments (160810 and 161123) into two data points for comparing each experiment to other single and clustered projectile impact experiments. We did this by computing a weighted average of π_2 relative to M/m for both experiments and the ratio of the sum of the displaced regolith mass ΣM to the sum of all the ejecta mass Σm. Thus, from 3-4 transient crater radii from the rim, regolith erosion amounts to 2.4% and 4.5% of the ejecta's mass for the two experiments, respectively (160810 and 161123).

These results indicate that ejecta is not particularly erosive relative to these more erosive cratering processes, which tend to displace several projectile masses of target material (e.g., Holsapple and Schmidt, 1982; Schultz and Gault, 1985). Our average ejecta erosive efficiency data fall well below the region expected from the power law prediction for clustered impacts and individual projectile impacts (Figure 4.12, *bottom*).

4.4.4. Kinetic Energy Partition e

The total specific *KE* of the ejecta in the curtain before landing, from 0.4 to 1.5 m from the catapult, is 16.8 ± 0.9 J/kg . In the case of the plywood interaction, the specific *KE* of the flowing ejecta is 6.0 ± 2.6 J/kg, giving $e_{\text{plywood}} = 0.36 \pm 0.18$. For deposition onto coarse gravel, we find a lower specific flow energy of 4.0 ± 1.2 J/kg and $e_{\text{gravel}} = 0.24 \pm 0.08$. Our measured values of *e* are comparable to the upper range of 0.3 proposed by Barnouin-Jha & Buczkowski (2007) which they preferred based on assessments of clustered impact data; their value of 0.01 based on an energy balance assessment

considering ejecta as single projectiles is clearly not correct. This number also matches what Wada and Barnouin-Jha (2006) saw in numerical discrete element simulations of the ejecta deposition process.

4.4.5. Ejecta Runout L and Efficiency $1/R_f$

Table 4.2 shows the results for L and $1/R_f$ for different experimental setups. In all cases, the ejecta deposits slide several tens of percent of the initial landing distance or more. This thins the ejecta deposit substantially from its initial pre-sliding configuration.

In comparing runout efficiency with ejecta volume, we discovered a trend consistent with small volume landslides, where both wet and dry debris flow have runout efficiencies of ~3.5 or less. Future ejecta and debris flow studies should leverage this commonality between lab ejecta and natural granular flow.

4.5. Discussion

The catapult demonstrates dynamic similarity to a natural ejecta curtain. Therefore, we can use the measurements of e and L to give at least loose constraints on what these values are in nature. Furthermore, our qualitative descriptions of the deposition and runout processes hint at the transport histories of ejecta and regolith parcels, in turn providing a context for interpretation of remote sensing datasets and returned samples, such as petrologic interpretation. From the whole of our qualitative observations, we present a schematic in Figure 4.13 illustrating ejecta emplacement flow, erosion, implantation, and saltation of regolith. Below, we discuss these further.

4.5.1. Qualitative Observations

The importance of ejecta flow during emplacement is perhaps the most overarching result in these early catapult experiments. A surprising consequence of our lab ejecta emplacement was the energetically mobilized bulldozed, sheared, and "saltated" regolith grains, which illustrates that ejecta can ballistically move large amounts of near-surface regolith further from the crater and affect regolith positions at depth. Ejecta saltation could perhaps explain ejecta "dunes" or crater concentric ridges (Oberbeck et al., 1975; Atwood-Stone et al., 2016) that are between ~1-6 crater radii from many lunar and Mercurian craters, perhaps acting in concert with the interacting ejecta mechanism proposed by Oberbeck et al. (1975).

Even if the ejecta dynamics is not the granular motion responsible for the dunes and concentric ridges, it does indicate instance of lateral gardening of the surficial regolith. Additionally, we observe erosional topography (Figures C3, C4) and shearing of the deep regolith simulant. Shearing occurs at depths several times the thickness of the ejecta deposit. Observations of erosion and shearing may be analogous to observations of buckling, detachment faulting, and furrows below Ries Crater's ejecta in Germany (Kenkmann and Ivanov, 2006; Kenkmann and Schönian, 2006). As a thought experiment, if one considers a hypothetical patch of ground on the Moon, subsequent ejecta curtains coming from multiple craters from different directions could shear layers at depth in different directions, leading to diffuse nonconformities in the ejecta stratigraphy. Additionally, up to ~5% of the ejecta's mass could be eroded from the substrate regolith. These heterogeneities in deposits and erosional contacts should lead to extreme caution in interpreting sample provenance and regolith stratigraphy.

The wavy nature of the erosion surface and ejecta deposit has implications for studying stratigraphy through the "window" of small craters superposing ejecta facies. Some small craters sitting atop a continuous ejecta facies from a large, dominant crater may only excavate ejecta from the dominant crater. Other small craters, sitting at approximately the same radial distance on the ejecta facies, may excavate the pre-impact regolith if these small craters form on a thin ejecta patch. These possibilities should be kept in mind when stratigraphers interpret ejecta geology.

4.5.2. Quantitative Measurements

M/m of the ejecta compared to that for single or clustered hypervelocity impacts (Holsapple and Schmidt, 1982; Schultz and Gault, 1985) is much less efficient at erosion. Our data also plot below the power law for the single and clustered projectile data. We suggest this is because low speed (high π_2) clustered impactors simply involve different physics than for hypervelocity impacts which can be approximated as point sources (Gault et al., 1968; Holsapple and Schmidt, 1982; Holsapple, 1993). The slow, granular nature of ejecta emplacement clearly does not have a point source solution due to multiple slow grain-grain interactions in which grain shape, surface texture, angularity, and spin are all important (Gutt, 1989) and contribute to unpredictable erosion. Interestingly, we note scatter and deviation from the power law in the slowest clustered impact speeds used by Schultz and Gault (1985) (Figure 4.12). This deviation could define a different power law relationship along with our slower, granular data.

Accordingly, new suites of experiments which more fully explore the range of M/m and π_2 values are needed, such as experiments with different speeds, thinner or

thicker ejecta curtains, and/or different gravities. New experiments to extend the π_2 range would need modification of the current catapult but could produce the data needed to identify a more robust scaling relationship and to test the current scaling relations. Already our data point to a regolith mass equivalent to ~2-5% of the ejecta mass becoming eroded, underscoring the erosive nature of ejecta deposition. Future experiments at lower π_2 values (corresponding to lower surface gravities, thinner curtains, and/or faster velocities) may have even higher erosive values.

In addition to significant erosion, high runout efficiencies between $1/R_f$ = ~1-2 (Figure 4.14) underscore the mobility of primary ejecta during its emplacement. Deep shearing, saltation of regolith, and the bulldozing of ~2-5% of the local regolith all contribute to vertical mixing. This critically emphasizes the complex dynamic transport histories that must be considered when tracing anomalous geochemical facies on the Moon (Li and Mustard, 2000; 2003; 2005) back to their originating lithologies or interpreting petrologic samples (e.g. Schmitt et al., 2017).

The remaining energy in the dynamic ejecta deposit just after striking the ground is what allows significant erosion and runout. The values for *e* of around 24-36% underscore the significant amount of kinetic energy available to thin the ejecta deposit via runout and to erode the substrate. This energy could be important on planets like Mars where small amounts of volatiles could facilitate extremely long ejecta runout lengths, paralleling water's role in enhancing debris flow runouts on Earth (Iverson, 1997). Evidence for efficient runout without water is clearly shown in Figure 4.14, where the lab results compare similarly to natural wet and dry terrestrial landslides with volumes up to 1 km^3 (12 decades more voluminous than in our laboratory experiments). If planetary and

lab ejecta regimes are indeed similar to each other, we also note that a high fraction of the ejecta's original kinetic energy (approximately 1-*e*, not accounting for heating) is lost to work done on cratering, displacing (e.g, shearing, exhuming), and eroding the pre-impact surface. These lead to the possibility of complex geologic structures below the ejecta-regolith interface and may explain the formation of such structures as sheared detachment faults visible at Ries Crater in Germany (Kenkmann and Ivanov, 2006; Kenkmann and Schönian, 2006).

Applying laboratory ejecta results extends to considerations of stratigraphic relations and related geology. Stratigraphic studies (e.g., Rice and Warner, 2016) have made assumptions about original ejecta thickness based on a simple thickness model (McGetchin et al., 1973) which does not account for post-depositional ejecta flow, erosion, and basal regolith shear. This model assumes a smooth thickness decay away from the crater with a power law slope around -3 for the Moon (McGetchin et al, 1973; Sharpton, 2014). We measured natural variation in a stochastic granular process and a high degree of runout which "stretched" its in-flight length by up to double (Table 4.2). Heterogeneous emplacement and long runout undermines the confidence in assuming a smooth power law thickness decay when considering ejecta stratigraphy and ejecta provenance depth from within the crater. As such, we urge caution when applying ejecta thickness models for constraining stratigraphy.

4.5.3. Caveats

A potential caveat in applying the current suite of catapult experiments to natural ejecta facies is with regard to curtain footprint. Cratering experiments show (Cintala et

al., 1999; Barnouin-Jha et al., 2007) and theory suggests (Maxwell, 1977; Richardson, 2011) that ejecta footprints shrink with increasing crater distance whereas ours expands slightly. However, these impact experiments had very small ejecta volumes and are only meant to replicate a small portion of a natural curtain. Even though we loaded gravel on the catapult such that it thinned slightly moving up the plate (visible in Figure 4.5), differential particle trajectories in flight widened the curtain such that the footprint widened with increasing catapult distance. While this effect was not predicted from theory or from cratering experiments, it may provide insight into possible curtain widening in natural cratering events due to a wide range of particle velocities in the fastest portions of the curtain.

Absent in our experiments are any considerations of volatiles, including impact melt, which can become emplaced within several crater radii (e.g., Ghent et al., 2016) and is common on the Moon and Mercury (Denevi et al., 2012; Denevi et al., 2013). Molten ejecta could potentially mobilize with lower shear stresses and easily incorporate granular regolith in ejecta facies. It may enhance runout as well. Furthermore, in nature, energy goes into fracturing rock not accounted for by our experiments, and this energy sink could reduce natural ejecta runout.

4.5.4. Future Work and Predictions for Planetary Surface Exploration

Future catapult experiments should use substantially thicker ejecta curtains, achievable by lengthening the catapult's walls. Experiments at faster speeds (partly achieved with steeper pull-back angles) will expand the range of investigation, especially π_2 values, that is possible with the catapult. Investigating the emplacement and runout of

coarse ejecta simulant on a finer-grained target would aid in understanding extreme near-rim ejecta emplacement. Angling the target box may aid in understanding emplacement effects on slopes, and adding water could reveal the role of volatiles in runout.

Many of the results from the catapult experiments can serve as predictions for further studies on natural planetary ejecta facies. We predict seismic, drilling, mapping crater wall exposures, geochemical and mineral identification, and other geophysical investigations on the Moon and elsewhere will reveal

1. Uneven erosional profiles beneath proximal ejecta deposits;
2. Ejecta blocks embedded beneath the erosional contact;
3. Detachment faults beneath ejecta;
4. Regolith blocks transported away from the crater;
5. Evidence for regolith shear beneath ejecta deposits; and
6. Radial ejecta facies thickness profiles that deviate substantially from the -3 power law slope and are highly stochastic.

Understanding the range of stochastic transport histories possible for rock fragments or parcels of regolith or will better allow interpretation of petrologic and provenance analyses.

Finally, we apply these predictions to a brief case study of the simple crater Giordano Bruno on the Moon (D = 22 km, R = 11 km). The catapult simulates an area of ejecta deposition ~33-44 km from the rim. The ejecta would be emplaced as a 2.8 km thick wall of debris (including pore space) striking the ground at ~270-380 m/s. Before sliding, the ejecta 33 km from the rim would be 33 m thick and would thin substantially after sliding for over 23 km from the impact point. The ejecta facies' base would be 1-2

m below the pre-impact surface due to erosion. Regolith down to 550 m would be sheared radially away from the crater 3-11 m.

4.6. Conclusions

We pioneered a novel method for studying ejecta emplacement dynamics using a catapult without having to produce the progenitor crater. This has diverse practical applications, including investigations of a number of ejecta emplacement conditions and the range of rock transport histories and geomorphologies possible on other cratered worlds. The JHUAPL ejecta emplacement catapult simulates the granular component of a portion of impact crater ejecta curtain that is dynamically similar to larger natural ejecta curtains. Our preliminary experiments begin to demonstrate vertical and lateral erosion, degrees of ejecta runout, and the subsurface geomorphology. Our observations of the dynamic ejecta deposit affirm models (Oberbeck, 1975) and observations (Chao, 1974; Chao, 1976; Kenkmann and Ivanov, 2006; Kenkmann and Schönian, 2006; Ghent et al., 2016) which invoke post-depositional ejecta emplacement flow: up to approximately 36% (e = 0.36) of the ejecta's original kinetic energy is still available for runout and erosion following ground impact, and this value could hold at natural size regimes. This substantial post-landing energy explains the ejecta's high erosive efficiency of M/m = ~2-5% and high runout efficiency of $1/R_f$ = 1-2, comparable to km^3-scale terrestrial debris flows. This contrasts sharply with the view often presented in the literature of a simple continuous ejecta "blanket" which remains where it landed (e.g., Housen et al., 1983), implying that all the ejecta's kinetic energy is immediately transferred to the ground. Rather than a simple blanket, the emplaced ejecta facies violently erodes the substrate,

launches *in situ* regolith parcels on ballistic trajectories, embeds itself within the regolith, exhumes regolith to sit atop the ejecta, and shears the subsurface. Accordingly, caution is warranted when estimating the volume of crater excavation based on volumes of ejecta facies, which we have shown to include *in situ* regolith. Ejecta runout cannot be ignored when considering ejecta thickness' stratigraphic and crater excavation relations. Accounting for ejecta runout may aid interpretation of ejecta provenance for lunar and planetary remote sensing datasets and samples.

Future experiments should build off this foundation to simulate specific Solar System craters or worlds as case studies. Also, future experiments should create a substantially thicker curtain. This will require minor modification of the existing catapult apparatus.

Figures

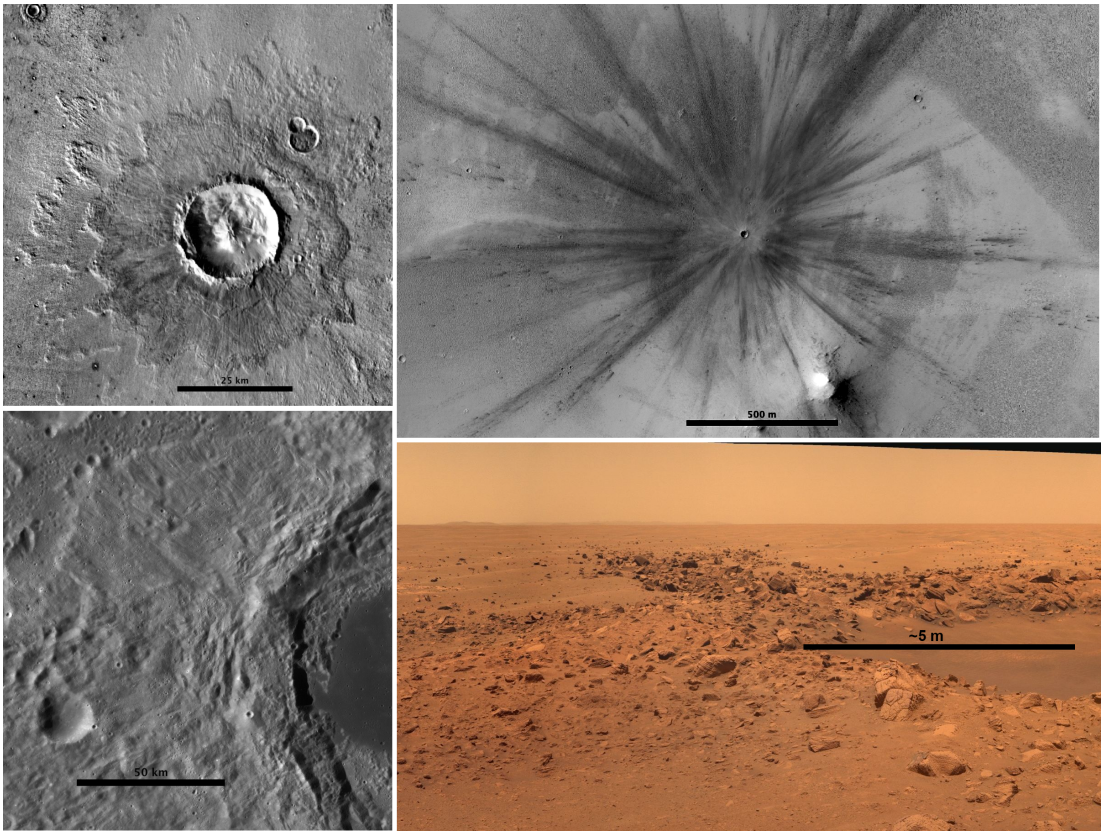

Figure 4.1. Examples of crater ejecta on planetary surfaces at a range of spatial scales. *Top left:* Bacolor Crater, Mars, features multi-layered ejecta with distal ramparts; 25 km scale bar; THEMIS image credit: NASA/ASU (33˚ N, 118.6˚E). *Top right:* A new impact crater with extensive dark ray ejecta on Mars. 500 m scale bar; HiRISE image ESP_034285_1835 (3.7˚N, 53.4˚E) credit: NASA/UA. *Bottom left:* Rare lunar lobate ejecta to the northwest of Tsiolkovsky Crater; 50 km scale bar; LROC WAC mosaic (18˚S, 124˚E), credit: NASA/GSFC. *Bottom right:* Proximal ejecta blocks from Concepción Crater (upper left of image) on Meridiani Planum, Mars, as imaged by the rover *Opportunity*; Credit: NASA/JPL/Cornell.

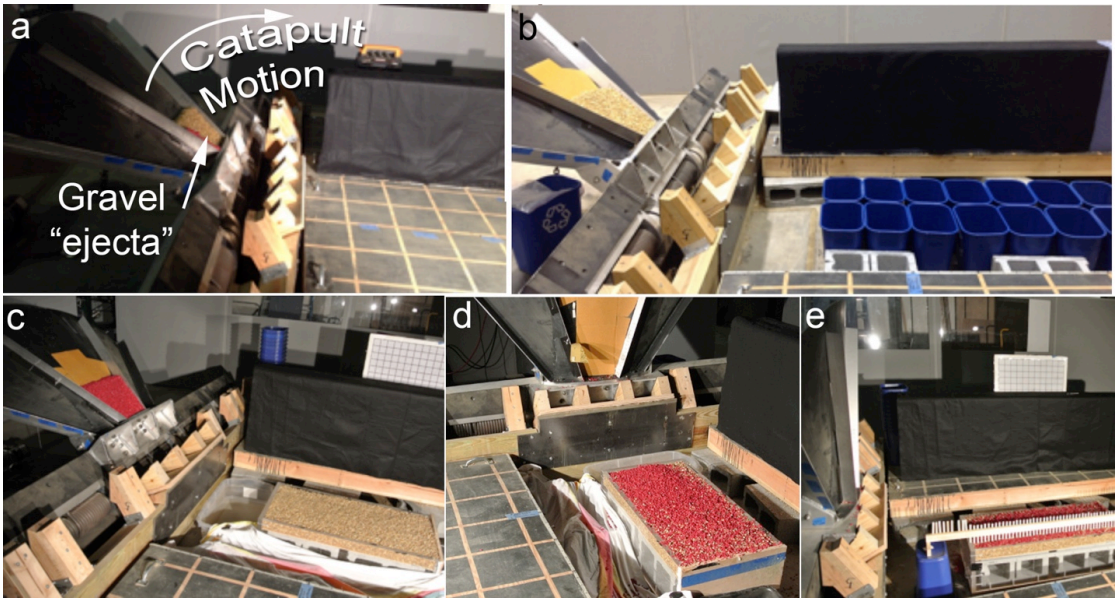

Figure 4.2. Overview of the ejecta catapult and the three main types of catapult ejecta experiments. (A) The catapult in the 40˚ pull-back cocked position loaded with pea gravel ejecta simulant prior to deposition on plywood. (B) Setup for deposition in buckets in order to measure the mass distribution of ejecta prior to surface flow. Dividing by the surface area of the buckets' opening yields the mass-per-unit-area of ejecta. (C) Colored pea gravel loaded on the catapult prior to emplacement on a 10 cm-thick gravel contained in a clear-sided target box. (D & E) The catapult in the fired position after depositing colored gravel onto the plain gravel target. A piece of the catapult's sand paper (used to fine-tune the curtain's velocity profile by reducing centrifugal effects during launch) has come loose in the photo.

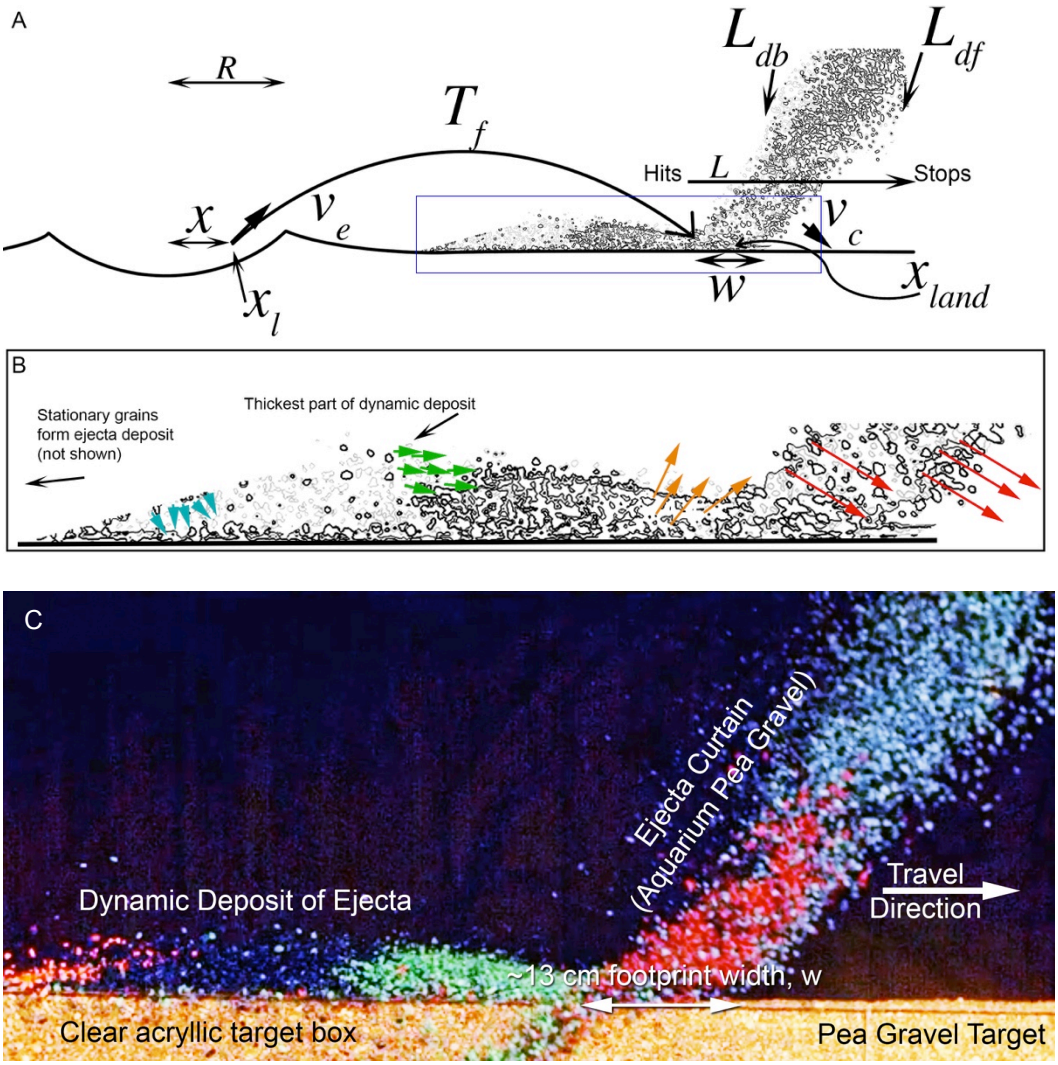

Figure 4.3. A) Schematic of some variables used in equations throughout the text to describe ejecta from an imaginary crater. See Table C1 for definitions. The area in B is boxed in blue in A. B) Schematic of ejecta deposition and the dynamic deposit. Red arrows (far right): ejecta curtain grains near their maximum velocity (kinetic energy). Orange arrows (middle right): grains transferred some energy into the target but rebound. Green arrows (middle left): grains reached their final height, giving the maximum porosity or thickness to the dynamic ejecta deposit. Cyan arrows (left): falling grains that will re-impact the surface, interact with each other stochastically, and come to a stop. C) Still frame from the high speed video showing the simulated ejecta curtain and the still-

mobile dynamic deposit. The footprint (width of the deposition front) is ~13 cm long. (From shot 160701.)

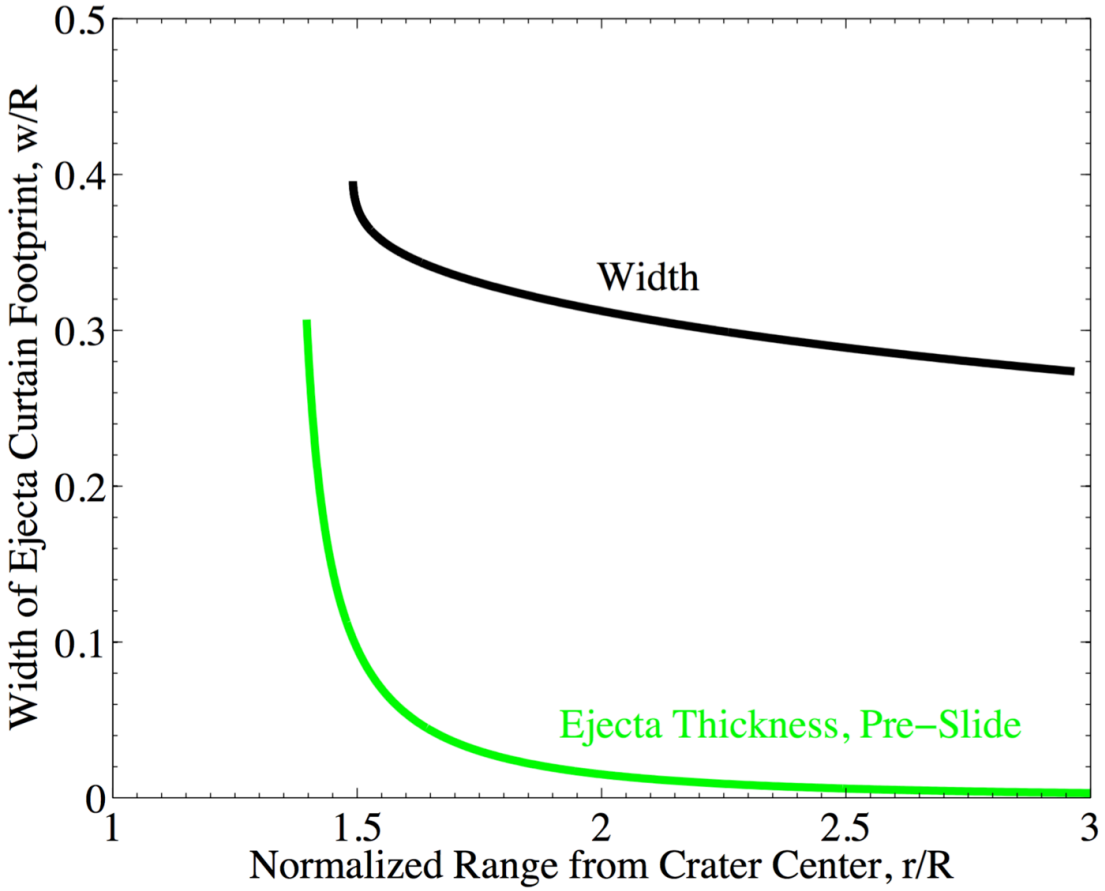

Figure 4.4. Ejecta curtain width at the time of impact (black) and the ejecta thickness (green), assuming no ejecta sliding. We use ~0.3 crater radii as the characteristic ejecta footprint width for the crater ranges we attempt to simulate. This agrees with plots from Richardson (2011) who calculated ejecta curtain widths from theory and impact experiments (Cintala et al., 1999).

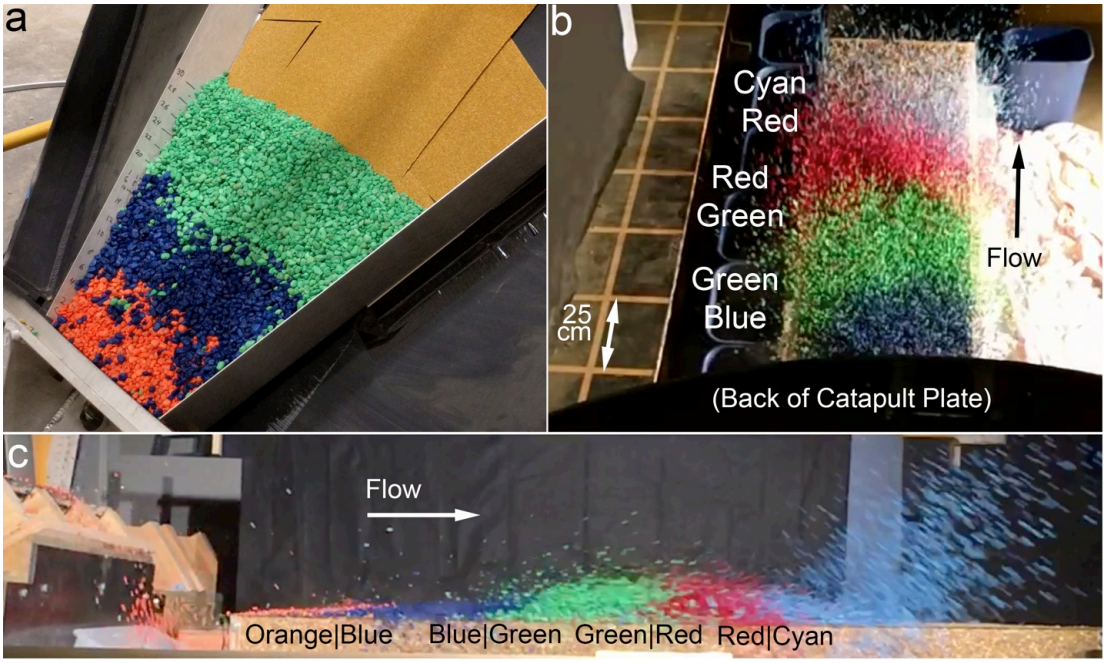

Figure 4.5. The color boundaries between layers of gravel allowed easy tracking of the ejecta runout and hence the runout efficiency. The red-green boundary was the most readily tracked as more distal portions flowed or landed beyond the edge of the clear-sided target box. A) Mid-way through loading colored gravel on the cocked catapult. B) Overhead view of ejecta deposition and runout. C) Side view of ejecta deposition and runout.

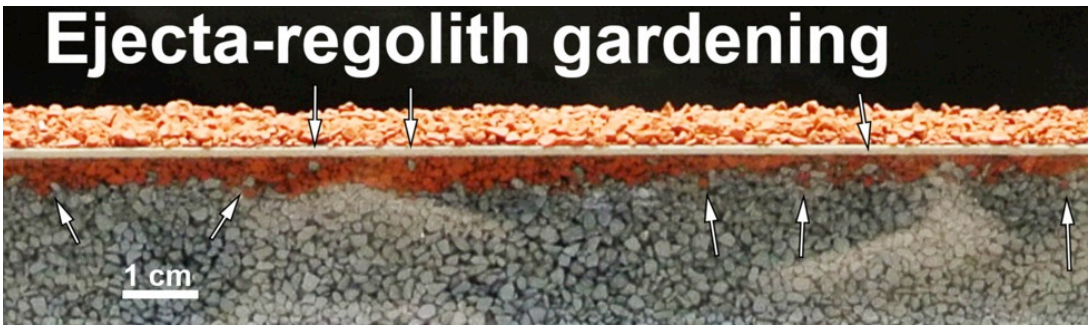

Figure 4.6. Examples of gardening in the fine gravel experiment. Red ejecta gardened and mixed heterogeneously with the blue regolith: some red ejecta buried itself beneath blue regolith and some blue regolith is correspondingly lifted above the red ejecta. The blue regolith was also sheared downrange down to about 5 cm depth. This section of the catchment box starts approximately 0.91 m from the catapult. From experiment 160810.

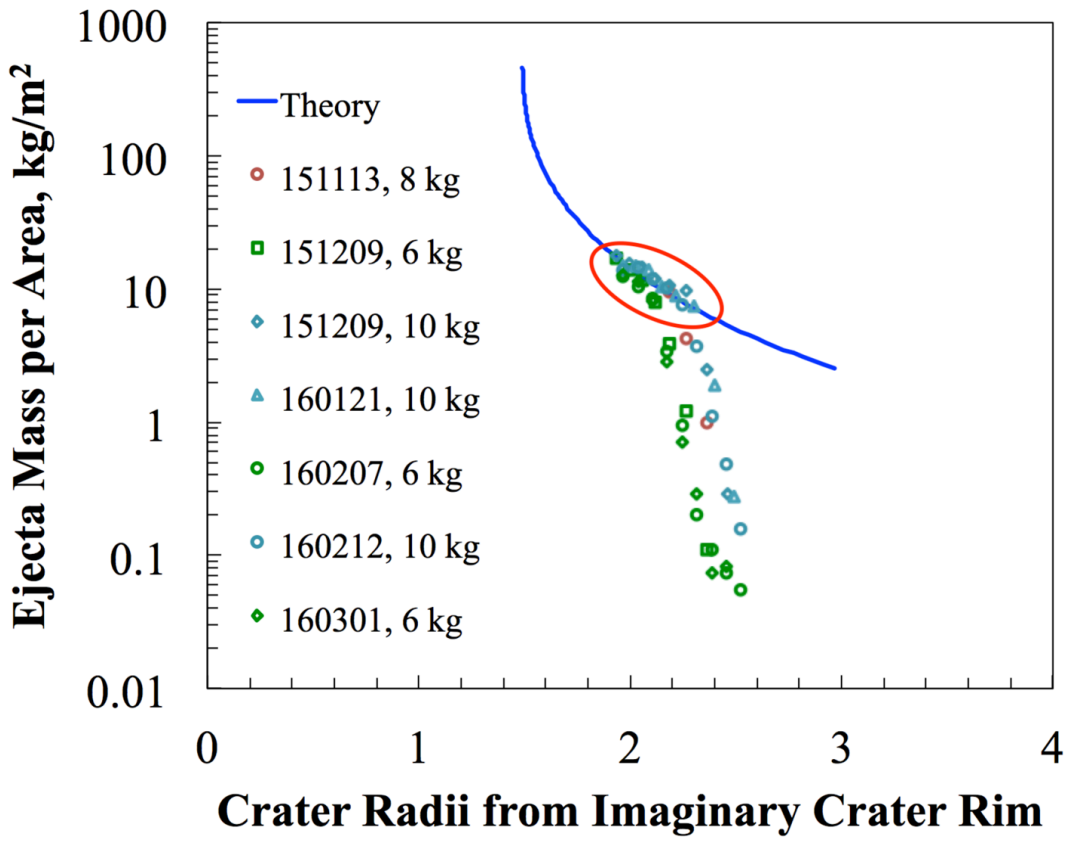

Figure 4.7. Mass per unit area of ejecta deposited before surface flow from a crater ejecta model (blue curve) and the ejecta (points) simulated in the laboratory. A best fit of the laboratory mass per unit area was obtained from the crater ejecta model when using a transient crater radius of 3 m, with the catapult located about 1.8*R* from the imaginary crater's rim and shows the catapult represents natural ejecta between 1.9-2.3*R*. The circled data points are where the catapult mass per unit areas are representative of nature. The observed drop off in the ejecta mass after 2.2*R* is where the top of the laboratory ejecta was located. These data are for shots using 6 (green), 8 (maroon), and 10 kg (cyan) of gravel. We used the last mass data point before the rollover (i.e., contained within the red circled area) for each mass range (6, 8, or 10 kg) to define the landing location of the top of the representative curtain for the runout length *L* calculations.

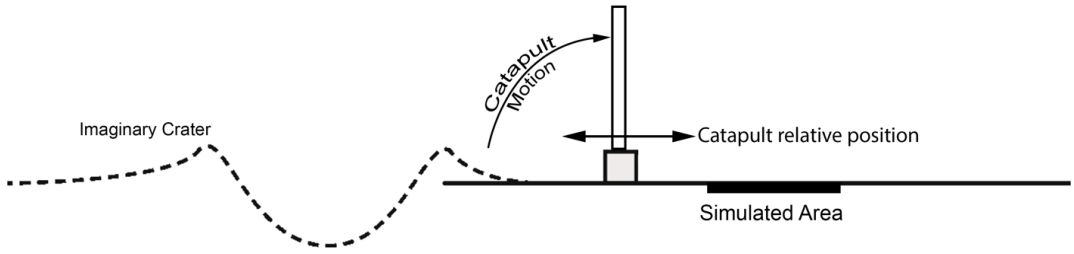

Figure 4.8. The catapult sits some distance from the rim of the imaginary crater, which is only discovered *post-hoc* by fitting catapult ejecta velocity profiles to theoretical ejecta velocity profiles from scaling relations. As such, the catapult is not necessarily on the rim of the imaginary crater. Areas simulated by the catapult's curtain and deposit are small relative to the size of the imaginary crater and the entire ejecta facies. For imaginary craters simulating the mass per unit area relationship, the catapult sits 1.8R downrange from a R = 3 m imaginary transient crater.

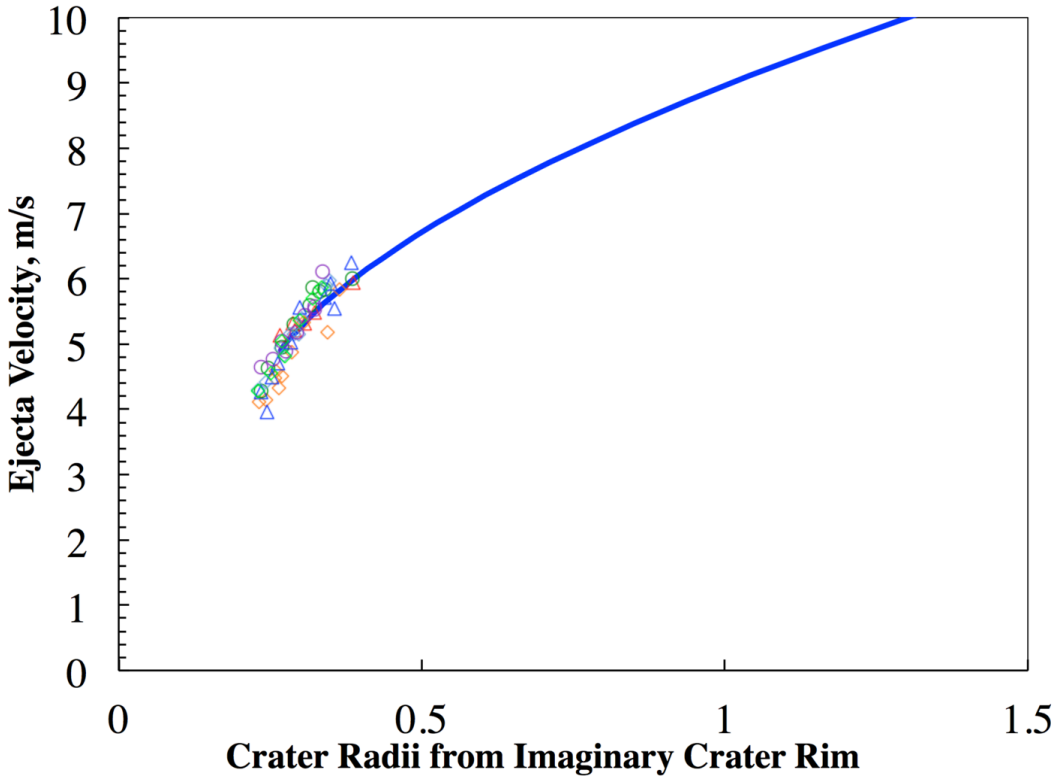

Figure 4.9. Velocity data points from 0.3-1.4 m from the catapult show the ejecta curtain velocity profile just as it strikes the ground (landing speed). The data are from seven experiments with 6, 8, or 10 kg of ejecta simulant. The blue curve is the theoretical velocity profile. By varying imaginary crater size and distances, we discovered *post-hoc* that the catapult simulates the ejecta curtain velocity profile (blue curve) for a 6 m radius transient crater with the catapult 0.16 transient crater radii downrange of the crater rim with an average error of 2.7%. Strictly speaking, the theoretical blue curve is the ejecta launch velocity from within the crater, but assuming negligible differences in launch versus landing height, the launch and landing velocities would be equal.

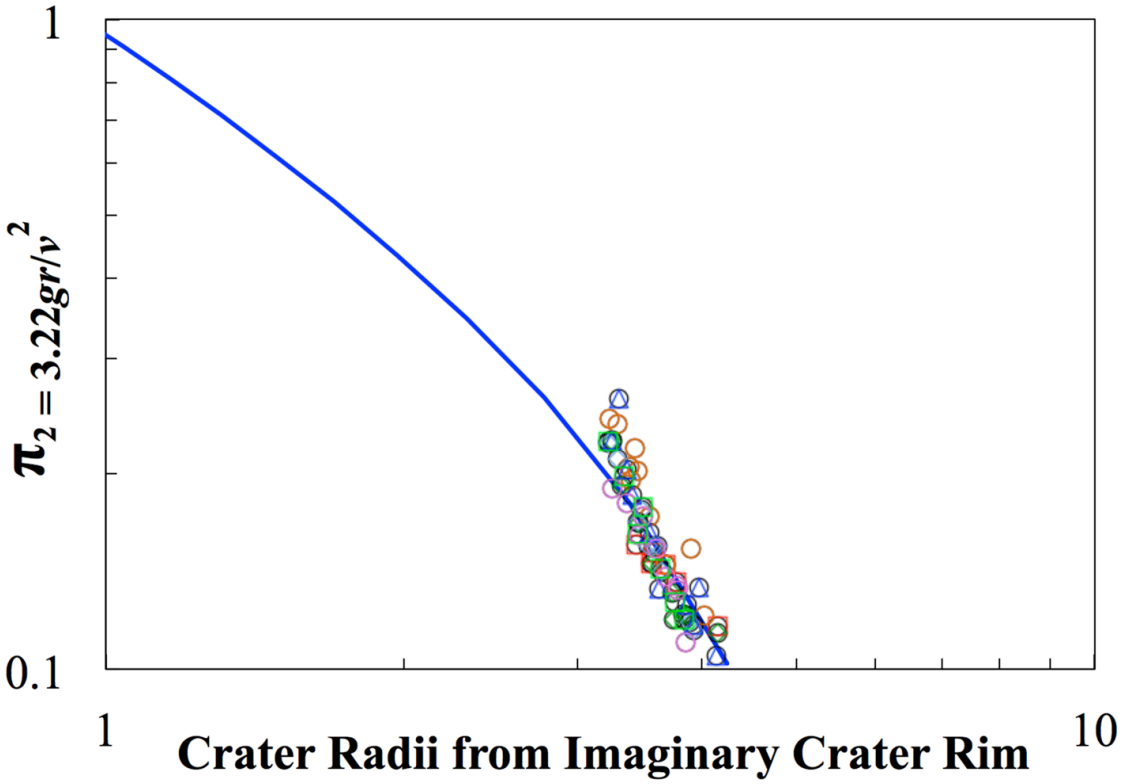

Figure 4.10. A plot of the ejecta curtain's non-dimensional velocity π_2 as a function of non-dimensional distance in transient crater radii from the rim of a crater. The transient crater radius of 1.0 m and an offset from the transient crater rim of 2.8*R*. This shows that the Catapult simulates the π_2 curtain profile as it lands from distances of 3-4*R* from the imaginary crater's rim.

Figure 4.11. Dynamically flowing ejecta deposits mobilize "regolith" grains in a manner reminiscent of aeolian saltation, seen here as circled plain-colored grains. We also picked up plain-colored "regolith" grains in the overflow area around the gravel target box, which is further evidence of lateral mobilization of regolith by ejecta.

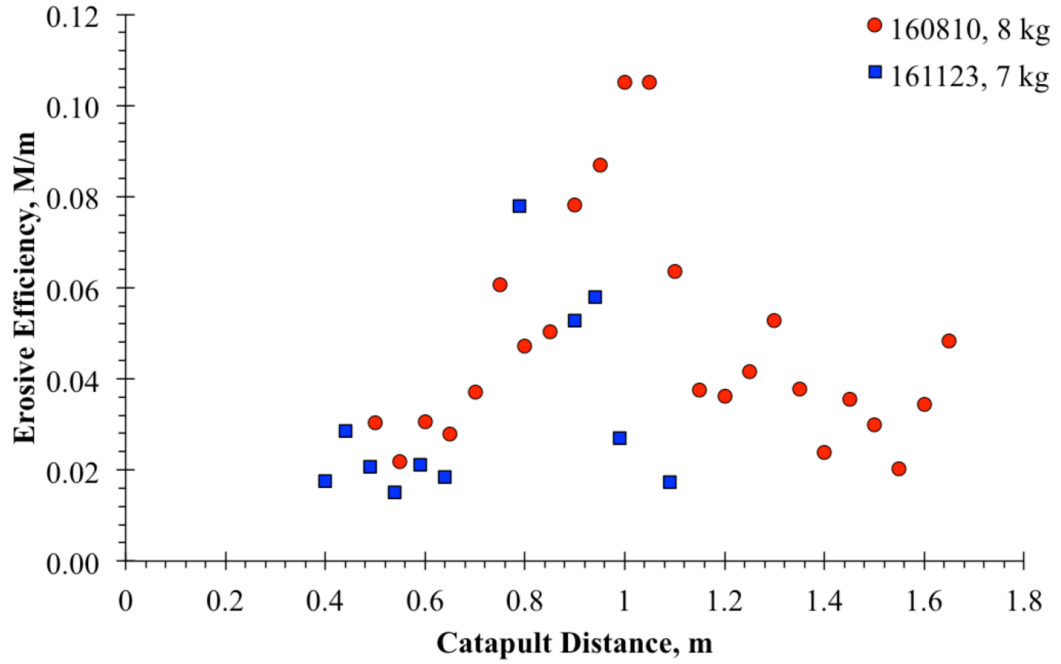
160810, 8 kg
161123, 7 kg
Erosive Efficiency, M/m
0.12
0.10
0.08
0.06
0.04
0.02
0.00
0
0.2
0.4
0.6
0.8
1
1.2
1.4
1.6
1.8
Catapult Distance, m

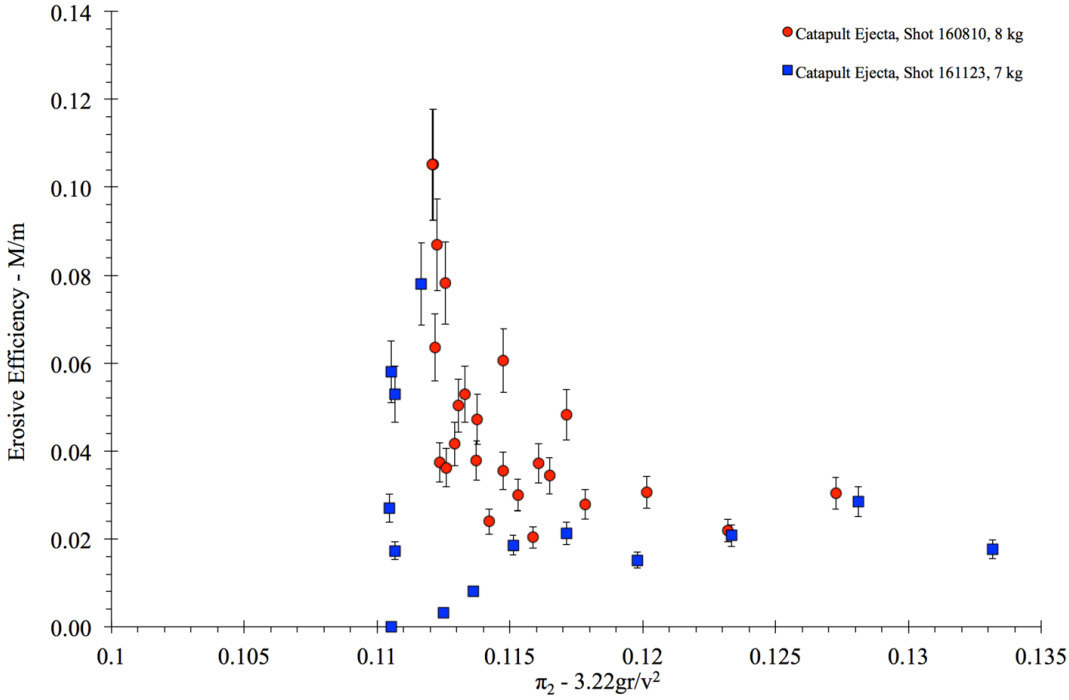
Catapult Ejecta, Shot 160810, 8 kg
Catapult Ejecta, Shot 161123, 7 kg
Erosive Efficiency - M/m
0.14
0.12
0.10
0.08
0.06
0.04
0.02
0.00
0.1
0.105
0.11
0.115
0.12
0.125
0.13
0.135
π2 - 3.22gr/v2

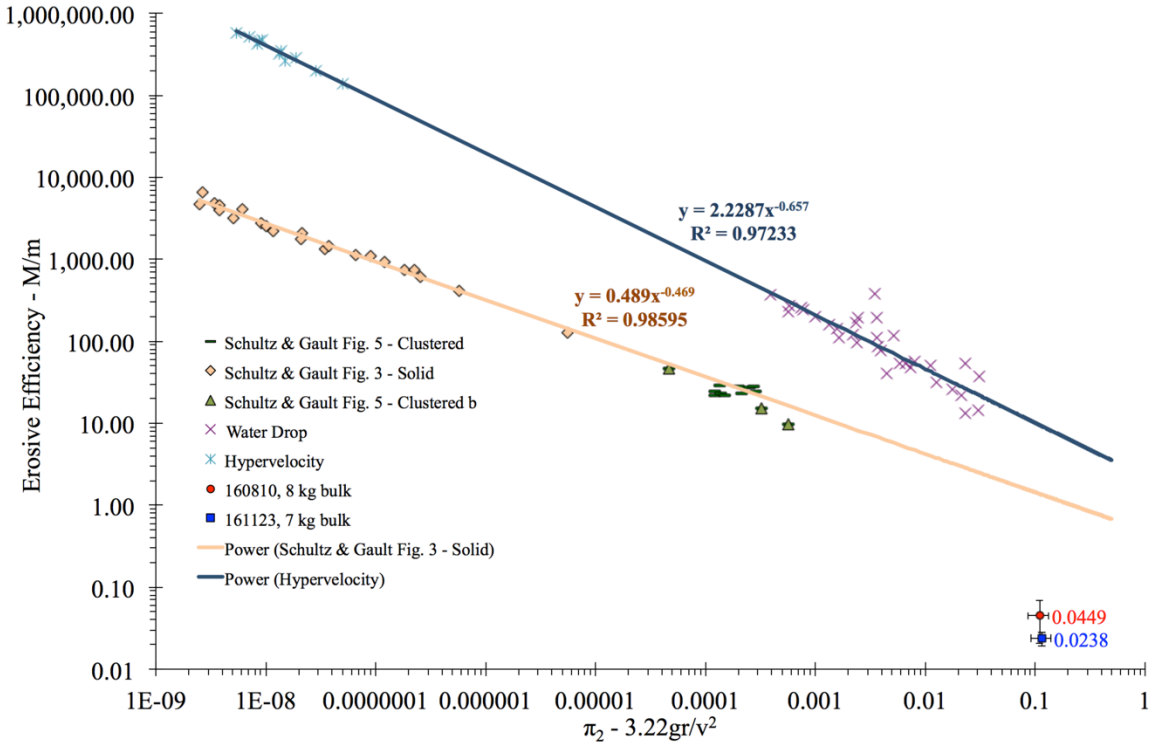

Figure 4.12. *Top:* Erosive efficiency for the two fine gravel experiments 160810 and 161123 using 8 and 7 kg of ejecta, respectively, as a function of catapult distance. *Middle*: Erosive efficiency of red fine gravel depositing onto blue fine gravel from two experiments. The erosive efficiency falls off quickly with respect to π_2. *Bottom*: The same experimental values averaged together for each experiment plotted in the context of both hypervelocity (Schultz and Gault, 1985) and water drop impact (Holsapple and Schmidt, 1982 and references therein) experiments. Ejecta experiments do not plot along the power law relations from other experiments, but they are in the plot space expected for such a low-efficiency erosion or "impact" process. Our data may indicate a separate power law in the erosive efficiency behavior and that at such low speeds the assumption of a point source impact is not applicable as it is for hypervelocity experiments. This potential new power law may be hinted at by the scattered clustered impactor data (green triangles,

Schultz and Gault, 1985). The range of ejecta data is for ejecta impact distances between 0.63 and 1.36 meters from the catapult.

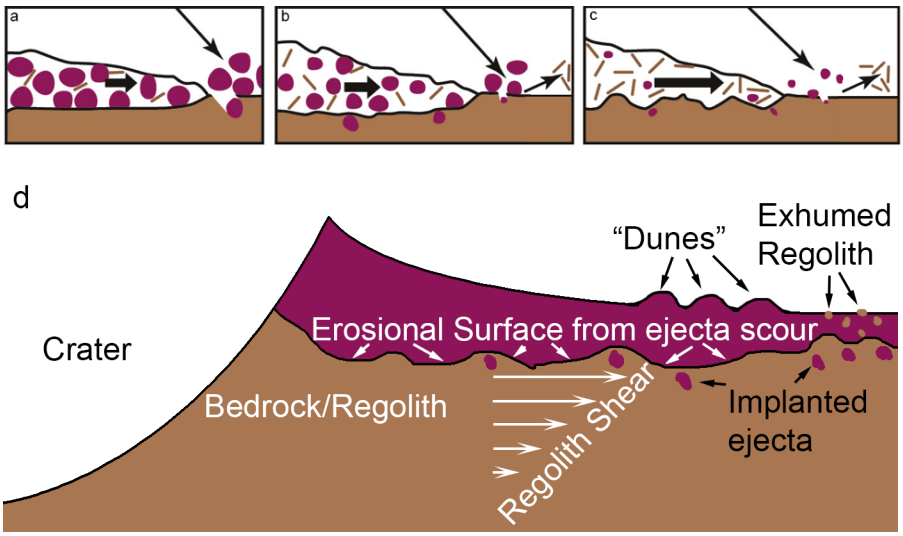

Figure 4.13. Manifestations of ballistic sedimentation. As the ejecta curtain deposits itself, just-landed ejecta continues to slide away from the crater. (A) The ejecta curtain lands (right side of frame), and some of it becomes embedded in the regolith, perhaps fast enough to be considered as secondary cratering. The rest of the deposit continues forward along the ground, incorporating regolith into the ejecta flow. (B) Some ejecta grains become trapped in the regolith beneath the ejecta deposit, which continues its flow and erodes the regolith substrate. Energetic portions of the curtain loft pre-impact regolith on saltation-like trajectories (lofted brown grains, far right side). This process continues into frame (C). Modified from Oberbeck (1975), Melosh (1989), and Kring. (D) The final stratigraphy shows implanted ejecta, exhumed regolith, erosional contract, sheared regolith at depth, and dune-like landforms, also called crater concentric ridges (Atwood-Stone et al., 2016).

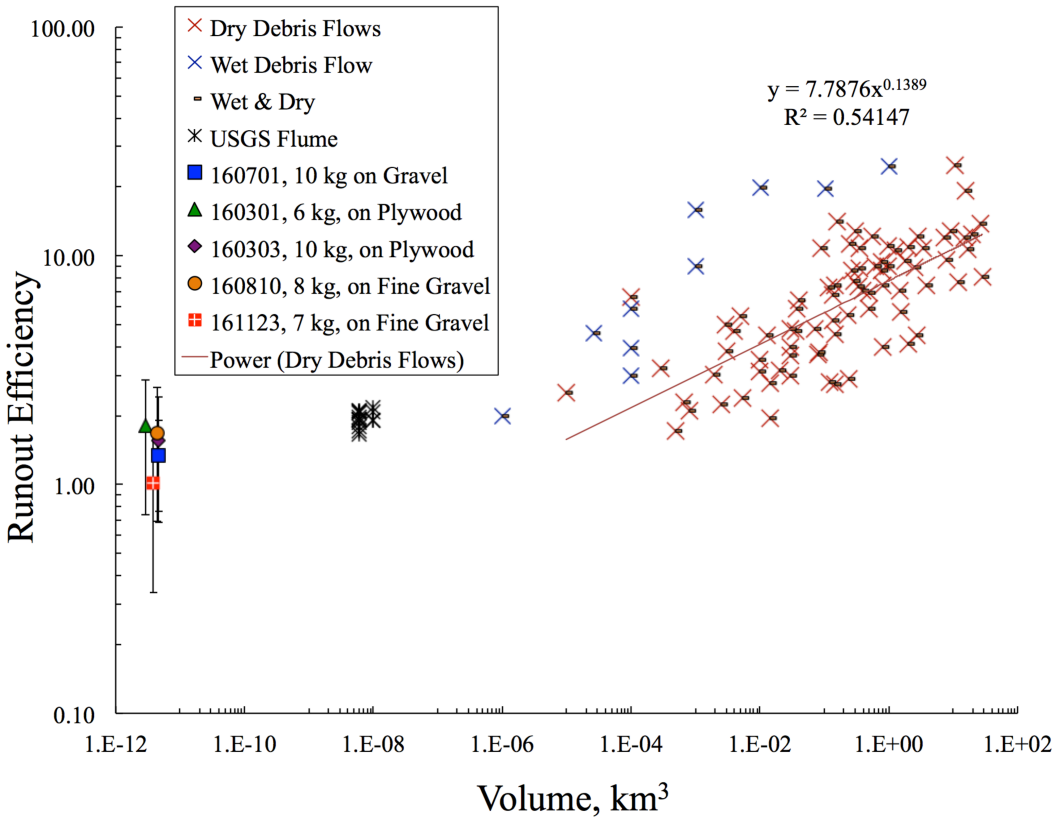

Figure 4.14. Runout efficiency $1/R_f$ compared against emplaced volume, with catapult results on the far left (filled polygons). Wet and dry debris flows are represented with x's (data from Iverson, 1997 and Hayashi and Self, 1992), and debris flow flume experiments are represented with asterisks *'s (data from Logan and Iverson, 2007; 2013). Both the debris flow experiments and the field measurements used the distal extents method as opposed to the more physically correct (but less geologically relevant) COM method. Iverson (1997) reports less dependence on flow volume for volumes under 10^{-4} km^3, which is consistent with our catapult findings. We calculated the ejecta runout efficiencies based on the maximum runout distance estimate where most of the uncertainty derives from the spread of measured values for L and the range of ejecta flow speeds. Note that our $1/R_f$ values are similar for some landslides with volumes up to 1 km^3 (12 decades greater in volume).

Experiment	Mass, kg	Target	Measurement(s)
151209,6	6	(Buckets)	Mass per unit area measurement
160207	6	(Buckets)	Mass per unit area measurement
151113	8	(Buckets)	Mass per unit area measurement
151209,10	10	(Buckets)	Mass per unit area measurement
160121	10	(Buckets)	Mass per unit area measurement
160212	10	(Buckets)	Mass per unit area measurement
151211	6	Plywood	*e*
160229	6	Plywood	Runout distance, *e*
160303	6	Gravel (pink ejecta)	*e*, erosion/deposition thickness, curtain footprint thickness
151204	8	Plywood	*e*
151210	10	Plywood	*e*
151222	10	Plywood	*e*
160105	10	Plywood	Runout distance
160301	10	Plywood	Runout distance
160701	10	Gravel ("rainbow" ejecta)	Runout distance, *e*, erosion/deposition thickness, curtain footprint thickness
160810	8	Fine blue gravel (fine red ejecta)	Runout distance, erosion/deposition thickness, curtain footprint thickness
161123	7	Fine blue gravel (fine red ejecta)	Runout distance, erosion/deposition thickness

Table 4.1. List of experiments and associated measurements reported in this paper. These experiments include both those experiments to demonstrate dynamic similarity to natural curtains and those experiments to determine dynamics of surface ejecta and regolith.

Experiment	Ejecta Mass, kg	Target	Pre-Slide extent, m	Post-Slide Extent, m	Runout Distance L, m	% of Initial Landing Distance (Stretch)	$1/R_f$	Notes
160701 "rainbow gravel"	10	Plain gravel	1.01 ± 0.03	1.48 ± 0.03	0.47 ± 0.06	47% ± 6%	3.23 ± 52%	Tracked red/green boundary
160301_6kg	6	Plywood	0.92 ± 0.10	1.90 ± 0.05	0.98 ± 0.15	107% ± 27%	1.8 ± 59%	
160301_10kg	10	Plywood	1.5 ± 0.10	2.75 ± 0.05	1.25 ± 0.15	83% ± 17%	1.55 ± 56%	
160810	8	Fine blue gravel	1.16 ± 0.10	1.68 ± 0.05	0.52 ± 0.15	45% ± 22%	1.68 ± 59%	Fine red gravel ejecta
161123	7	Fine blue gravel	1.33 ± 0.10	1.68 ± 0.03	0.35 ± 0.13	26% ± 18%	1.02 ± 67%	Fine red gravel ejecta

Table 4.2. Runout distances and runout efficiencies using the distal extents method for lab ejecta. The pre-slide extent is based on the furthest point in the curtain's mass profile that is representative of a natural curtain (just before the mass rollover discussed in the text) as measured by the "bucket" experiments in Table 4.1. Experiment 160701 is the exception to this and we used the red-green color boundary, which likely under predicts the runout distance and speed and thus over-predicts the runout efficiency. The post-slide extent was based on when 50% of the distal boundary was present, based on pixel values corresponding to ejecta grains. Uncertainties are estimated based on the size of the search areas, i.e., the 10 cm-wide buckets and the 5 cm-wide photograph search areas for runout; and from the uncertainties in the empirical ejecta flow models for the different masses and targets.

References

Austin, M.G., Thomsen, J.M., Ruhl, S.F., Orphal, D.L., Schultz, P.H., 1980. Calculational investigation of impact cratering dynamics: Material motions during the crater growth period. In: Lunar and Planetary Science Conference, 11th, Houston, TX, March 17-21, 1980, Proceedings. Volume 3. (A82-22351 09-91) New York, Pergamon Press, 1980, p. 2325-2345.

Baloga, S.M., Fagents, S.A., Mouginis-Mark, P.J., 2005. Emplacement of Martian rampart crater deposits. Journal of Geophysical Research, 110, E10001, doi:10.1029/2004JE002338.

Barlow, N.G., 2005. A review of Martian impact crater ejecta structures and their implications for target properties. Geological Society of America Special Paper, ;in Kenkmann. T., Hörz. E. and Deutsch, A., eds., Large meteoritic impacts III: Geological Society of America Special Paper 384, p. 433-442, doi: 10.1130/0-8137-2384-1.433.

Barlow, N.G., Boyce, J.M., Cornwall, C., 2014. Martian Low-Aspect-Ratio Layered Ejecta (LARLE) craters: Distribution, characteristics, and relationship to pedestal craters. Icarus, 239, 186-200, doi: 10.1016/j.icarus.2014.05.037.

Barnouin-Jha, O.S., and D.L. Buczkowski, 2007. Comparing the runout of fluidized ejecta on Mars with mass movements on Earth. 37th Lunar and Planetary Science Conference, Abstract #1304.

Barnouin-Jha, O.S., Yamamoto, S., Toriumi, T., Sugita, S., Matsui, T., 2007, Non-intrusive measurements of crater growth. Icarus, 188, doi:10.1016/j.icarus.2007.01.009.

Boyce, J., Barlow, N., Mouginis-Mark, P., Stewart, S., 2010. Rampart craters on Ganymede: Their implications for fluidized ejecta emplacement. Meteoritics and Planetary Science, 45, 4, p. 638-661, doi: 10.1111/j.1945-5100.2010.01044.x.

Boyce, J.M., Mouginis-Mark, P.J., 2006. Martian craters viewed by the Thermal Emission Imaging System instrument: Double-layered ejecta craters. J. Geophys. Res. 111, E10005, doi:10.1029/2005JE002638.

Carr, M.H., Crumpler, L.S., Cutts, J.A., Greeley, R., Guest, J.E., Masursky, H., 1977. Martian impact craters and emplacement of ejecta by surface flow. Journal of Geophysical Research, 82, 28, doi:10.1029/JS082i028p04055.

Chao, E.C.T., 1974. Impact cratering models and their application to lunar studies—a geologist's view. Proc. of the 5th Lunar Science Conference, Supplement 5, Geochemica et Cosmochimica Acta, 1, p. 35-52

Chao, E.C.T., 1976. Mineral-produced high-pressure striae and clay polish: Key evidence for nonballistic transport of ejecta from Ries Crater. Science, 194, 4265, p. 615-618, doi: 10.1126/science.194.4265.615-a.

Cintala, M.J., Berthoud, L., Hörz, F., 1999. Ejection-velocity distributions from impacts into coarse-grained sand. Meteoritics and Planetary Science, 34, 4, 605-623, doi: 10.1111/j.1945-5100.1999.tb01367.x.

Denevi, B.W., et al., 2012. Physical constraints on impact melt properties from Lunar Reconnaissance Orbiter Camera images. Icarus, 219, 665-675, http://dx.doi.org/10.1016/j.icarus.2012.03.020.

Denevi, B.W., et al., 2013. The distribution and origin of smooth plains on Mercury. J. Geophys. Res., Planets, 118, 5, 891-907, doi:10.1002/jgre.20075.

Erismann, T.H., Abele, G., 2001. Dynamics of Rockslides and rockfalls. Springer, 291 p. ISBN 3-540-67198-6.

Gault, D.E., Quaide, W.L., Oberbeck, V.R., 1968. Impact cratering mechanics and structures. Shock metamorphism of natural materials, Mono Book Corporation. B.M French and N.M. Short, eds.

Ghent, R.R., Carter, L.M., Bandfield, J.L., Tai Udovicic, C.J., Campbell, B.A., 2016. Lunar crater ejecta: Physical properties revealed by radar and thermal infrared observations. Icarus, 273, 182-195, doi:10.1016/j.icarus.2015.12.014.

Gutt, G.M., 1989. The physics of granular systems. PhD Thesis, California Institute of Technology, CaltechETD:etd-05302007-081951, http://resolver.caltech.edu/CaltechETD:etd-05302007-081951.

Hamran, S.E., et al., 2015. RIMFAX: a GPR for the Mars 2020 Rover Mission. IEEE Xplore, doi:10.1109/IWAGPR.2015.7292690.

Hartmann, W.K., 1985. Impact experiments 1. Ejecta velocity distributions and related results from regolith targets. Icarus, 63, 69-98, doi:10.1016/0019-1035(85)90021-1.

Hayashi, J.N., Self, S., 1992. A comparison of pyroclastic flow and debris avalanche mobility. Journal of Geophysical Research, 97, B6, 9063-9071, DOI: 10.1029/92JB00173.

Holsapple, K.A., 1993. The scaling of impact processes in planetary sciences. Annu. Rev. Earth Planet. Sci., 21, 333-373.

Holsapple, K.A., Housen, K.R., 2007. A crater and its ejecta: An interpretation of Deep Impact. Icarus, 187/1, 345-356, doi:10.1016/j.icarus.2006.08.035.

Holsapple, K.A., Schmidt, R.M., 1982. On the scaling of crater dimensions 2: Impact Processes. J. Geophys. Res., 87, B3, 1849-1870, doi: 10.1029/JB087iB03p01849.

Hörz, F., Ostertag, R., Rainey, D.A., 1983. Bunte Breccia of the Ries: Continuous deposits of large impact craters. Reviews of Geophysics and Space Physics, 21, 8, p. 1667-1725, DOI: 10.1029/RG021i008p01667.

Housen, K.R., Holsapple, K.A., 2011. Ejecta from impact craters. Icarus, 211, 856-875, doi:10.1016/j.icarus.2010.09.017.

Housen, K.R., Schmidt, R.M. & Holsapple, K.A., 1983. Crater ejecta scaling laws - Fundamental forms based on dimensional analysis. 88, pp.2485–2499.

Iverson, R.M., 1997. The physics of debris flows. Reviews of Geophysics, 35, 3, 245-296, doi: 10.1029/97RG00426.

Iverson, R.M., Reid, M.E., Logan, M., et al., 2010. Positive feedback and momentum growth during debris-flow entrainment of wet bed sediment. Nature Geoscience, 4, doi: 10.1038/NGEO1040.

Iverson, R.M., 2015. Scaling and design of landslide and debris-flow experiments. Geomorphology, 244, 9-20, doi: 10.1016/j.geomorph.2015.02.033.

Kenkmann, T., Ivanov, B.A., 2006. Target delamination by spallation and ejecta dragging: An example from the Ries crater's periphery. Earth and Planetary Science Letters, 252, 15-29, doi:10.1016/j.epsl.2006.08.024.

Kenkmann, T., Schönian, F., 2006. Ries and Chicxulub: Impact craters on Earth provide insights for Martian ejecta blankets. Meteoritics and Planetary Science 41, 10, 1587-1603, DOI: 10.1111/j.1945-5100.2006.tb00437.x.

Logan, M., Iverson, R.M., 2007, revised 2013. Video documentation of experiments at the USGS debris-flow flume 1992–2006 (amended to include 2007–2013): U.S. Geological Survey Open-File Report 2007–1315 v. 1.3., http://pubs.usgs.gov/of/2007/1315/.

Maxwell, D.E., 1977. Simple Z model of cratering, ejection, and the overturned flap. In Impact and Explosion Cratering, Pergamon Press (New York), p. 1003-1008, Roddy, D.J., Pepin, R.O, and Merrill, R. B., eds.

McGetchin, T.R., Settle, M., Head, J.W., 1973. Radial thickness variation in impact crater ejecta: Implications for lunar basin deposits. Earth and Planetary Science Letters, 20, 226-236, https://doi.org/10.1016/0012-821X(73)90162-3.

Melosh, J.H., 1989. Impact cratering: A geologic process. Oxford Monographs on Geology and Geophysics, 11, 253 p.

Mouginis-Mark, P., 1979. Martian fluidized crater morphology: Variations with crater size, latitude, altitude, and target material. Journal of Geophysical Research, 84, B14, doi: 10.1029/JB084iB14p08011.

Oberbeck, V.R., 1975. The role of ballistic erosion and sedimentation in lunar stratigraphy. Rev. Geophys. and Space Phys., 13, 2, p. 337-362, doi: 10.1029/RG013i002p00337.

Oberbeck, V.R., Morrison, R.H., Hörz, F., 1975. Transport and emplacement of crater and basin deposits. In The Moon, 13: 9, doi:10.1007/BF00567505.

Rice, M.S., Warner, N.H., 2016. Sediment sources for the Eberswalde delta: Stratigraphy and mineralogy of the Eberswalde Crater catchment. Geological Society of

America Abstracts with Programs, 48, 7, Abstract #20-4, doi: 10.1130/abs/2016AM-287720.

Richardson, J.E., Melosh, H.J., Lisse, C.M., Carcich, B., 2007. A ballistic analysis of the Deep Impact ejecta plume: Determining Comet Tempel 1's gravity, mass, and density. Icarus, 191, 176-209, doi:10.1016/j.icarus.2007.08.033.

Richardson, J.E., 2011. Modeling impact ejecta plume evolution: A comparison to laboratory studies. Journal of Geophysical Research, 116, E12004, doi:10.1029/2011JE003844.

Robbins, S.J., Hynek, B.M., 2012. A new global database of Mars impact craters ≥ 1 km: 1. Database creation, properties, and parameters. J. Geophys. Res. 117, (E5). doi: 10.1029/2011JE003966.

Sharpton, V.L., 2014. Outcrops on lunar crater rims: Implications for rim construction mechanisms, ejecta volumes and excavation depths. Journal of Geophysical Research, Planets, 119, doi:10.1002/2013JE004523.

Shoemaker, E.M., 1962, Exploration of the Moon's surface. American Scientist, 50, 1, Frontiers of Zealous Research, p. 99-130.

Schmitt, H.H., Petro, N.E., Wells, R.A., Robinson, M.S., Weiss, B.P., Mercer, C.M., 2017. Revisiting the field geology of Taurus-Littro. Icarus, in press, http://doi.org/10.1016/j.icarus.2016.11.042.

Schmidt, R.M., Housen, K.R., 1987. Some recent advances in the scaling of impact and explosion cratering. Int. J. Impact Engng., 5, 543-560, doi:10.1016/0734-743X(87)90069-8.

Schultz, P.H., 1992. Atmospheric effects on ejecta emplacement and crater formation on Venus from Magellan. Journal of Geophysical Research, 97, E10, p. 16,183-16,248, doi:10.1029/92JE01508.

Schultz, P.H., Gault, D.E., 1985. Clustered impacts: Experiments and implications. J. Geophys. Res., 90, B5, p. 3701-3732, doi: 10.1029/JB090iB05p03701.

Stickle, A.M., Patterson, G.W., Cahill, J.T.S., Bussey, D.B.J., 2016. Mini-RF and LROC observations of mare crater layering relationships. Icarus, 273, 224-236, doi: 10.1016/j.icarus.2016.03.014.

Wada, K., Senshu, H. & Matsui, T., 2006. Numerical simulation of impact cratering on granular material. Icarus, 180, pp.528–545, http://doi.org/10.1016/j.icarus.2005.10.002.

Wünnemann, K., Zhu, M.-H., Stöffler, D., 2016,

Yamamoto, S., Barnouin-Jha, O.S., Toriumi, T., Sugita, S., Matsui, T., 2009. An empirical model for transient crater growth in granular targets based on direct observations. Icarus, 203, p. 310-319, doi:10.1016/j.icarus.2009.04.019.

Appendix C

Table C1. Values used in equations throughout this paper which may not be defined in the text. Sorted alphabetically.

Variable	Definition
c	Empirical value = 0.47
dl	Landing position change
dx	
e	Ratio of sliding ejecta KE to just-landed ejecta KE.
g	Gravity in the lab = 9.8 m/s^2
H	Height of landslide origin
k	Empirical constant, = 0.62
k_2	Empirical constant $k_2 = \frac{\mu}{(1+\mu)\cos(45^\circ)}$
L	Runout length of ejecta
L_{db}	Landing position of curtain's back
L_{df}	Landing position of curtain's front
l_{dr}	Curtain landing position
m	Emplaced mass (used in erosive efficiency as M/m)
M	Eroded mass (used in erosive efficiency as M/m)
M_e	Total ejecta mass
R	Transient crater radius
r, w	Ejecta curtain footprint width
R_b, x_ℓ	Ejecta launch position within crater, $x_l = R\left(\frac{t_l}{T}\right)^{\mu/(\mu+1)}$
R_f	Resistance factor for ejecta and avalanche runout. We use its reciprocal called the runout efficiency.
ρ	Bulk density
T	Total crater formation time
T_f	Time of flight for the ejecta
θ	Launch angle from the imaginary crater (45˚ from horizontal)
v	Emplaced volume (used in erosive efficiency as V/v)
V	Eroded volume (used in erosive efficiency as V/v)
v_c	Velocity of ejecta as it strikes the ground
v_e	Velocity of excavation at x.
x	Distance between ejecta launch distance and the crater center
x_{db}	Back position of the curtain
x_{df}	Front position of the curtain
x_{dr}	Incremental launch position within the transient crater
μ	Empirical value = 0.5

Size-Frequency Distribution of Gravel Ejecta Simulants

Table C2. Size-frequency distribution of a) fine gravel (using sieves), b) coarse plain gravel (using a Retsch CAMSIZER), and c) coarse colored gravel.

a) Fine Gravel	
Mesh Size, µm	% Retained
850	71%
425	28%
180	1%
125	<1%

b) Coarse Plain Gravel	
Equivalent Mesh Size, µm	% Retained
1,000,000	77.28%
4,000	14.22%
3,262	5.07%
2,661	2%
2,170	0.89%
1,770	0.38%
1,443	0.13%
1,177	0.03%

c) Coarse Colored Gravel	
Mesh Size, mm	% Retained
4.75	70.7%
3.35	25.2%
2.00	4.0%
1.00	<1%

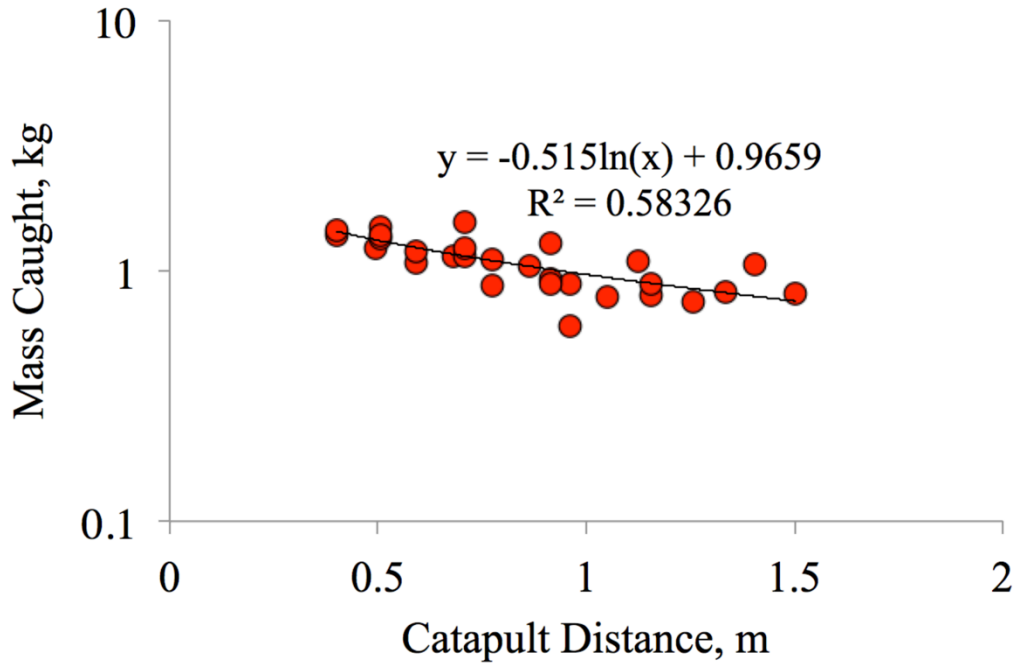

Figure C1. Mass catchment profiles for six experiments used to derive the empirical mass profile law for the catapult. The empirical catapult mass model is shown as a best-fit curve. The amount of mass used (between 6-10 kg) for a given experiment did not affect the mass distribution trend except to extend it further downrange for higher masses. Beyond 1.5 m, the mass falls off, indicating the edge of where the catapult ejecta curtain mass profile matches that of a natural ejecta curtain. Based on the empirical mass model, we estimate an uncertainty of 11%.

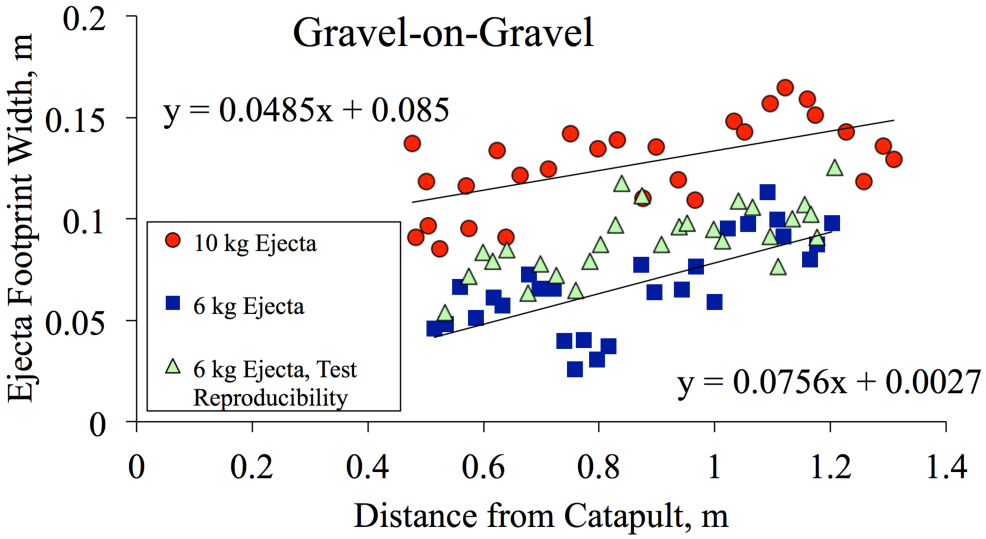

Figure C2. The width of the impacting ejecta curtain from the catapult (it's "footprint") widens distally. Larger masses of ejecta simulant placed on the catapult result in wider footprints. The 6-kg average width is 7 ± 2 cm (± 1 sigma), the test for reproducible data for the 6-kg average is 9 ± 2 cm, and the 10-kg average width is 13 ± 2 cm. The widening is not due to extra mass but rather to increased porosity higher up in the curtain due to relative motions between grains. To calculate π_2 we used a median empirical footprint model between the 6 kg and 10 kg measurements: $w = 0.06205x + 0.04385$, where x is meters from the catapult.

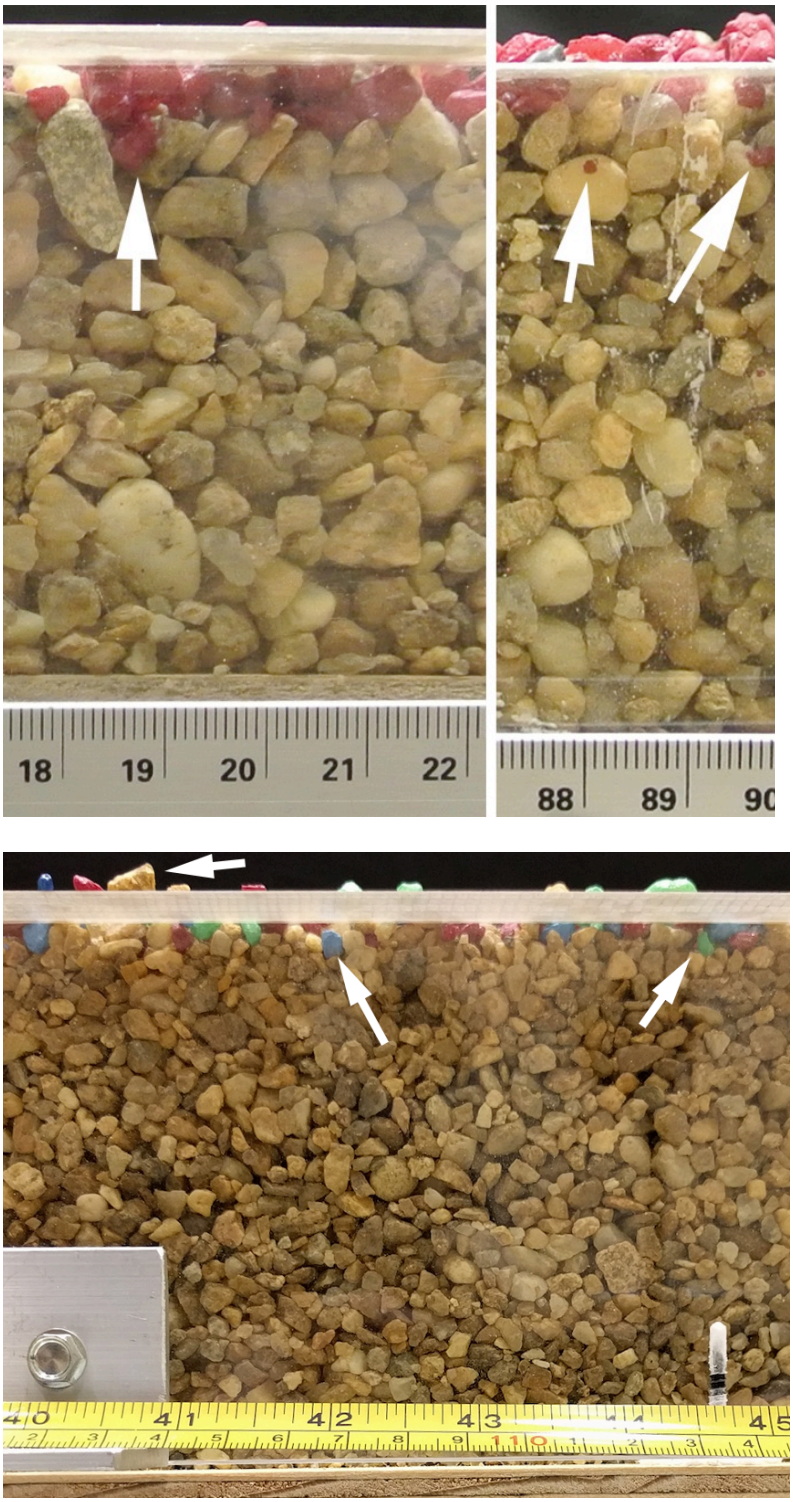

Figure C3. *Top:* Examples of occasional ejecta embedding itself in the pre-impact regolith (Experiment 160303). The centimeter scale shows distance from the proximal edge of the clear target box, which was 44 cm from the catapult. *Bottom:* arrows show

examples of ejecta grains embedding in regolith; the top arrows shows a regolith grain that was evidently mobilized and now sits atop the ejecta, emphasizing the heterogeneous and stochastic nature of ejecta emplacement. The tape measure starts at the up range end of the target box, which was 36 cm from the catapult.

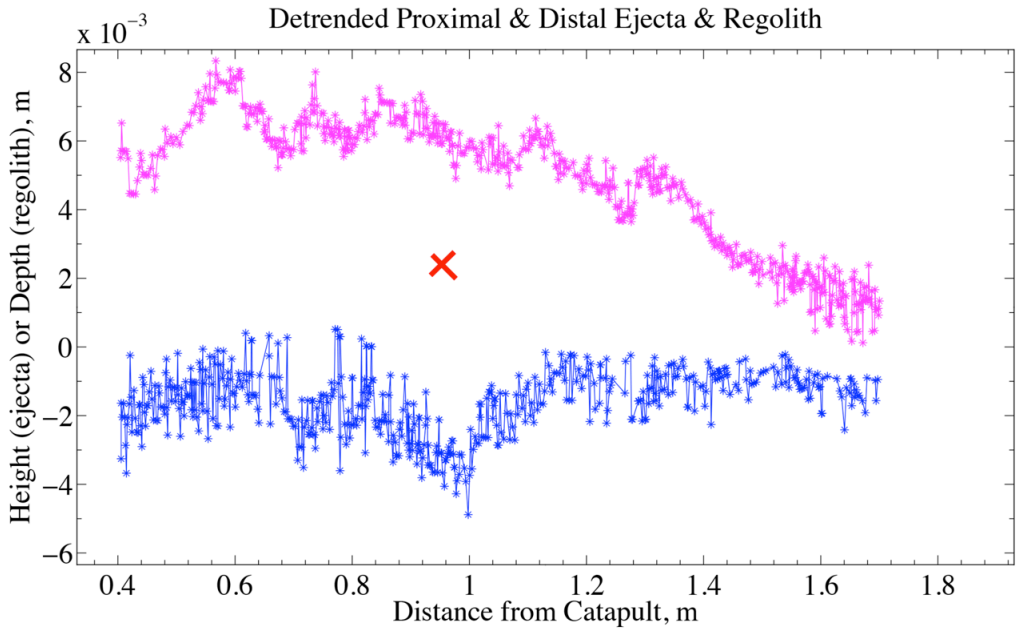

Figure C4. The topographic profile yielded from 8 kg of fine red gravel (pink data) deposited on fine blue gravel (blue curve) (experiment 160810) mapped from photogrammetrically controlled photographs through the side of the clear target box. The bold red X denotes the deposit's lateral center of figure, which is used as a proxy for the center of mass. Note the thinning ejecta deposit with distance from the catapult, analogous to natural ejecta facies.

Air Resistance on Ejecta Simulants

We claim that air resistance is negligible on both gravel sizes used of 5.1 mm and 2 mm.

The drag force F_d is

$F_d = ½\ C_d \rho_a A v^2$

where grains are assumed spherical and A is the frontal surface area (half the area of a sphere), v is velocity, ρ_a is the air density of 1.225 kg/m^3, and C_d is the drag coefficient assumed to be 0.5. C_d is estimated by calculating the Reynold's number R_e for flow around a grain and referencing a C_d versus R_e plot on a NASA website (https://www.grc.nasa.gov/www/k-12/airplane/dragsphere.html). For 5.1 mm quartz gravel traveling near the maximum measured speed of ~6.5 m/s, F_d = 0.001 N. Equating this force to Newton's 2nd law (using a density for quartz of 2600 kg/m^3 and a sphere volume for the given diameter), gives a deceleration of 5.5 m/s^2. The grains are in flight for 0.2 seconds or less, resulting in a velocity difference (compared to flight through a vacuum) of 1 m/s. For 2 mm clay gravel also traveling at 6.5 m/s, C_d = ~0.7 and F_d = 0.0002 N resulting in a speed difference compared to vacuum of 4 m/s. However, these values of 1 and 4 m/s are for individual grains, not for tightly clustered grains as we have. Thus, the actual velocity differences compared to vacuum for both grain sizes will be far less. Indeed, our videos show that the fine gravel curtain moves at the same velocity as the coarser gravel curtain. Because the catapult moves a bulk volume of air along with the grains, the grains are at rest with respect to the surrounding air parcel. A final line of reasoning justifies our ignoring air resistance: we fit the velocity profile of the laboratory curtain to the theoretical prediction for vacuum, so our fit implicitly accounts for air resistance.

Particle Velocimetry

The high speed camera records scenes at 1200 frames per second, which we save as a QuickTime® movie and then export as individual frames. Prior to each experiment, however, we imaged a calibration grid with grid lines every centimeter using the high speed camera. We created a text file correlating pixel locations in *xy* space with the corresponding physical positions, which we manually typed in. We wrote two Matlab scripts for the velocimetry analysis: one script to measure the simple ballistic motion of grains in the curtain and a second script to measure the granular motion of grains in the dynamic deposit. Both of these scripts used the calibration text file to both correct for lens distortion and to convert pixel space to physical space. Then, knowing the frame rate (1200 fps), converting grain displacement to velocity was trivial.

To calibrate for lens distortion in our calibration of pixel space to physical space, we used the Matlab function "lsqlin" to solve for a two-dimensional constrained linear least-squares best fit to calibration points defined on a grid. As an input, this used an ASCII file with four columns created by the user that correlated a point's *x* and *y* coordinates in pixels with user-input *x* and *y* coordinates in centimeters by clicking on grid intersection points on the calibration image. Because of lens distortion, the conversion from pixels to centimeters is not constant across the image. The constrained linear least squares fit provides a pixel-to-cm conversion as a function of both width and height across an image; this is roughly analogous to orthorectification in remote sensing photogrammetry.

Our Matlab curtain script displays five images of the curtain separated by 10 frames in which the final image shows a tracer grain just making initial contact with the

target. The user clicks on the same spot on the same grain in each image, then fits a parabola to the positions. This parabolic equation, together with the visual inspection of the landing location, reveals the landing velocity and initial landing distance from the catapult.

The "dynamic deposit script" is simpler. In it, the user selects two temporally-adjacent images from the image sequence and clicks on the same spot on the same grain in each. The mid-point and the velocity components and resultant speed are calculated. We conducted this analysis at intervals of 10 frames, selecting grains that had already landed but were within ~10 cm of the deposition front. The location, velocity, speed, and specific kinetic energy (measured in J/kg) were saved in an Excel spreadsheet.

When the catapult when it is cocked at 40˚ (Figure 4.2), the empirical model describing the grain speed an infinitesimal amount of time before impact is:

$s = 5.6659x^{0.3624}$,

where s is speed in m/s and x is distance in m from the catapult, is most applicable between 0.3 and 1.5 m from the catapult, and the ejecta grains strike the ground at 42˚ ± 2˚ from the horizontal. The error between this empirical model and measured grain speeds is 3%.

For the same conditions as above, the empirical mass distribution (Figure 4.C1) is

$Mass = -0.515\ln(x) + 0.9659$

where x is distance in m from the catapult. Note that this is mass as collected in the buckets and not mass per unit area.

We also used a semi-automatic grain identification and tracking algorithm for both the in-flight ejecta curtain and the ejecta dynamic deposit for the coarse-on-coarse

gravel experiments (160303 and 160701). The two approaches give similar velocity results but the semi-automatic technique can measure more grains. Figure 4.C5 shows a still movie frame from the analysis output.

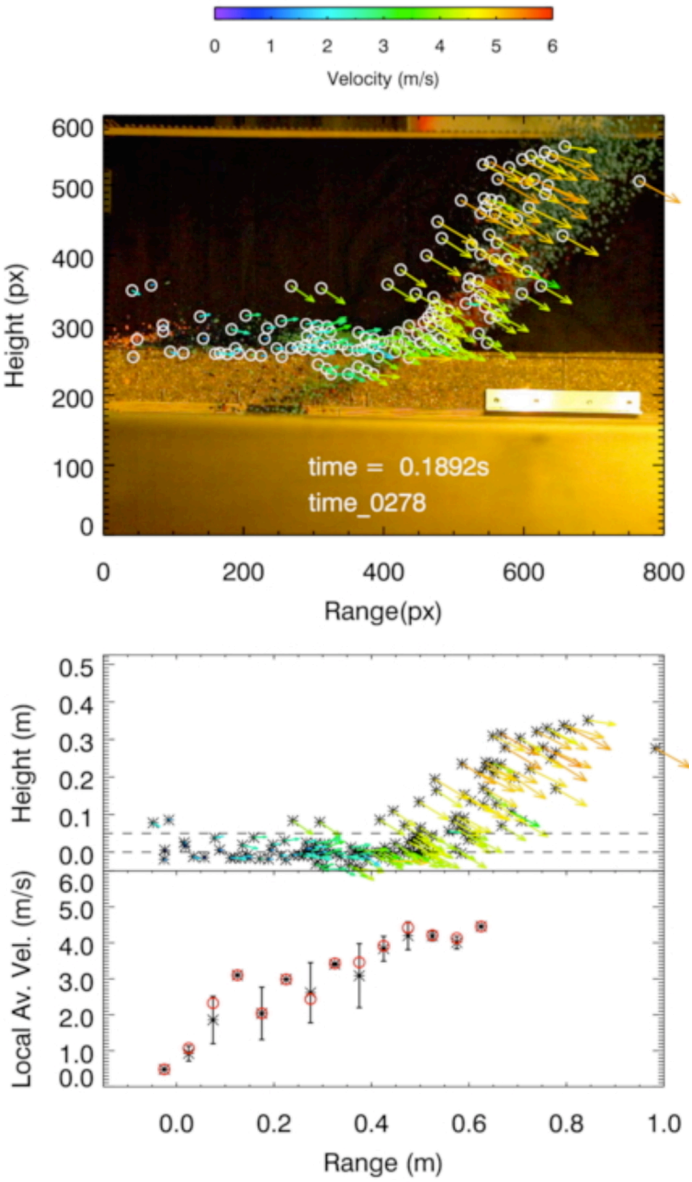

Figure C5. The top frame shows where the algorithm identified grains and the bottom two frames show the computed velocity for each grain. The bottom plot shows the averaged, standard deviation, and median grain velocities over a 5 cm-wide window.

Curtain Width Theory

Here we define the variables used in the main text to describe the landing locations from the front and back portions of a natural ejecta curtain. x_{db} is the launch position within the transient crater for material comprising the back of the curtain, and ranges from 0.6 to 0.98 crater radii (in steps *dx*) from the impact point (this range minimizes non-physical artifacts in the calculations). The launch velocity v_e at the back of the curtain is given by $v_{eb} = x_{dr}^{\frac{-1}{\mu}} \frac{\sqrt{Rg}}{k\left(\frac{1}{\mu}+1\right)}$. The time of flight T_{fb} for the curtain's back is $T_{fb} = \frac{2v_{eb}\sin(\theta)}{g}$. The calculations for the front of the curtain are more involved, but the necessary items to calculate are

total crater formation time *T*,

$$T = k\sqrt{\frac{R}{g}}$$

the time of launch of the curtain's back end, t_{launch_back},

$$t_{launch\_back} = T x_{dr}^{\frac{1}{\mu}+1}$$

the time of flight for the curtain's back end, T_{fb},

$$T_{fb} = \frac{2v_{ef}\sin(\theta)}{g}$$

the time of landing t_{lpb}, normalized to the total crater growth time,

$$t_{lpb} = \frac{t_{launch\_back} + T_{fb}}{T}$$

the velocity of the curtain's front side, v_{ef},

$$v_{ef} = \frac{gTt_{lpb}}{2\sin(\theta)}$$

and finally the front of the curtain's position at the time of launch x_{df} is given as

$$x_{df} = \left(\frac{v_{ef} k \left(\frac{1}{\mu} + 1 \right)}{\sqrt{Rg}} \right)^{-\mu}.$$

R = 1 m, and the other variables are defined in Table C1.

Curtain Areal Mass Density

Similar to above, we develop the parameters used to calculate the curtain's mass density during deposition as a function of distance from the crater. The above calculations for ejecta curtain position serve as a useful starting point for calculating the surface density (mass per unit area). The excavated volume at each step away from the impact point is

$dV_E = 3x_{dr}^2 k_m R^2 dx$, where

$k_m = 0.32k^{-3\mu}$

and dx is the change in excavation point radially from the center. We compute the incremental mass at each step using the characteristic ejecta bulk density as $dm_e = dV_E \rho$. Other parameters used in the calculations in the main text are the change in landing position

$$\frac{dl}{dx} = \frac{1}{R} - \frac{2k^2 \sin(\theta)}{\mu R} x_{dr}^{\frac{-2}{\mu}-1}$$

and the landing position is

$l_{dR} = x_{dr} + k^2 \sin(2\theta) x_{dr}^{\frac{-2}{\mu}}$.

The area A of a natural curtain's annular footprint and the corresponding mass is calculated as

$$A = -2\pi \left(\frac{dl}{dx}\right)(l_{dR})(R)(dx)$$

and the surface density is simple dV_E/A.

Matlab Script for Mapping Erosional Profiles and Converting from Pixel Position to Physical Location

```
%% Measure things in photos (like an erosion profile from
an ejecta
% experiment) by clicking, thereby making lots points. This
also has the
% option for converting from pixel space to physical space
and correcting
% for oblique imaging distortion.
% If just doing one image, run the 1st, 2nd, and 6th
sections of the script
clear, close all

MyPic=imshow(imread('/Users/runyokd1/Documents/CatapultExpe
riments/1412_MassDistro/141212_N01_MD_40deg/161123_BlueRedE
rosion_7kg/DSC_0509.JPG','jpg'));

axis image, zoom(4), title('Use the arrow keys to pan
around image','fontsize',16)
disp('Pan to a good part of the image, then run the next
part of the script'), hold on
%%
disp('Run the scripts next section when you are done')
(X,Y)=getpts;
plot(X,Y,'*-m')
%% OPTIONAL, post-processing
close all, clear
disp('Now open each figure file (the ones with the image)
and select all')
disp('data and save them sequentially as A, B, C, D, E,
etc. Then plot them all')
disp('on one figure, use the brush to re-save each data
with its original name')
disp('(A, B, etc.) in order to elimintate overlapping
data.')
disp('Run the next section when ready')

%% Combine Sections into one section
all=(A;B;C;D);
% Sorts by x position; keeps lines from crossing
% https://www.mathworks.com/matlabcentral/answers/108419-
sorting-data-points-so-x-are-in-ascending-order
X=all(:,1);
Y=all(:,2);
figure, plot(X,Y,'*-')
```

```
%% Space conversion
% Before running this section save the erosion and then
depositon profiles
% as X and Y
cal=csvread('/Users/runyokd1/Documents/CatapultExperiments/
1412_MassDistro/141212_N01_MD_40deg/161123_BlueRedErosion_7
kg/DSC_0509.csv',1);
Xc=cal(:,1); Xc=Xc'/100; %x in m
Yc=cal(:,2); Yc=Yc'/100; % y in m
xp=cal(:,3); xp=xp'; %x in px
yp=cal(:,4); yp=yp';
one=ones(1,length(Xc));
a=(xp; yp; one; 0.*one; 0.*one; 0.*one; -xp.*Xc; -yp.*Xc);
b=(0.*one; 0.*one; 0.*one; xp; yp; one; -xp.*Yc; -yp.*Yc);
c=(a,b)';
d=(Xc,Yc);
(sol, resnorm, residual)=lsqlin(c,d);

xc1=sol(1).*X+sol(2).*Y+sol(3);
xc1=xc1./(sol(7).*X+sol(8).*Y+1);
yc1=sol(4).*X+sol(5).*Y+sol(6);
yc1=yc1./(sol(7).*X+sol(8).*Y+1);

figure
plot(xc1,yc1,'*-b'), axis equal
disp('If you need to select more points in this image, save
the previous plot as a .fig file and')
disp('then re-run this script and just pan to a different
part of the image.')
disp('Next, you will assemble the profile segments. Just
read the instructions.')
thickness=max(yc1)-min(yc1)
```

Chapter 5: Conclusion

This PhD Thesis has been a contribution to geomorphology and dynamics as applicable to Mars, the Moon, and other planets. I mainly used both remote sensing observations and laboratory experiments, with some input from the results of numerical modeling. I applied the aeolian morphodynamic observations and numerical modeling to Mars and the impact cratering experiments and observations to any solid Solar System world but with a focused case study for Earth's Moon.

In Chapter 1 I set the stage for both aeolian morphodynamics and impact cratering experiments, giving an introductory background for both topics. In Chapter 2 I identified and described the Herschel-type aeolian sequence and linked changes in measured sand flux downwind (likely from an atmospheric internal boundary layer (IBL)) from slip face measurements to the changes in aeolian morphology within a Herschel-type sequence. I also pioneered the use of the panel method in aeolian geology (borrowing it from aeronautical engineering) for predicting wind speed and thus sand flux along slopes. I showed that by combining flux predictions from IBL theory and the panel method that the general trend in decreased sand flux downwind could be reproduced. The overarching impact is that other Herschel-type aeolian fields could have their broad aeolian sand flux accurately estimated without needing high resolution temporal imagery.

Chapter 3 built off my work in Chapter 2 and characterized a broad Martian sand sheet in order to constrain the formation boundary conditions for sheets versus sand dunes. I showed that Martian sand sheets can be just as active as dunes and hypothesized a new conceptual model for understanding Martian epochs of dune and sheet building and erosion and for identifying such epochs in the sedimentary stratigraphic record. Sand

suspension is likely the erosive agent for upwind dunes in the present epoch. I also pioneered a new method for the estimation of total sand flux on a sheet from remote measurements by ratioing total dune flux to ripple flux. Applying this new technique showed sheets to have comparable sand fluxes as dunes.

Shifting away from Martian aeolian morphodynamic geology, I described in Chapter 4 the new method for studying the geology of impact crater ejecta by use of a laboratory catapult. I showed the catapult to accurately reproduce a section of an impact crater ejecta curtain as predicted from theory. I then measured ejecta erosive and runout efficiency as a predictor for understanding ejecta stratigraphy on the Moon and other planets. Comparing the erosive efficiency with the gravity-scaled velocity, I showed the catapult results to be broadly consistent with crater scaling rules. Complimenting these quantitative measurements were qualitative descriptions of the types of behavior and morphology I observed showing the ejecta emplacement and substrate erosion process to be heterogeneous and dynamic.

CURRICULUM VITAE

Kirby D. Runyon

PhD Candidate, Johns Hopkins University
Department of Earth and Planetary Science, 301 Olin Hall
3400 N. Charles Street, Baltimore, MD 21218
email: kirby.runyon@gmail.com

Born

August 24, 1985, Jackson, Michigan, USA

Education

PhD Candidate in Planetary Geology, The Johns Hopkins University.
Dissertation title: Aeolian and Impact Crater Ejecta Geomorphology and Dynamics.
Expected graduation: May, 2017 (started August, 2012).

Master of Science in Planetary Geology, Temple University. 2011.
Thesis title: Structural Characterization of the Cerberus Fossae and Implications for Paleodischarge of Athabasca Valles, Mars.

Continuing educational credits in geosciences, Western Michigan University, 2008-2009

Bachelor of Arts in Physics; Mathematics minor, Houghton College, 2008

Research Interests

I seek to understand how planetary landscapes evolve. I accomplish this using remote sensing data (mainly visible-wavelength images and laser topography) and with laboratory experiments. My current interests include:

- Tracking and quantifying sand ripple and sand dune slipface migration on Mars using the HiRISE camera on Mars Reconnaissance Orbiter, on which I am a Collaborator. My aeolian interest extends to Titan, Venus, Earth, and Comet 67P.
- Mapping paleo-aeolian deposits on Mars to infer past aeolian regimes informed from current aeolian processes.
- Using low-gravity platforms (e.g., parabolic aircraft flights) for experiments into ejecta emplacement on small solar system bodies.
- Simulating the granular dynamics and resulting morphology of impact crater ejecta emplacement in a lab setting, applicable to any solid solar system body.
- Interpretation of geomorphology on Pluto and Charon; I am an affiliate member on the New Horizons Geology and Geophysics Imaging Team. Mars and Pluto are surprising analogs of each other in regards to sublimation-driven geology.
- Human spaceflight-enabled science; I am a qualified geological spacesuit test subject with NASA/Johnson Space Center's Crew and Thermal Systems Division. I have also worked in astronaut geology training curriculum development.
- Crater counting and the surface retention age for the asteroid Gaspra.

- Structural geology controls on floods and volcanism at the Cerberus Fossae and Athabasca Valles, Mars.

Occupational Experience

Community Service

- **Executive secretary** for a NASA grant review panel, 2017
- **Peer-reviewer** for planetary science journal Icarus, 2015, 2016.
- **Co-supervisor** for undergraduate intern in planetary geology, 2015.
- **Aeolian session chair** for the Lunar and Planetary Science Conference aeolian geology session, 2015, 2016.

Human Spaceflight

- **Spacesuit** test subject volunteer with NASA/JSC, 2015-present.
- **Test subjects volunteer** for NASA's Human Exploration Research Analog (HERA) program (pending)
- **Spaceflight** medical centrifuge test subject with University of Texas Medical Branch and the National Aerospace Training and Research Center (NASTAR), 2016.
- **Executive secretary** with the Lunar Exploration Analysis Group Geologic Astronaut Training Special Action Team (GAT-SAT), 2016.

Financial

- **Awarded** the JHU/Applied Physics Laboratory Graduate Student fellowship for three consecutive years, 2012-present.
- **Competitively won** a NASA/JPL student travel grant for the 4th International Planetary Dunes Workshop, 2015.
- **Competitively won** multiple internal JHU/Earth and Planetary Sciences department grants for educational travel, 2013-2015.

Political

- **Space policy activist** speaking with Congressional staffers in the House of Representatives and the Senate, 2014-present.

Other

- **Science consultant,** Mohawk Games: Martian and planetary geologic and spaceflight realism, 2014-present.
- **Taught** math and science, lecture and lab: Spring Arbor University, 2008; Temple University, 2009-2011; Holy Family University, 2011-2012.
- **Exploration Intern**, Lunar and Planetary Institute, 2011.
- **Scientific literacy and inspiration** public speaking engagements to general audiences, 2008-present.

Mission Experience

New Horizons mission to Pluto and the Kuiper Belt, 2014-present.
Geology and Geophysics Imaging group affiliate: I interpret and discuss the photographed geology of Pluto and Charon and have been a co-author on two high profile publications.

Mars Reconnaissance Orbiter/HiRISE Camera at Mars, 2013-present.

Collaborator: I assist in image planning and targeting, participate in science team discussions and telecons, and promote education and public outreach.

Concurrent mission concept design at APL iteratively integrating science and engineering constraints for conceptual robotic missions to Titan, 2013.

Publications

Peer-Reviewed Papers

Runyon, K.D., Bridges, N.T., Ayoub, F., Newman, C.E., and Quade, J.J., 2017, An integrated model for dune morphology and sand flux on Mars, Earth and Planetary Science Letters, 457, 204-212, doi:10.1016/j.epsl.2016.09.054.

Moore, J.M. and 40 others (including **Runyon, K.**), 2016, The Geology of Pluto and Charon through the eyes of New Horizons: Science, 351, 1284-1293, DOI: 10.1126/science.aad7055.

Stern, A.S., and 150 others (including **Runyon, K.**), 2015, The Pluto system: Initial results from its exploration by New Horizons: Science, 350, 1815-1:1815-8, DOI: 10.1126/science.aad1815.

Lemelin, M., Blair, D.M., Roberts, C.E., **Runyon, K.D.**, Nowka, D., Kring, D.A., 2015, High-priority lunar landing sites for in situ and sample return studies of polar volatiles: Planetary and Space Sciences, 101, 149-161, DOI: 10.1016/j.pss.2014.07.002.

Conference Abstracts (Selected)

Runyon, K.D., Bridgets, N.T., Newman, C.E., 2017, Eroding Dunes? Characterization and implications of Martian sand sheets: 48th LPSC, Abstract # 2187.

Runyon, K.D., S.A. Stern, T.R. Lauer W. Grundy, M.E. Summers, K.N. Singer, 2017, A geophysical planet definition: 48th LPSC, Abstract #1448.

Runyon, K.D., 2016, A successful case study of teaching evolutionary geoscience literacy in a conservative Christian church, GSA, Abstract #282890.

Runyon, K.D., Bridges, N.T., 2016, Morphology and dynamics of a Martian sand sheet, GSA, Abstract #282868.

Runyon, K.D., Barnouin, O.S., 2016, Ejecta Emplacement in the Lab: 47th LPSC, Abstract #1075.

Runyon, K.D., Lisse, C.M., Cheng, A.F., Bridges, N.T., Lewis, K., 2015, Controls on and implications of aeolian geomorphology on comet 67P: 4th International Planetary Dunes Workshop, Boise, ID, Abstract #8037.

Runyon, K.D., Barnouin, O.S., 2015, Gaspra's craters: Implications for production functions and surface processes: 46th LPSC, Abstract #2869.

Runyon, K.D., Bridges, N.T., 2015, Internal boundary layer control for sediment flux in Herschel Crater, Mars: 4th International Planetary Dunes Workshop, Boise, ID, Abstract #8021.

Bridges, N.T., Banks, M.E., Ayoub, F., Silvestro, S., Chojnacki, M.F., Geissler, P.E., Hansen, C.J., Mattson, S.S., **Runyon, K.D.**, Russell, P.S., 2014, Windy Mars: A Record of Bedform Migration and Sand Activity: 8th International Conference on Mars.

Runyon, K.D., Bridges, N.T., Ayoub, F., Mattson, S., 2014, Aeolian Provinces and Activity in Herschel Crater, Mars: 45th LPSC, Abstract #1495.

Runyon, K.D., Barnouin, O.S., 2014, Experimental Ejecta Emplacement: Early Results: 45th LPSC, Abstract #1071

Runyon, K.D., 2013, Terrestrial Meteorites as Preservers of Early Biomarkers: Implications for Selection of Golden Spike Landing Sites: Workshop on Golden Spike Human Lunar Expeditions, Lunar and Planetary Institute, Abstract #6020.

Runyon, K.D., Barnouin, O.S., 2013, Ejecta Emplacement and Regolith Gardening: An Experimental Investigation: 44th LPSC, Abstract #2163.

Barnouin, O.S., **Runyon, K.D.**, Susorney, H., Ernst, C.M., Wada, K., 2012, Experimental Investigation of Ejecta Emplacement, 2012 GSA Annual Meeting, Session No. 202, v. 44, no. 7, p. 482.

Runyon, K.D., Blair, D.M., Lemelin, M., Nowka, D., Roberts, C.E., Paige, D.A., Spudis, P., Kring, D.A., 2012, Volatiles at the Lunar south pole: A case study for a mission to Amundsen crater: 43rd LPSC, Abstract #1619.

Runyon, K.D., Davatzes, A.K., Gulick, V.C., 2012, Putative active brine flows in the Cerberus Fossae, Mars: 43rd LPSC, Abstract #2072.

Roberts, C.E., Blair, D.M., Lemelin, M., Nowka, D., **Runyon, K.D.**, Paige, D.A., Spudis, P.D., Kring, D.A., 2012, The potential for volatiles in the intercrater highlands of the Lunar north pole: 43rd LPSC, Abstract #1371.

Lemelin, M., Roberts, C.E., Blair, D.M., **Runyon, K.D.**, Nowka, D., Paige, D.A., Spudis, P.D., Kring, D.A., 2012, Finding volatiles on the Lunar surface: An innovative multi-source ArcGIS-based approach: 43rd LPSC, Abstract #1067.

Runyon, K.D., Davatzes, A.K., Davatzes, N.C., 2011, Structural characterization of the Cerberus Fossae at the Athabasca Valles source region, Mars: 42nd LPSC, Abstract# 1913.

Oral and Poster presentations: Multiple oral and poster presentations at planetary science conferences and workshops per year. 2011-present

Research Skills

GIS

ArcGIS (proficient), GoogleEarth (highly skilled), Small Body Mapping Tool (highly skilled), JMARS (proficient) ENVI (proficient), COSI-Corr (proficient), ISIS (familiar), SOCET SET (familiar).

Computational

Matlab (proficient) MS Excel (proficient), IDL (familiar).

Laboratory and Field

Laboratory experiment design, setup, implementation, and cleanup for sedimentary morphodynamics (highly skilled); Field geology and field mapping (proficient).

Graphics
Adobe Photoshop (highly skilled), Adobe Illustrator (proficient), QuickTime (highly skilled).

Memberships
- The Planetary Society, 2003-present.
- Geological Society of American student member, 2014-2015.
- Astronauts For Hire associate member, 2011-present.

Invited Talks
"Geology Across the Solar System," Guest Lecturer, Howard Community College Introductory Astronomy, March 8, 2017.

"Morphology and Dynamics of a Martian Sand Sheet," Geological Society of America fall conference, October, 2016.

"Planetary Sedimentology: Impact Crater Ejecta Emplacement and Martian Sand Dunes," George Mason University geology colloquium series, January, 2016.

"From Pluto, With Love," Spring Arbor University science outreach series, August, 2015.

"Physical Modeling of Impact Crater Ejecta Emplacement," Carnegie Department of Terrestrial Magnetism, Spring, 2013.

"Crustal Permeability of the Cerberus Fossae, Mars," Houghton College Interdisciplinary Science Seminar, Fall, 2010.

In the News
March 30, 2017—Now.Space—Geophysical Planet Definition and Pluto
http://now.space/posts/redefinition/

March 29, 2017 - Scientific American—Geophysical Planet Definition and Pluto
https://www.scientificamerican.com/article/ringo-is-a-beatle-hawaii-is-a-state-mdash-why-isnt-pluto-a-planet/

March 25, 2017 - Vox—Geophysical Planet Definition and Pluto
http://www.vox.com/science-and-health/2017/3/25/15052084/make-pluto-planet-again

March 21, 2017 - Reuters—Geophysical Planet Definition and Pluto
http://www.reuters.com/article/us-space-pluto-idUSKBN16S2GU

March 21, 2017 USA Today—Geophysical Planet Definition and Pluto
http://www.usatoday.com/story/tech/nation-now/2017/03/21/nasa-scientists-researchers-will-pluto-become-planet-new-definition/99440868/

March 20, 2017 - Washington Post—Geophysical Planet Definition and Pluto
https://www.washingtonpost.com/news/speaking-of-science/wp/2017/03/20/a-new-definition-would-add-102-planets-to-our-solar-system-including-pluto/?hpid=hp_hp-cards_hp-card-national%3Ahomepage%2Fcard&utm_term=.e469956542bd

March 17, 2017 - JHU & Phys.Org—Geophysical Planet Definition and Pluto
http://hub.jhu.edu/2017/03/16/make-pluto-a-planet-again/

March 2, 2017 - Wired.com – Geophysical Planet Definition and Pluto
https://www.wired.com/2017/03/pluto-thing/

February 28, 2017 - Seeker.com – Geophysical Planet Definition and Pluto
http://www.seeker.com/behind-the-push-to-get-pluto-its-planetary-groove-back-2290287200.html

February 21, 2017 - Universe Today – Geophysical Planet Definition and Pluto
http://www.universetoday.com/133525/sad-pluto-110-planets-solar-system-instead/

February 21, 2017 - CBC Radio, As It Happens – Geophysical Planet Definition and Pluto
http://www.cbc.ca/radio/asithappens/as-it-happens-tuesday-edition-1.3991263/make-pluto-a-planet-again-nasa-scientists-argue-1.3991265

February 21, 2017 - Inverse.com – Geophysical Planet Definition and Pluto
https://www.inverse.com/article/28125-pluto-ninth-planet-new-definition

May 13, 2016 - The Escapist – Geology Consultant for Video Game
http://www.escapistmagazine.com/articles/view/video-games/editorials/reviews/17037-Offworld-Trading-Company-Strategy-Economy-Simulation#&gid=gallery_6232&pid=5

May, 2016 - Mental_Floss – Geology Consultant for Video Game
http://mentalfloss.com/article/79318/game-set-mars-next-oregon-trail

Winter, 2016 - Houghton College Magazine – Pluto Exploration
http://www.houghtonmagazine.com/open-your-eyes-look-up-to-the-skies-and-see/

Christmas, 2015 - Home.fm morning show interivew – Pluto Exploration

http://home.fm/wp-content/uploads/2015/08/Kirby-in-Space-EXTENDED.mp3

June 29, 2015 – Pluto Exploration
http://www.mlive.com/news/jackson/index.ssf/2015/06/kirby_runyon.html

April 5, 2012 - 365 Days of Astronomy Podcast Inteview – Human Lunar Mission
https://cosmoquest.org/x/365daysofastronomy/2012/04/05/april-5th-a-human-mission-to-the-lunar-south-pole/